

**Measurement of the spatial location of double
escape events in a germanium detector using a
PET scanner**

Dissertation

der Mathematisch-Naturwissenschaftlichen Fakultät
der Eberhard Karls Universität Tübingen
zur Erlangung des Grades eines
Doktors der Naturwissenschaften
(Dr. rer. nat.)

vorgelegt von
Christopher Alexander Schmitt
aus Dinslaken

Tübingen 2018

Measurement of the spatial location of double escape events in a germanium detector using a PET scanner

Dissertation

der Mathematisch-Naturwissenschaftlichen Fakultät
der Eberhard Karls Universität Tübingen
zur Erlangung des Grades eines
Doktors der Naturwissenschaften
(Dr. rer. nat.)



vorgelegt von
Christopher Alexander Schmitt
aus Dinslaken

Tübingen 2018

Gedruckt mit Genehmigung der Mathematisch-Naturwissenschaftlichen Fakultät der Eberhard Karls Universität Tübingen.

Tag der mündlichen Qualifikation:

15.06.2018

Dekan:

Prof. Dr. Wolfgang Rosenstiel

1. Berichterstatter:

Prof. Dr. Josef Jochum

2. Berichterstatter:

Prof. Dr. Peter Grabmayr

ABSTRACT

Germanium detectors have been used in science to carry out high resolution spectroscopy for more than half a century. Only recently has their capacity to distinguish different types of events been put to use in low-background experiments. By examining the waveform, it is possible to distinguish signal-like from background-like events and push down the background index of such experiments even further than previously achieved. For an analysis of the pulse shape it is beneficial to fully understand the pulse shape creation process.

In this work, a new method is proposed to measure the point of interaction of signal-like double escape events inside a germanium detector by using a PET detector. A typical waveform is assigned to each point in the detector. By knowing the different shapes of the pulses, the pulse shape discrimination can be tested and possibly be improved. The general method, preceding simulations, the measurement setup, and the results are presented in this thesis.

One chapter addresses an otherwise rather unrelated deconvolution method to analyse waveforms of photomultipliers and, simultaneously, calibrate them in units of photo electrons.

ZUSAMMENFASSUNG

Germaniumdetektoren werden bereits seit geraumer Zeit in der Wissenschaft für spektroskopische Messungen eingesetzt. Erst seit kurzem wird von ihrer Eigenschaft unterschiedliche Eventtypen unterscheiden zu können bei Experimenten mit niedrigem Untergrund Gebrauch gemacht. Durch Analysieren der Pulsform ist es möglich signalähnliche von untergrundähnlichen Ereignissen zu unterscheiden und den *background index* dieser Experimente dadurch noch weiter abzusenken. Solch eine Analyse setzt Wissen über den exakten Entstehungsprozess des Pulses voraus.

In dieser Arbeit wird eine Methode vorgestellt, um den Interaktionspunkt eines Signalereignisses im Germaniumdetektor mithilfe eines PET-Scanners zu bestimmen. So kann eine typische Pulsform jedem Punkt im Detektor zugeordnet werden. Die Kenntnis über die Form der Pulse abhängig vom Ort kann zum Test und möglichen Verbesserung der Pulsformdiskriminierung verwendet werden. In der Arbeit werden die Grundidee der Methode, vorangegangene Simulationen, der Messaufbau und die Ergebnisse beschrieben.

Ein sonst thematisch eher unverbundenes Kapitel beschäftigt sich mit einer Kalibrations- und Analyseverfahren, die auf der Dekonvolution von Standardpulsen basiert und eine gleichzeitige Kalibration in Einheiten von Photoelektronen ermöglicht.

Contents

1 INTRODUCTION	1
2 THE NEUTRINOLESS DOUBLE BETA DECAY ($0\nu\beta\beta$)	3
2.1 Neutrino physics	3
2.1.1 Neutrino oscillation	5
3 PARTICLE DETECTION WITH SEMICONDUCTOR DETECTORS	17
3.1 Interactions with matter	17
3.2 Germanium detectors	21
3.2.1 Semiconductor physics	21
3.2.2 pn junctions	22
3.3 Signal formation	24
3.4 Pulse shape discrimination	26
4 THE GERDA EXPERIMENT	31
4.1 Setup	31
4.2 Sensitivity and background	35
4.3 First results	37
5 DECONVOLUTION OF PMT SIGNALS	41
5.1 Deconvolution	43
5.2 Comparison to older methods	45
6 SIMULATION AND FEASIBILITY OF THE PET EXPERIMENT	49
6.1 General idea	49
6.2 <i>Geant4</i> simulations	51
6.2.1 Dimensions of collimator	52
6.2.2 Expected rates	56
6.2.3 Position reconstruction	58
6.3 Summary	64
7 SETUP OF THE PET EXPERIMENT	65
7.1 Measurement setup	65
7.2 Triggers and timing pattern	68

7.3	The Inveon PET scanner	70
7.4	Radioactive source	72
8	RESULTS OF THE PET EXPERIMENT	75
8.1	Analysis and results	76
8.2	Energy spectrum	78
8.3	Time shift correction	80
8.3.1	The time difference method	82
8.3.2	The fitting method	83
8.4	Coincidences	88
8.4.1	Coincidences from PET and germanium data	89
8.4.2	Coincidences within PET data	92
8.4.3	Delayed trigger	93
8.5	Root cause analysis	94
8.5.1	Structure in the temporal pattern	94
9	SUMMARY	101
	A MEASUREMENT REPORT ^{56}Co SOURCE	103

1

Introduction

*“Begin at the beginning, the King said gravely, and
go on till you come to the end: then stop.”*

— Lewis Carroll, *Alice in Wonderland*

The goal of the experiment described in this thesis is to measure pulse shapes of germanium detectors and their corresponding location within the germanium crystal by using a PET scanner and a beam of collimated gamma rays. The high-energy gammas can produce an electron-positron pair via pair production; the positron, after being stopped, emits two 511 keV gammas that are directed in opposite directions when annihilating with an electron from the crystal. The gammas are then detected in a medical PET¹ detector that can, under the assumption of a collimated initial gamma beam, reconstruct the position where the interaction took place. The experiment is carried out by using the 2598.5 keV and 3253.5 keV γ -lines of ⁵⁶Co. The procedure how these two detector systems are synchronized in order to detect coincident events across both systems is a major part of this thesis. The feasibility of the experiment the dimensions and setup that have to be used are simulated beforehand. With this method of intersecting lines of collimator and PET detectors, the location of the point of interaction of such a single site event (SSE) inside the germanium detector can be measured. The shape of the pulse induced in the electrode on the outside of the detector is recorded for every reconstructed location. The benefit of this method is that it allows to better understand pulse formation in the crystal. Pulses created by single site events look in principle very similar. Yet there are small differences depending on the location of the interaction within the crystal. In astroparticle physics experiments such as GERDA ([5]), the

¹positron emission tomography

pulse shape is used to differentiate between wanted signal-like and unwanted background-like multi-site events (MSE). The signature reaction of the $0\nu\beta\beta$ is single-site-event-like while multi-site-events are mainly caused by gamma particles that compton-scatter several times within the detector, depositing their energy in multiple locations. In order to improve the cut efficiencies and to accurately measure these efficiencies, it is necessary to understand the differences in pulse shape due to different points of origin. The background index of experiments like GERDA is crucial in order to further improve the sensitivity; understanding pulse formation and pulse shape discrimination better and be able to get a position sensitive measurement can help in controlling and improving the background index.

Pulse shape behaviour of a detector can be simulated with programs that track the paths of the particles and compute the electric fields induced on the electrodes. With the method described in this work, direct comparisons between computer simulated pulse shapes and an actual real world experiment are possible. While simulations know quite a lot about the location, drifting speeds, etc. of the simulated particles, they lack the possibility to compare these parameters of the simulation to the experimentally accessible world. This is why their results can usually only be compared to processed spectra as they are observed in the experiment. This is due to the fact, that the point of interaction where the pair production takes place is not known and cannot be controlled. Therefore quite some information about the individual pulses is lost. With the method proposed in this thesis it should be possible to directly compare pulse shapes originating in the same location measured by experiment with those calculated with simulations. The effects that changes of the simulation parameters have can be much easier compared to a measured pulse than to a histogram containing aggregated and reduced data.

This thesis covers an introduction to the neutrino and astroparticle physics, with a special emphasis on the neutrinoless double beta decay ($0\nu\beta\beta$) in chapter 2. Chapter 3 covers semiconductor detectors, especially those made from germanium. The pulse formation mechanism is also described in this chapter. The experiment GERDA, in which context the idea for this project was created and where its main motivation is drawn from, is introduced and described in chapter 4. Chapter 5 is not directly related to the main topic of this thesis, but describes a technique used for the analysis of the muon veto of the GERDA experiment which also helps in reducing the background index. This method is based on a deconvolution of the photomultiplier signals and includes an automatic calibration in units of photo electrons. The PET project itself, its basic principle, the simulations done to estimate the efficiencies, the dimensions needed for the collimator and to prove the general feasibility are explained in chapter 6. The experimental setup is described in chapter 7. Finally, the results of the measurements are explained in this key chapter of the thesis, chapter 8. The problems encountered and what was done to try to evade them is layed out here as well. At the end of the thesis, chapter 9 provides a summary of the thesis and gives an outlook how these obstacles could be overcome in a future experiment.

2

The neutrinoless double beta decay ($0\nu\beta\beta$)

“Nukular! Das Wort heißt nukular!”

Homer J. Simpson

Wolfgang Pauli introduced the idea of the neutrino¹ in his illustrious letter to the “radioactive Damen und Herren” [48] meeting in Tübingen in 1930. Its discovery by the POLTERGEIST experiment (also known as the Cowan-Reines experiment) in 1956 [23], took place almost 30 years after their postulation. Even today, neutrinos still remain at the forefront of scientific mystery with only a handful of their properties discovered. While by now it is known that neutrinos come in three flavors (electron-, muon- and tau-like) and that the neutrino can oscillate between these states, their absolute masses are still unknown. Their inherent nature, i.e. if they behave as Majorana or Dirac particles is still unknown as well. The neutrinos and their properties, according to the standard model and going beyond that, are introduced in the following paragraphs; properties expected by theory and sought after in current experiments are explained as well.

2.1 NEUTRINO PHYSICS

The notion of a neutrino was imposed to explain the apparent non-conservation of energy, observed in β -decays. Instead of a fixed energy value, a continuous spectrum of the electron energies was observed in beta decays. Pauli stated that the reaction equation describing the $\beta^{(-)}$ -decay should be extended by an extra neutral, (almost) massless, weakly interacting

¹He initially called it a neutron. After the neutron was discovered by Chadwick in 1932, the Italian diminutive suffix “-ino” was added.

particle: the neutrino²:

$$n \rightarrow p + e^{-} + (\bar{\nu}_e) \quad (2.1)$$

The idea behind it was that the electron and the neutrino would share the total energy of the decay, but the neutrino, due to its extremely low cross-section, would carry away its energy undetected. The energy of the electron would be measured in the detector. This would explain the continuous spectrum of the β -decay.

It took until 1956 to directly detect this newly postulated but evasive particle. Cowans and Reines managed to detect (anti-)neutrinos at the Savannah River Site by using the inverse beta decay reaction

$$\bar{\nu}_e + p \rightarrow n + e^{+}. \quad (2.2)$$

The anti-neutrinos of a nuclear reactor were used as a strong neutrino source to trigger the reaction described above. The annihilation reaction of the positron emits two γ -rays. The produced neutron thermalizes and is captured either on hydrogen or cadmium and another signature gamma cascade is emitted. The occurrence of these two events within a certain time window was used as a signature to distinguish an anti-neutrino.

Three families of neutrinos have been discovered since; corresponding to the three lepton families of the electron, muon and τ -lepton the neutrinos exist in the three flavours ν_e , ν_μ and ν_τ . The ν_μ was discovered in 1962 by Leon Lederman, Melvin Schwartz and Jack Steinberger at the Brookhaven National Laboratory. In 1988, they were awarded the Nobel prize for their discovery. After the τ -lepton had been discovered at the Stanford Linear Accelerator Center (SLAC) in 1975, the existence of a ν_τ was already strongly expected. It took until 2000 to directly detect the ν_τ and confirm its existence in the DONUT experiment at Fermilab [26].

THE STANDARD MODEL

The Standard Model of particle physics describes the electro-magnetic, weak and strong nuclear forces and categorizes all elementary particles according to their interactions and properties. It has been developed in the second half of the 20th century. The last big piece of the puzzle was the discovery of the Higgs boson in 2013. The particles are classified according to the statistics they obey. Bosons (Bose-Einstein statistics) are the mediators of the forces and carry integer spin. Fermions (Fermi-Dirac statistics) have odd half-integer spin ($\frac{1}{2}$, $\frac{3}{2}$, $\frac{5}{2}$, ...) and follow the Pauli Exclusion Principle.

A particle exchange of bosons corresponds to the action of a force. Fermions can be subdivided into leptons and baryons by their behaviour to interact or not to interact via the strong force. The leptons appear in three flavors: e, μ, τ . Every massive lepton has an almost massless neutrino partner of the same flavor assigned. Here, the limitations of the Standard Model are already apparent. While the Standard Model is able to explain a great deal of

²Technically, in this equation it has to be an anti-neutrino.

electro-magnetic force	photon
weak nuclear force	W, Z^+, Z^- bosons
strong nuclear force	gluons

Table 2.1: The three forces of the Standard Model and their exchange particles.

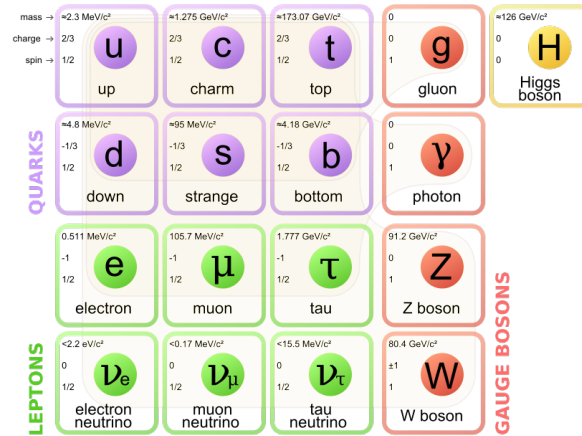


Figure 2.1: The Standard Model of particle physics describes and classifies subatomic particles and their interaction forces. [57]

particle physics, according to it, neutrinos should be massless. This is not true, since neutrino oscillations have been observed. Why this leads to non-zero masses of the neutrinos will be explained in more detail in the next section (sec. 2.1.1).

Neutrinos interact only via the weak and gravitational force. Therefore, the cross-section is very small and it is very hard to detect them.

2.1.1 NEUTRINO OSCILLATION

By now it is well established that neutrinos have non-zero mass, albeit a very small one. This mass is in contradiction to the Standard Model. Neutrinos are observed in three flavor eigenstates that are a combination of three mass eigenstates. The exact amount of these combinations, the so called mixing angles, have been studied by a variety of experiments with different techniques and neutrino sources.

Having been predicted theoretically by Bruno Pontecorvo in 1957 [50], neutrino oscillation was used to explain the observed disappearance of solar neutrinos in the Homestake experiment by Raymond Davis Jr. in the 1960s [24]. Davis was measuring the neutrino flux of solar neutrinos by chemically extracting Argon atoms from a large tank of a chlorine compound. ^{37}Ar is created by the neutrino induced beta decay reaction:

$$\nu_e + {}^{37}\text{Cl} \rightarrow {}^{37}\text{Ar} + e^- \quad (2.3)$$

The observed flux was a factor of three lower than the expected flux from solar model calculations. It took several more years and the results of the experiments Kamiokande [36], SAGE [1], and GALLEX [33] to establish the solar neutrino deficit and thereby neutrino oscillations. The more recent experiments SNO [34], BOREXINO [19] and Super-Kamiokande [29] have significantly contributed to establishing neutrino oscillations as the solution to the deficit by detecting not only solar neutrinos but also myon-neutrinos created in the atmosphere. Recently, there have been neutrino experiments using particle beams([7],[2]) and nuclear reactors ([4],[16],[13]) as (anti-)neutrino sources. The two experiments Double Chooz [4] and Daya Bay [16] first established the last unknown neutrino mixing angle θ_{13} to be non-zero.

Neutrinos are produced via weak interaction in its flavour eigenstate $|\nu_\alpha\rangle$, where $\alpha = e, \mu, \tau$. But it propagates in the mass eigenstates $|\nu_i\rangle$, with $i = 1, 2, 3$. Right now we know about three neutrino families, and that a propagating neutrino can oscillate into the three flavour eigenstates along its way. The relation between flavour and mass eigenstates is given via

$$|\nu_i\rangle = \sum_{\alpha} U_{\alpha i} |\nu_\alpha\rangle \quad \text{and} \quad |\nu_\alpha\rangle = \sum_i U_{\alpha i}^* |\nu_i\rangle \quad (2.4)$$

respectively. The matrix $U_{\alpha i}$ is named after Bruno Pontecorvo, Ziro Maki, Masami Nakagawa and Shoichi Sakata, and more commonly referred to as the PMNS-matrix. It can be represented factorised into four matrices:

$$\begin{aligned} U &= \begin{pmatrix} U_{e1} & U_{e2} & U_{e3} \\ U_{\mu1} & U_{\mu2} & U_{\mu3} \\ U_{\tau1} & U_{\tau2} & U_{\tau3} \end{pmatrix} \\ &= \begin{pmatrix} 1 & 0 & 0 \\ 0 & \cos(\theta_{23}) & \sin(\theta_{23}) \\ 0 & -\sin(\theta_{23}) & \cos(\theta_{23}) \end{pmatrix} \begin{pmatrix} \cos(\theta_{13}) & 0 & \sin(\theta_{13})e^{-i\delta} \\ 0 & 1 & 0 \\ -\sin(\theta_{13})e^{-i\delta} & 0 & \cos(\theta_{13}) \end{pmatrix} \\ &\cdot \begin{pmatrix} \cos(\theta_{12}) & \sin(\theta_{12}) & 0 \\ -\sin(\theta_{12}) & \cos(\theta_{12}) & 0 \\ 0 & 0 & 1 \end{pmatrix} \begin{pmatrix} 1 & 0 & 0 \\ 0 & e^{i\alpha} & 0 \\ 0 & 0 & e^{i\beta} \end{pmatrix} \end{aligned}$$

where the θ_{ij} are the mixing angles between the mass eigenstates, δ is the CP-violating phase and α and β denote the Majorana phases that only exist if the neutrino were a Majorana particle. Otherwise, in case of the neutrino being a Dirac particle, the phases would vanish and this last matrix would amount to the unity matrix.

The state describing the neutrino after time t and distance of propagation L is given by

$$|\nu_i(t)\rangle = e^{-iE_i t + ip_i L} |\nu_i\rangle, \quad (2.5)$$

with E_i being the energy of the mass state and p_i its momentum. Using equation 2.4 and

assuming a pure flavour eigenstate³ at $t = 0$ the state develops with t :

$$|\nu_\alpha(t)\rangle = \sum_{i=1,2,3} U_{\alpha i} e^{-iE_i t + ip_i L} |\nu_i\rangle = \sum_{\beta=e,\mu,\tau} \sum_{i=1,2,3} U_{\alpha i} e^{-iE_i t + ip_i L} U_{\beta i}^* |\nu_\beta\rangle \quad (2.6)$$

The transition amplitude for a state $|\nu_\alpha\rangle$ to oscillate into $|\nu_\beta\rangle$ is given by:

$$\langle \nu_\beta | \nu_\alpha(t) \rangle = \sum_{i=1,2,3} U_{\alpha i} U_{\beta i}^* e^{-iE_i t + ip_i L} \quad (2.7)$$

from which the transition probability $P_{\alpha \rightarrow \beta}$ follows directly:

$$\begin{aligned} P_{\alpha \rightarrow \beta} &= |\langle \nu_\beta | \nu_\alpha(t) \rangle|^2 = \left| \sum_i U_{\alpha i} U_{\beta i}^* e^{-iE_i t} \right|^2 = \sum_{i,j} U_{\alpha i} U_{\alpha j}^* U_{\beta i}^* U_{\beta j} e^{-(E_i - E_j)t} \\ &= \sum_i |U_{\alpha i}|^2 |U_{\beta i}|^2 + 2\text{Re} \sum_{j>i} U_{\alpha i} U_{\alpha j}^* U_{\beta i}^* U_{\beta j} \exp \left\{ -i \frac{\Delta m_{ij}^2 L}{2E} \right\} \end{aligned} \quad (2.8)$$

with $\Delta m_{ij}^2 = m_i^2 - m_j^2$. The propagation velocity of neutrinos is practically c and, therefore, the time and the propagation distance can be considered equal in natural units (with $c = 1$). This leads to the relation:

$$E_i t - p_i L \simeq (E_i - p_i) L = \frac{E_i^2 - p_i^2}{E_i + p_i} L = \frac{m_i^2}{E_i + p_i} \simeq \frac{m_i^2}{2E} L, \quad (2.9)$$

that is used in equation 2.8. This means that the oscillation probability does not depend on the propagation time, but only on the propagation length from the source to the detector and the energy of the neutrino. This derivation follows roughly the path shown by Giunti and Laveder in their paper on neutrino mixing [30]. It should be noted that equation 2.8 describes the oscillation probabilities in vacuum. For the propagation in matter the MSW-effect⁴ has to be considered as well. It can heavily influence the probabilities, but the general form of the oscillations still depends on the same parameters.

Oscillation probabilities are hence often stated in dependency of $\frac{L}{E}$. This is the main parameter when designing an oscillation experiment. Figure 2.2 shows the probability for an initial electron neutrino to be found in one of the three flavour states depending on the distance travelled and the neutrino energy. In cases where $\frac{L}{E}$ values are not fixed exactly in the experiment, because propagation length or energy of the neutrinos can vary, some smaller oscillations are washed out and cannot be distinguished by the experiment. This can be, for example, the sun, with a non-negligible extension or the energy spectrum of a nuclear reactor being used as experimental sources. Neutrino oscillations are dependent on all three mixing angles, but in general there is only one specific mixing angle an experiment with its fixed source-detector distance, energy spectrum of the source, and detection principle is sensitive

³This assumption is very reasonable, since particles are always created in their flavour eigenstates.

⁴Mikheyev-Smirnov-Wolfenstein

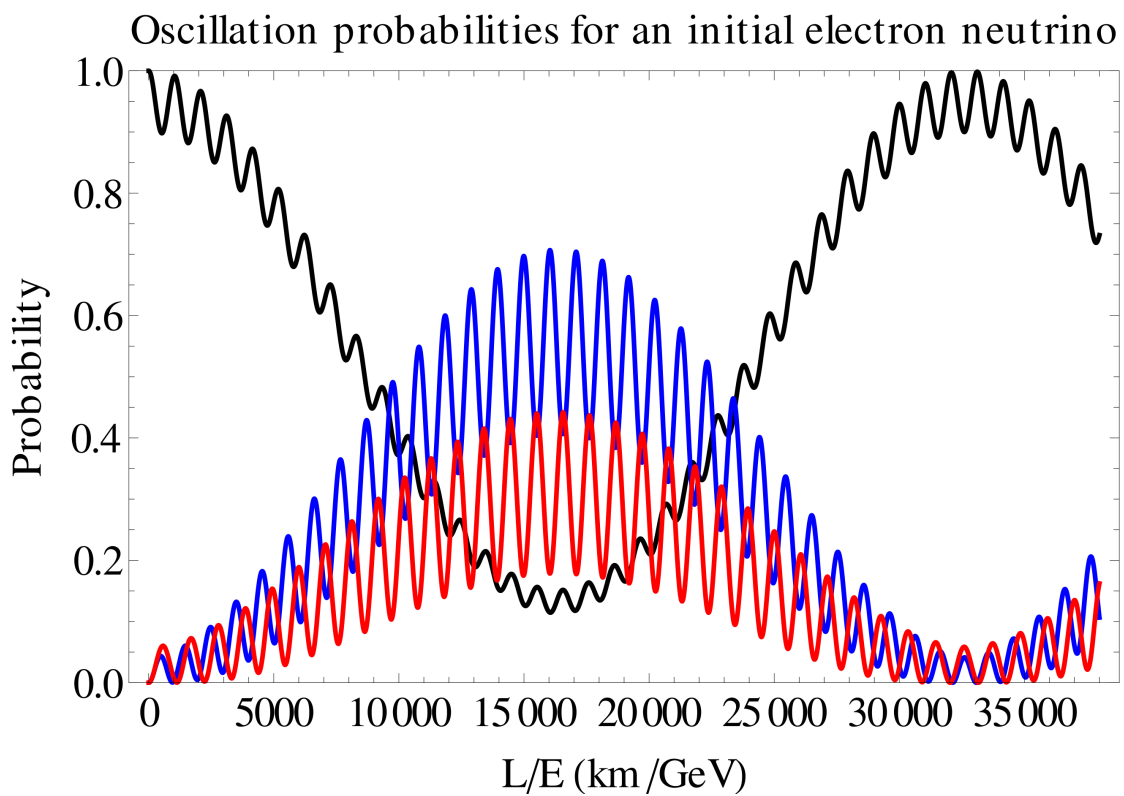


Figure 2.2: Probability for an initial electron neutrino to be detected as a different flavour. Colours are black for electron, blue for muon and red for tau neutrinos. The graph shows the probabilities for relatively long propagation distances and small energies. Taken from [56]

mixing angle	$\sin^2(\theta_{ij})$	θ_{ij}
θ_{12}	0.308 ± 0.017	34°
θ_{23}	$0.437^{+0.033}_{-0.023}$ (NH)	42°
	$0.455^{+0.039}_{-0.031}$ (IH)	
θ_{13}	$0.0234^{+0.0020}_{-0.0019}$ (NH)	8.8°
	$0.0240^{+0.0019}_{-0.0022}$ (IH)	

Table 2.2: Neutrino mixing angles and the corresponding $\sin^2(\theta_{ij})$. From [47].

for one. First hints to a possible neutrino oscillation were found in 1968 in the Homestake mine experiment lead by Raymond Davis Jr. The experiment observed only one third of the expected neutrino flux [24]. So either the solar model of the nuclear fusion processes that create neutrinos at various energies had to be flawed, or the neutrino must behave differently from what was expected (this is assuming that the researchers were confident in excluding any experimental errors). This solar neutrino deficit could be explained by the original (electron) neutrino from the sun oscillating into different flavour neutrinos that could not be detected by the setup used in this experiment.

Later on, many experiments using atmospheric, accelerator or reactor neutrinos as sources have been performed. The survival/appearance/disappearance probabilities of the different neutrino flavour states have been measured and from these probabilities the mixing angles θ_{ij} have been deduced. Table 2.2 shows the results of the combined experimental effort of studying the mixing angles for the last few decades. Values with their 1σ -uncertainties obtained from global analyses are listed. If the assumption of a normal or inverted mass hierarchy has an effect on the mixing angle, the different values are labelled with NH/IH for the normal/inverted hierarchy respectively. The mass hierarchy will be explained in more detail in the next section.

MASS HIERARCHY

The neutrino oscillation mixing angles are closely linked to the mass differences of the neutrino states, or rather their square Δm_{ij}^2 . It can be clearly seen in equation 2.8 that the Δm_{ij}^2 have a direct influence on the oscillation frequency of the neutrinos.

Δm_{12}^2 was the first mass-square to be measured. This was achieved by experiments studying solar neutrinos as described in section 2.1.1. Δm_{23}^2 was obtained from atmospheric neutrinos produced by cosmic rays hitting the upper atmosphere. So the significance of the mass square difference is clear and is accompanied by a few consequences:

- Neutrinos have a non-zero mass
- the absolute mass values cannot be deduced by oscillation experiments
- even the order of all neutrino masses cannot be determined with today's experiment, only the absolute mass differences can be derived from them

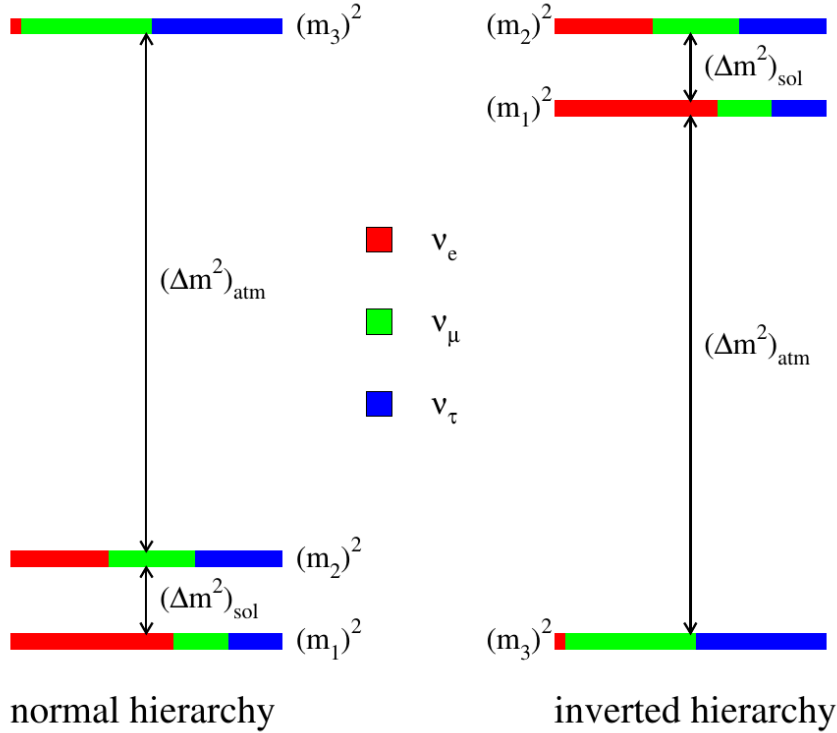


Figure 2.3: Mass hierarchy for the normal and inverted hierarchy. The mixture of flavour states is represented in the different colours. [25]

This last point is the so called mass hierarchy. Two possible solutions exist: The normal hierarchy in which the masses are ordered according to their mass state numbering $m(\nu_1) < m(\nu_2) < m(\nu_3)$; or the inverted hierarchy in which $m(\nu_3) < m(\nu_1) < m(\nu_2)$ holds. Knowing the mass hierarchy is important to check on a number of theories. There are theories that explain the unification of the four forces and predict a normal hierarchy. There are others that explain the origins of particles and the universe and predict an inverted hierarchy [14]. Obviously, only one interpretation can be right. One example of an experiment that wants to check this hypothesis, among others, is the Hyper-Kamiokande experiment in Japan [3]⁵. Muon neutrinos travel through the earth and reach the big water tanks of the experiment coming upwards. The probability to have changed to an electron neutrino would be larger in case of a normal mass hierarchy. This is shown in Figure 2.4 in dependence of the zenith angle. The inverted mass hierarchy would be realised; the probability for anti-muon neutrinos to turn into anti-electron neutrinos would be larger. Even though the mixing angles of the neutrino oscillations have been measured, the accuracy was not good enough yet to be able to distinguish such an effect.

Neutrinoless double beta decay experiments generally do not have the ability to differentiate between the two mass hierarchies. The inverted hierarchy can only be excluded if the $0\nu\beta\beta$ exists with $\langle m_{\beta\beta} \rangle \leq 0.01$ eV and the standard interpretation of light Majorana neutrino ex-

⁵Other experiments also probing the mass hierarchy are ORCA as part of the KM3NET, PINGU with ICECUBE, and JUNO.

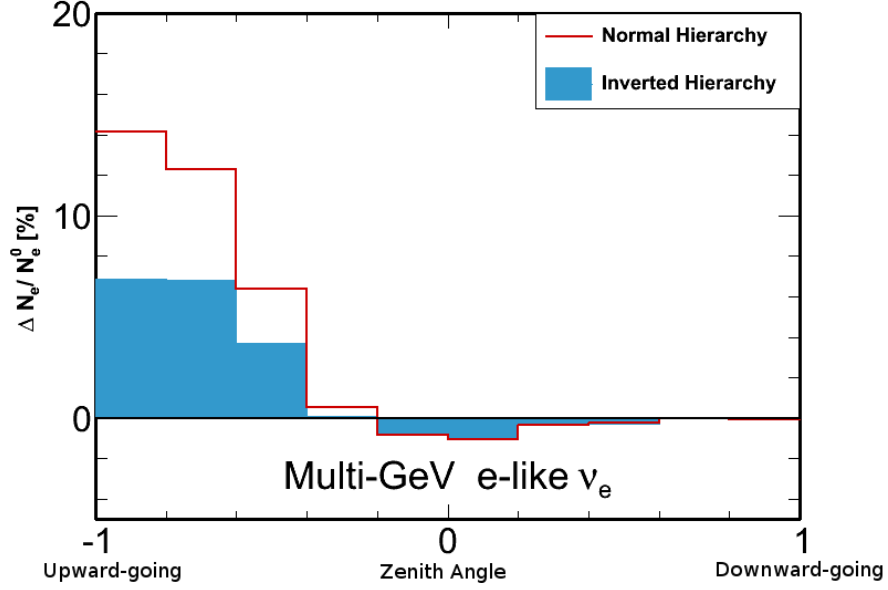


Figure 2.4: Difference in production rates of electron neutrinos induced by muon neutrinos for normal and inverted hierarchy. [3]

change is assumed (Fig. 2.5). The half-life of the $0\nu\beta\beta$ is the only quantity accessible from experiment, but it is possible via the nuclear matrix element \mathcal{M} to calculate the effective neutrino mass $\langle m_{\beta\beta} \rangle$:

$$\frac{1}{T_{1/2}} = \Phi \mathcal{M}^2 \left| \frac{\langle m_{\beta\beta} \rangle}{m_e} \right|^2 \quad (2.10)$$

The phase space Φ relates the quantities half-life $T_{1/2}$ and effective neutrino mass. m_e is the electron mass and the effective Majorana neutrino mass is defined as

$$\langle m_{\beta\beta} \rangle = \left| \sum_i U_{\alpha i}^2 m_i \right| = \left| \cos^2 \theta_{12} \cos^2 \theta_{13} m_1 + \sin^2 \theta_{12} \cos^2 \theta_{13} m_2 e^{i2\alpha} + \sin^2 \theta_{13} m_3 e^{i2\beta} \right| \quad (2.11)$$

The nuclear matrix element \mathcal{M} has to be calculated in elaborate calculations and today the results differ by a factor of ~ 3 . The phase space Φ indicates the space of all possible states and can be calculated accurately.

But this means, that along with a long enough half-life of the neutrinoless double beta decay, the effective neutrino mass could be low enough to be able to distinguish the two hierarchies, as it is shown in Figure 2.5. In principle, with increasing exposure of the $0\nu\beta\beta$ experiments, and without a positive find, $\langle m_{\beta\beta} \rangle$ would be limited to smaller and smaller values, cutting into the parameter space of the inverted hierarchy. In reality, the experiments will not be able to probe deeply into this range of the parameter space in the near future. Experiments on a much larger scale would be needed.

Even though the neutrino oscillations and the neutrino mass differences are known now, the

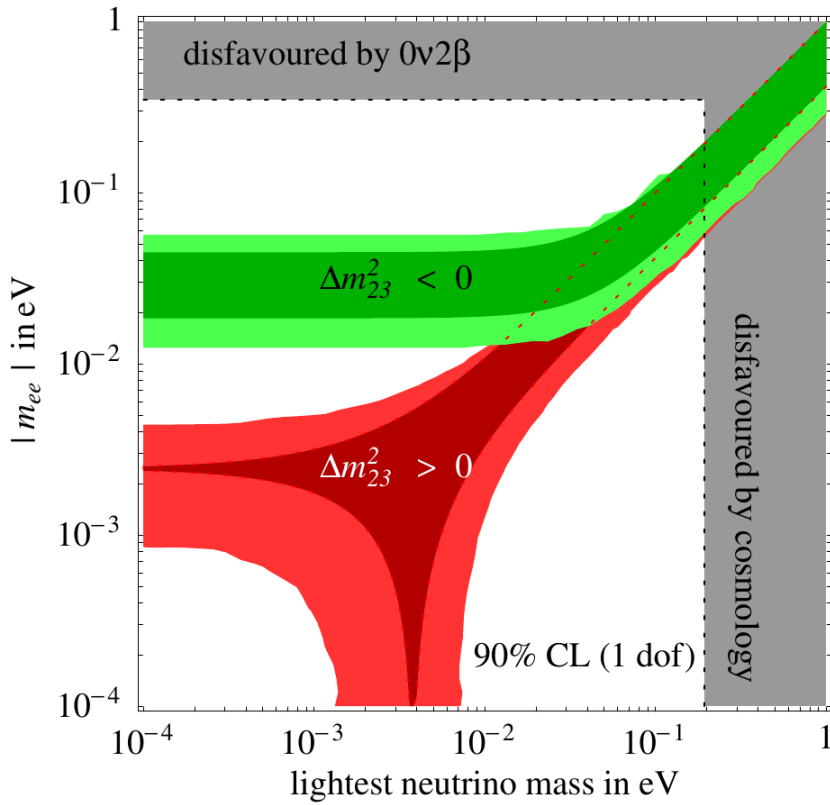


Figure 2.5: Effective neutrino mass as a function of the lightest neutrino mass. The different colours of the bands belong to the inverted hierarchy (green) and the normal hierarchy (red). [27]

absolute value of the neutrino(s)⁶ is still unknown and also cannot be measured by either oscillation or double beta experiments. There are two general approaches that so far have only been able to limited the possible range of the absolute neutrino mass. One are the experiments that very accurately measure the endpoint of the beta decay spectrum and determine the missing energy. This missing energy is attributed to the electron neutrino mass that silently escapes along with the neutrino. An experiment employing this approach is KATRIN⁷ and is still in the setup process. It aims to measure m_{ν_e} down to 0.35 eV by using a gigantic mass spectrometer to measure the beta-decay of tritium [38].

Another approach are cosmological measurements as they were for example carried out by ESA's Planck satellite [49] that measured the anisotropies of the microwave background. The Planck collaboration arrived at a limit for the sum of the neutrino masses of

$$\sum_i m_i < 0.23 \text{ eV}. \quad (2.12)$$

The next section will take a closer look at the double beta decay itself and give a quick overview of isotope where the neutrinoless double beta decay might occur.

⁶If one neutrino mass were known, the others could be derived via the known mass differences. Provided the mass hierarchy is known by then.

⁷Karlsruhe Tritium Neutrino Experiment

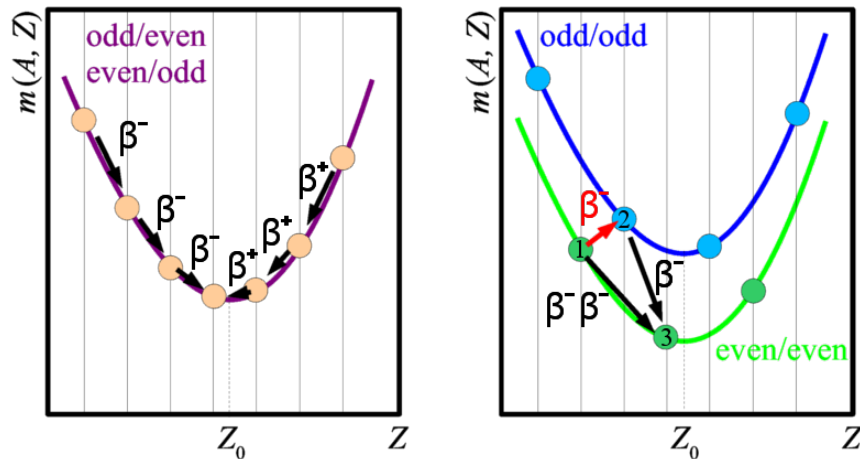


Figure 2.6: The parabola of isobares shows two examples where a β decay is energetically allowed (left) and forbidden (right). Even though a single β -decay may be forbidden on the right side, a double beta decay, with or without neutrinos, can potentially occur.

DOUBLE BETA DECAY

Double beta decay is a possibility for some nuclei to decay to a lower state that cannot decay energetically via a single β -decay. Instead of the regular β^- -decay with:



the double beta-decay, as the name promises, doubles all constituents of the above equation:



The energetical situation of both types of beta decay is shown in Figure 2.6. While a decay as in equation 2.13 might be forbidden, for 35 even-even isotopes the double beta-decay, as described in equation 2.14, is possible. The probability for the decay to occur is very small though. It is a second order process with its intermediate state violating energy conservation [35] and its half-life is typically in the order of $\sim 10^{20}$ yr. There are assumed to be two types of double beta decay; the one with neutrinos and the neutrinoless, this is why the neutrinos in equation 2.14 were put in parenthesis. The “regular” two-neutrino double beta decay ($2\nu\beta\beta$) has already been observed in ${}^{130}\text{Te}$ in 1950. The neutrinoless double beta decay ($0\nu\beta\beta$), which is a consequence of the neutrino being its own antiparticle as hypothesised by Ettore Majorana in 1937 [43], has been proposed by Maria Goeppert-Mayer as early as 1935 [31], but to this day its existence has not been experimentally confirmed.

In order for the $0\nu\beta\beta$ to happen, the neutrino needs to be its own antiparticle. On the other hand, if the neutrino followed the classical particle-antiparticle schema proposed by Dirac, the $0\nu\beta\beta$ does not exist.



Figure 2.7: Feynman graphs of the two types of neutrinoless double beta decay. [32]

Majorana	Dirac
$\nu_e = \bar{\nu}_e$	$\nu_e \neq \bar{\nu}_e$

Table 2.3: Property of the neutrino/anti-neutrino if they behave like a Majorana/Dirac particle

$0\nu\beta\beta$ EXPERIMENTS

The experimental search for the neutrinoless double beta decay has seen a rise in recent decades, many different collaborations around the world are now trying to find that rare decay. Different techniques have been used to study a multitude of candidate isotopes. Each isotope having its own $Q_{\beta\beta}$ energy endpoint of the beta spectrum and with this are more or less susceptible to ambient gamma background. The detection techniques may involve direct or indirect measuring methods; the direct approach incorporates the isotope in the detector material, while with the indirect approach source material and detector are separated. Also, depending on the type of detector, the energy resolution of the experiments varies widely. The best resolution being found with semiconductor detectors, in particular germanium, the worst resolutions are usually found with photomultiplier experiments.

The different double beta isotopes, their $Q_{\beta\beta}$ energies, half-life and the experiment investigating them are compiled in Table 2.4. The choice of isotope is crucial and determines the experiment's specifications as different properties like $Q_{\beta\beta}$ and half-life influence the requirements on background, active mass needed or detection method. In the end, economic considerations also play a significant role. It has to be determined how expensive it is to produce and buy a certain amount of the isotope, and if necessary what the process and cost of an enrichment in the sought-for isotope is.

This work was created in the environment of the GERDA collaboration that searches for the $0\nu\beta\beta$ decay of ^{76}Ge with a “*detector = source*” approach at Gran Sasso. This experiment will be covered in more depth in chapter 4. The germanium semiconductor detectors used in GERDA and investigated in this thesis are described in the next chapter. This chapter explains their interaction with matter, the semiconductor physics, and the formation of pulse shapes.

isotope	$Q_{\beta\beta}$ [keV]	$T_{1/2}$ [yr]	experiment
^{48}Ca	4271	$4.4 \cdot 10^{19}$	Candles
^{76}Ge	2039	$1.8 \cdot 10^{21}$	GERDA, MAJORANA
^{82}Se	2995	$9.2 \cdot 10^{19}$	(Super)NEMO, Lucifer
^{96}Zr	3350	$2.3 \cdot 10^{19}$	(Super)NEMO
^{100}Mo	3034	$7.1 \cdot 10^{18}$	(Super)NEMO
^{116}Cd	2809	$2.9 \cdot 10^{19}$	COBRA
^{13}Te	2529	$6.9 \cdot 10^{20}$	CUORE, COBRA
^{136}Xe	2479	$2.2 \cdot 10^{21}$	EXO, Kamland-ZEN
^{150}Nd	3367	$8.2 \cdot 10^{20}$	SNO+

Table 2.4: Overview of the different $0\nu\beta\beta$ isotopes, their $Q_{\beta\beta}$ -value and half-life of the $2\nu\beta\beta$ decay; the experiments searching for the $0\nu\beta\beta$ decay in the respective isotopes are included as well.[17][28]

3

Particle detection with semiconductor detectors

This chapter describes how detectors made of semiconducting materials are used to detect particles and ionising radiation. Above all, germanium detectors have been used to detect radiation with very high precision since the 1960s. Silicon detectors have also been around for a long time and are now typically used as thin striped detectors for tracking of particle paths in collider physics. The physical interactions that take place when a detector is hit with ionising radiation or particles will be described below. The physics of semiconductors and the reverse-biased pn-junction as their working principle are explained in sections 3.2.1 and 3.2.2. GERDA is using the special pulse shape properties of a new detector type, the BEGe¹, to distinguish background reactions. The BEGe is named for its ability to reliably measure a broad energy range of gammas. This is due to its short, wide geometry and thin dead layer that allows low energy gammas to be detected, while still being large enough to detect high energy gammas. The last section of this chapter (3.3) deals with the process of signal formation that leads to distinguishable signals.

3.1 INTERACTIONS WITH MATTER

The way radiation² passes through matter and interacting with it and losing energy along its path that is deposited in some form in the detector material, is the fundamental principle on which all detectors of radiation are based. These principles govern the performance of particle detectors and their performance in respect to sensitivity, efficiency, and the types of

¹**B**road **E**nergy **G**ermanium

²According to quantum mechanics radiation always behaves like particles and particles always have a wave-character. So “radiation” will always comprise α - and β -particles, as well as γ -radiation.

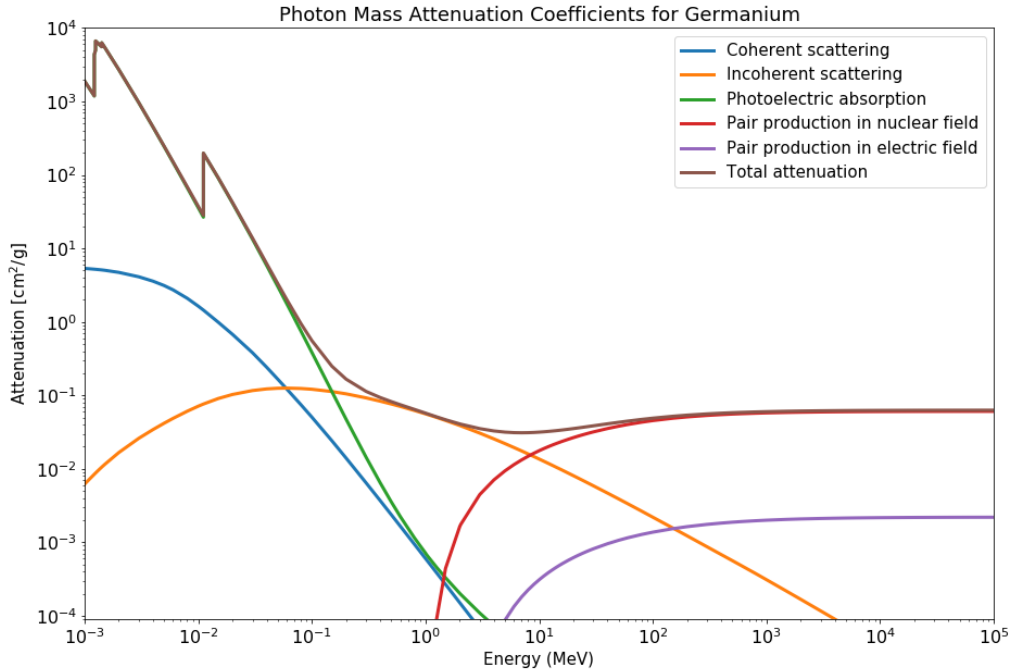


Figure 3.1: Mass attenuation coefficient for germanium. All processes contributing to the total mass attenuation of photons are included. [20]

particles they can detect in a certain energy range.

A charged particle ionises the material while it is passing through. Previously bound charges are separated and with the help of an applied electric field transported to the electrodes. At the anode or cathode, depending on the charge and on the detector technology used, these charges are collected and, with the help of electronic circuits, amplified and shaped into a signal which is then further treated with analogue or digital measurement electronics. The process how the pulse shape is formed and how it can be used for background discrimination is covered towards the end of this chapter.

The number of separated electron-hole pairs in the detector is proportional to the energy deposited, which again is proportional to the path travelled in the detector material. If the energy of the particle is low enough, or the detector large enough, the particle deposits its full kinetic energy in the detector and is stopped within the material. This principle is basically the same for other detector types. Instead of electron-hole pairs, in a gas detector electrons are separated from their then ionised atoms; in scintillation detectors molecules are excited by passing particles and emit photons. The number of photons is again proportional to the energy deposited, their wavelength depends on the material used.

The advantage of semiconductor detectors is their small band gap and connected with that, the low energy needed to create an electron-hole pair. This means that the number of separated charges per energy is larger than for other detector types. A larger number of electron-hole pairs means that statistical fluctuations have a proportionately smaller influ-

ence on the uncertainty of the measurement than techniques that produce smaller numbers of electron-hole pairs, or photons, phonons or any other medium that dissipates energy. Therefore, semiconductor detectors have a very good energy resolution and have thus been used in spectroscopy for a long time.

Other properties of the material like its density, number of neutrons and protons in the nuclei determine how quickly radiation is absorbed.

Semiconductor detectors are able to measure a variety of particles:

- charged particles like electrons, protons and α -particles
- photons (γ -rays and X-rays)
- neutrons

The detection efficiencies are very different for the various particles. Germanium detectors are mainly used for high precision spectroscopy of photons. With a germanium crystal of a few centimetres, an energy range from few keV to several MeV photons can be covered. The major processes involved in the detection vary depending on the different particles.

PHOTONS

The attenuation of photons in matter is mainly governed by three processes:

photoelectric interactions

An incoming photon with high enough energy is fully absorbed by a shell electron and consequently this K (or L) shell electron is ejected off the shell. The produced electron is called a photo electron. The vacancy is filled by an electron of a higher shell and an accompanying X-ray with characteristic energy is emitted. This process dominates for lower energies ($\lesssim 200$ keV) and happens between a photon and an entire atom.

Compton scattering

Takes place between a photon and a free electron. The angles θ and energies E follow the distribution of a two-body collision and the maximum transferable energy follows the relation

$$E_{max} = E \left(1 - \frac{1}{1 + \frac{(1-\cos\theta)E}{m_e c^2}} \right) \quad (3.1)$$

This leads to the typical characteristic energy spectrum of the Compton scattering: a full-energy peak, a depleted area between full-energy peak and Compton edge, the Compton edge and the Compton continuum (Fig. 3.2).

pair production

If the photon's energy exceeds 1022 keV, the production of an electron-positron pair in the vicinity of a nucleus becomes energetically possible. The production rate increases with higher energy. The positron and electron created each travel only a few millimetres

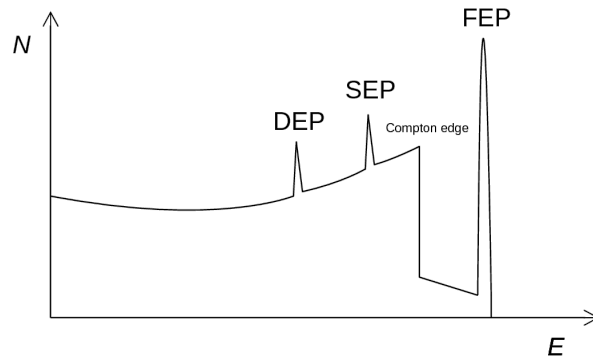


Figure 3.2: Schematic energy spectrum for Compton scattering. The full energy peak (FEP), single escape peak (SEP), and double escape peak (DEP) are depicted. [44]

in the material before having lost all kinetic energy. The positron then annihilates with another electron creating two photons of 511 keV. If one or two photons manage to escape the detector, their energy is missing in the total energy deposition and single- and double-escape peaks appear in the spectrum 511 keV and 1022 keV below the full-energy-peak.

Depending on the energy of the photon, these effects contribute in varying degrees as can be seen in Figure 3.1.

CHARGED PARTICLES

Charged particles, which for the field of germanium detectors can be limited to electrons, protons, and heavier ions (mainly α -particles), behave slightly different than photons when passing through matter. Bound electrons can be excited or removed from the ionised atom by passing particles. This reduces the energy carried by the particle by the amount needed for excitation e.g. ionisation. Another process is the elastic scattering off nuclei. This exchanges a lot of energy in case of the heavier particles since the impact partners have roughly the same mass. Electrons on the other hand lose less energy but are deflected to larger angles. This leads to shorter, straighter paths for the heavier particles and longer average path lengths for electrons. The penetration depth is roughly the same as the average path length for heavy charged particles; for electrons the penetration depths is a lot smaller than the average path length when compared to heavier particles due to the many deflections of the electron.

For high energies (>10 MeV) *Bremsstrahlung* becomes the dominating effect, at least for electrons. *Bremsstrahlung* is the resulting radiation that is emitted when the momentum of a charged particle is changed in the electro-magnetic field of a nucleus.

Neutrons are another category of particles that can be detected by semiconductor detectors. The detection efficiency is very low for neutrons, since all electro-magnetic interactions that deposit energy in case of charged particles are not applicable for the neutral neutrons and mainly elastic scattering contributes to the cross section. Neutrons are not relevant for this thesis and will not be considered here.

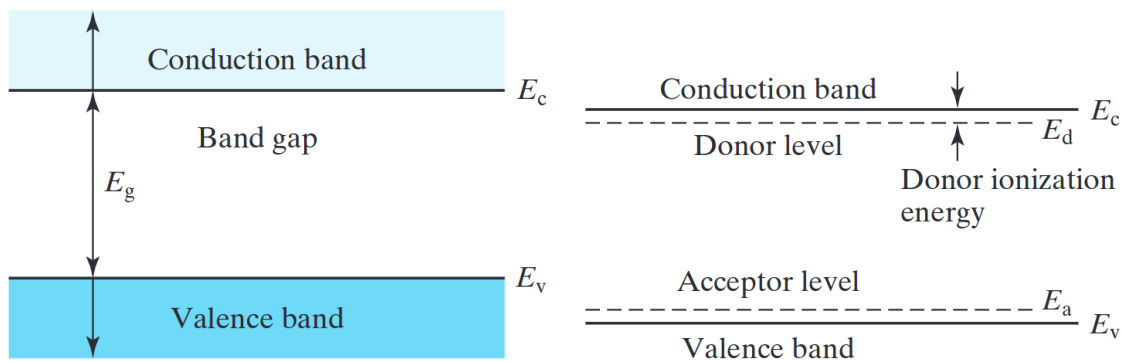


Figure 3.3: Sketch of the valence and conduction bands in semiconductors. Additional levels are added by doping the crystal with donor or acceptor atoms, turning the crystal into a n- or p-type semiconductor. [37]

3.2 GERMANIUM DETECTORS

The effects and interactions of particles with matter were described in the previous chapter; this chapter deals with the techniques employed to turn the charges separated by the passing particle into a measurable signal by using and instrumenting semiconductor detectors. This signal then corresponds to the energy deposited in the detector.

The basics of semiconductors, pn-junctions, and the operation mode of a semiconductor detector will be explained in the following; as well as how the signal is formed, how the signal shape can be used to distinguish different particles, and how the noise characteristics affect the performance of the germanium detector.

3.2.1 SEMICONDUCTOR PHYSICS

In solid state physics the quantum mechanical model of discrete shells, energy states and fixed number of possible states of free atoms has to be extended. The wave functions of the valence electrons overlap and form bands of many, many energy levels. The Fermi level separates the valence band from the conduction band. At 0 K, the valence band is completely filled with electrons, while the conduction band is totally empty. For metals, the two bands overlap, while the band gap in an insulator is fairly large. This leads to the well-known electric properties of these two kinds of material. In case of a semiconductor, the bands are separated, but not so far that the conduction band is not slightly populated by electrons that get their energy from (ambient³) temperature.

Typical semiconductors like germanium and silicon are elements from Group IV and therefore have four valence electrons. By doping a semiconductor crystal with atoms from either Group III or Group V, boron and phosphorus are typical examples, extra atoms are incorporated in the lattice. Phosphorus has five valence electrons, while the surrounding silicon only has four. The extra electron needs very little energy to be lifted in the conduction band. This

³or non-zero for that matter

type of dopant is called a donor. The small energy difference $E_c - E_d$ is the energy needed to free one electron. An energy level close to the conduction band is created. The analogue principle holds true for acceptor dopants that accept electrons, thereby creating a hole in the valence band. The energy $E_a - E_v$ is the energy needed to receive an electron and is slightly above the valence energy E_v . These extra energy levels increase the number of charge carriers in the conduction band and therefore the conductivity, because at a finite temperature this small energy difference will be easily overcome by a number of charge carriers. In case of a dopant of Group V, the charge carriers are electrons and the resulting semiconductor is n-type; if the doping agent is from Group III, the material will be p-type with holes being the majority charge carriers. The concentration of (induced) impurities governs the number of available charge carriers. In reality, a semiconductor crystal always contains acceptor and donor atoms; the density of free charge carriers being governed by the net charge carrier difference:

$$p_0 \approx N_d^+ - N_a^- \quad (3.2)$$

$$n_0 \approx N_a^- - N_d^+ \quad (3.3)$$

with N_d^+ being the donor and N_a^- the acceptor concentration.

Heavily doped semiconductors (n^-/p^+) can be considered conductors, and heavily doped regions of a diode are usually used as an electrode to electrically connect the detector to the read-out electronics.

3.2.2 PN JUNCTIONS

The good suitability of germanium detectors to do high-resolution spectroscopy is based on the small amount of energy that is needed to create electron-hole-pairs. The small band gap of 0.67 eV (at 273 K) helps to ensure that the mean energy needed to create an e^- - h -pair is only around 2.9 eV. Yet with all the free charge carriers from the donors/acceptors it would be impossible to recognise a small signal from ionising radiation over the background of charge fluctuations. Therefore, the material has to be depleted of free charges.

In microelectronics, bringing a p-type and n-type semiconductor together to form a pn-junction, is the basic building block of almost all advanced electronics. While in microelectronics the challenge is always to miniaturise structures and to squeeze more transistors on a chip, in particle physics the challenge is to produce big and yet reliable detectors. Applying a bias voltage and creating a depletion zone helps in removing free charge carriers from the crystal. Semiconductor detectors, thus, are basically big pn-diodes with an applied high voltage. Since the pn-junction and its reverse bias operational mode are the basic principles for radiation detection with a semiconductor, they will be briefly explained in this section.

When a p-type semiconductor is brought into contact with a n-type, holes and electrons are diffusing in the material of the other type. There, they recombine, leaving behind charged ions which build a potential that inhibits further diffusion. The region along the p-n contact

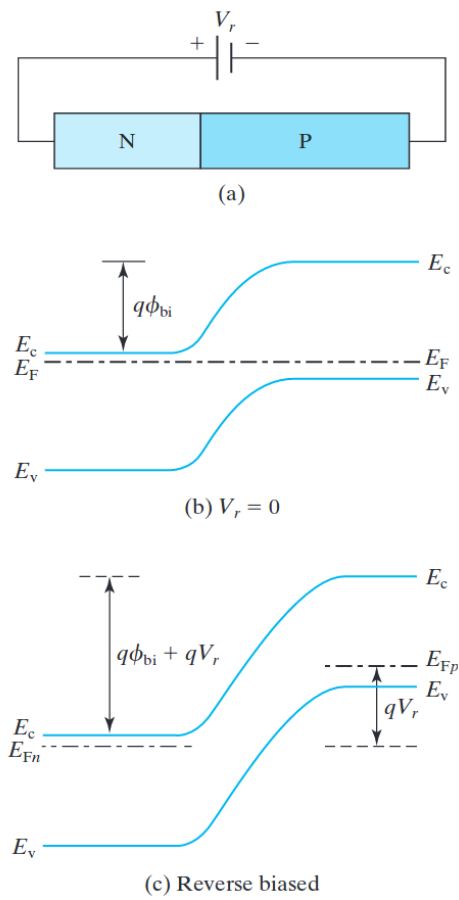


Figure 3.4: pn-junction with reverse bias voltage. (a) polarity of voltage (b) energy band with no applied voltage $V_r = 0$ (c) energy band with applied voltage in reverse direction.[37]

is called the space charge region or depletion layer, since it is almost fully depleted of free charge carriers.

When a reversed bias voltage is applied as in Figure 3.4 c), the holes of the p-type semiconductor are pulled towards the negative contact of the power supply, while the electrons see a positive potential that pulls them away from the depletion zone as well. Consequently, the depletion layer increases, the resistance rises and only very little current flows over the pn-junction. Semiconductor detectors operate in this reverse-bias-state when detecting ionising radiation. As described above in chapter 3.1 particles as well as ionising radiation create electron hole pairs when they deposit energy in the detector. These electron hole pairs are separated by the applied voltage and drift towards the electrodes of opposite polarity. This current can be measured and is proportional to the energy deposited.

In order to make the whole detector sensitive to radiation, the voltage applied has to be sufficiently large to deplete the whole crystal. For typical germanium detectors with sizes of a few centimetres in diameters as well as height, this means that the applied voltage has to be in the range of a few kV. Additionally, the detector cannot operate at room temperature, since the conducting levels of the doped semiconductor can be populated with a reasonable probability at that temperature. This would create extra electron hole pairs that would be separated and drift along the electric field. This leakage current would increase dramatically and drown out the signal current induced by the gamma rays. The purity of the crystal prevents scattering off impurities and recombination of electrons and holes, thus guaranteeing a better signal to energy proportionality.

3.3 SIGNAL FORMATION

When charges are separated by a gamma ray (or a charged particle) in a semiconductor detector, they form a small cloud of free charges which consequently start drifting along the electric field lines towards the electrodes of opposite charge. Depending on the design of the detector the electrodes might be structured in different ways. Figure 4.3 schematically shows the two types of detectors used in the GERDA experiment. While both types have one electrode on their outer skin, the semi-coaxial uses the inside of its borehole as the second electrode. The BEGe-type on the other hand has its contact on the bottom of the flat cylindrical shape, which is much more point-like than with the semi-coaxial type. This creates an E-field which is a lot more inhomogeneous than that of the semi-coaxial detectors. The signal gets induced in the read-out electrodes when charges travel through the weighting potential of the detector is described by the Shockley-Ramo theorem:

$$i = E_v q v \tag{3.4}$$

with E_v being the component of the electric field in direction of v . The drift velocity is dependent on the type of the charge carrier, the applied voltage and also the orientation of

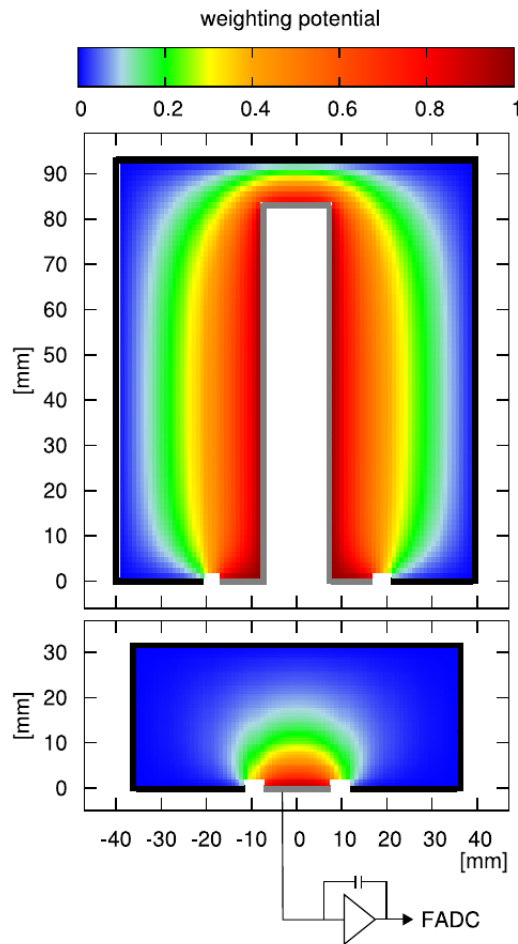


Figure 3.5: Weighting potential for semi-coaxial and BEGe germanium detectors.

the crystal axes. The electric field E_v is connected to the weighting potential $\psi(\vec{x})$:

$$E_v = -\nabla\psi(\vec{x}). \quad (3.5)$$

The Shockley-Ramo theorem allows to calculate the induced electric current of a moving charge. The theorem states that for the calculation of the induced current only the electric field induced by the applied voltage is relevant, all charges inside the detector can be neglected for the calculation.

For the weighting potential $\psi(\vec{x})$ it is assumed that all charges are removed from the detector, the considered electrode's potential is set to one, the potential of all other electrodes is set to zero. In other words it is enough to know the trajectories of the charges, as pictured in Figure 3.6, and the potential created by applying a voltage to the electrodes. The internal charge carriers do not matter for the signal formation.

The weighting potentials of the two detector types used in GERDA are pictured in Figure 3.5. Especially for the BEGe-type, it has to be noted, that the weighing potential is largest close to the point-contact and very small everywhere else. This is where most of the signal is created

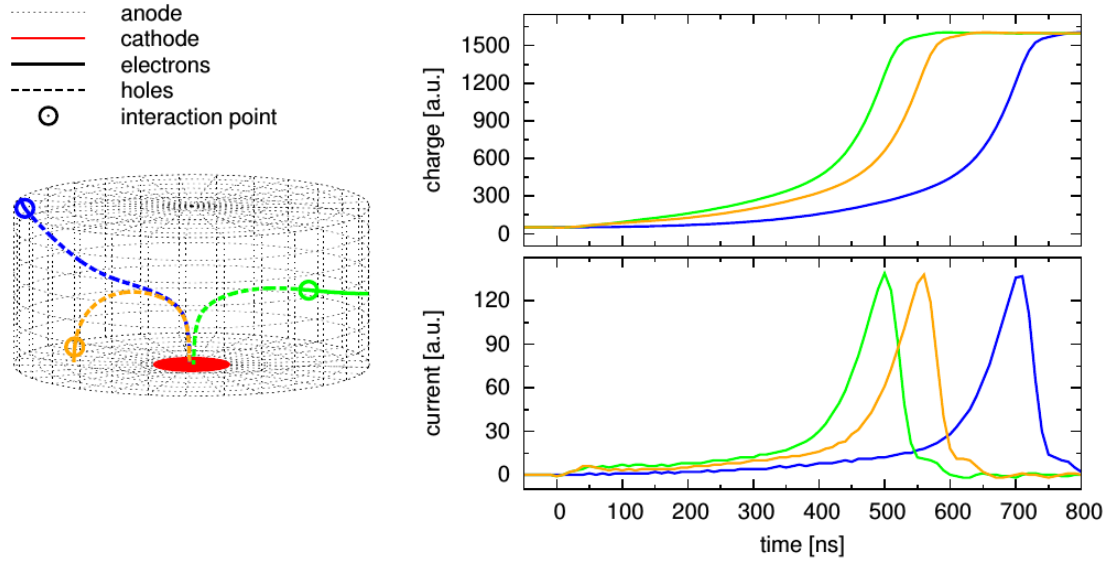


Figure 3.6: Different locations of interaction points in the detector lead to different trajectories of the charge cloud. This in turn leads to different arrival times.

and this effect makes for the unique characteristics of the BEGe. Almost all trajectories are funnelled towards the point contact and approach the electrode in similar trajectories. This means that it does not matter if the interaction occurred in the far corner of the detector or closer to the center, the signals will look very similar. Of course, looking even closer, the signal shape does depend on the exact position, for example a small leading tail is added when the trajectory is very long, or rises a lot quicker when the interaction is close to the point contact. Different pulse shapes for different starting points of the trajectories are shown in Figure 3.6. These pulses are taken from a simple simulation and it has to be noted that the time shift notable in the pulses would not be visible in a real experiment, since the start time would not be known. The properties of the BEGe detector type regarding multi-site events and the possibilities to do pulse shape analysis by taking advantage of its behaviour to separate single-site from multi-site events is described in the next section (sec 3.4).

3.4 PULSE SHAPE DISCRIMINATION

In the previous section 3.3 the way a signal forms was explained for the case that there is a single interaction point. Interactions induced by gamma rays often deposit energy in two or more places within the detector. While these interactions practically happen at the same time, drift times may vary substantially for different locations within the crystal. The drifting charges arrive in the vicinity of the electrode, where the majority of the signal formation happens, at slightly different times. The time shifted partial signals are superimposed to form a total signal which is proportional to the total energy deposited. But additionally the shapes of the signals coming from a single-site event now differ slightly from those created by

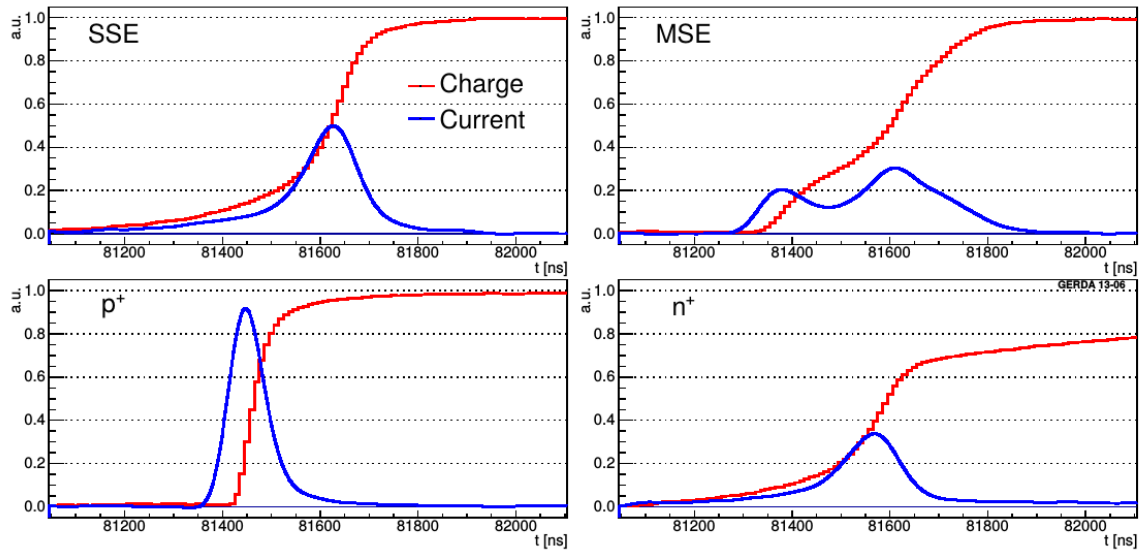


Figure 3.7: Pulses originating from different physical processes produce different waveforms. Pulse shape and corresponding current signal from a single site event (SSE) and a multi site event (MSE) in the top row. Signals from an event close to the p^+ contact and close to the n^+ dead layer are shown on the bottom row. [9]

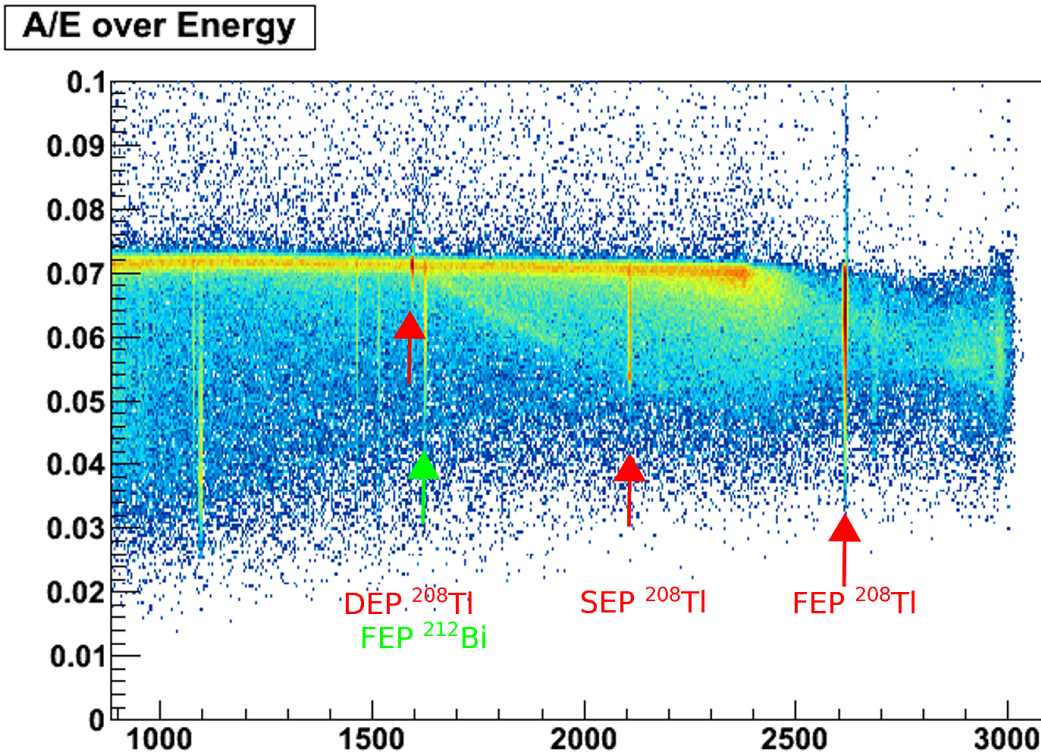


Figure 3.8: The parameter A/E is displayed over the energy for a Th-228 measurement. The MSE-like full energy peak (FEP) of ^{208}Tl at 2614 keV and the SSE-like double escape peak (DEP) at 1592 keV particularly catch the eye. The single escape peak (SEP) of ^{208}Tl is also displayed, along with the FEP of ^{212}Bi at 1620 keV. The FEP of ^{212}Bi and the DEP of ^{208}Tl are often used to test pulse shape discrimination techniques since they have very similar energies, one is MSE-like, the other SSE-like.

multi-site events. This is most obvious when not considering the charge signal, but its time derivative, the current signal. Taking the maximum of the current signal A and normalising by the total energy E serves as a good parameter to classify the two different event types. But this A/E method can also recognise very slow or very fast pulses as they might be produced when particles penetrate the lithium diffused outer layer or directly the p^+ electrode. These are usually unwanted e^-/e^+ or even α -particles. The multi-site events from the gamma rays can be effectively distinguished as well. These four classes of pulses are pictured in Figure 3.7.

When looking for the $0\nu\beta\beta$, which is expected to be an almost point-like interaction, this pulse shape method can help to reduce unwanted background. The BEGe type detector is particularly suited for this discrimination technique, since its small electrode at the bottom centre of the detector leads to a field that can produce long and different drifts paths depending on the location of the interaction. Hence, events with single or multiple interaction sites produce different signal shapes with different A/E parameters, which can be used to discriminate MSE from SSE.

Figure 3.8 shows the A/E parameter over the energy for a ^{228}Th measurement. The decay chain of ^{228}Th includes ^{208}Tl , which produces gammas with the highest energy from naturally occurring isotopes at 2614 keV. ^{228}Th measurements are used to determine the pulse shape characteristics of the germanium detectors and to check and evaluate the discrimination method and the efficiency of the cuts. The full energy peak of ^{208}Tl at 2614 keV shows a wide range of A/E parameters. This is due to the FEP's strong multi-site characteristics. The high A/E values can be explained by the a significant percentage of gamma rays penetrating the detector deeply and depositing their energy close to the p^+ contact, where due to the field characteristics a very fast signal pulse is produced. The SSE-like double escape peak is due to pair production occurring upon first contact of the gamma with the detector material, the resulting positron annihilates, and both 511 keV gammas produced by the annihilation escape the detector without further energy deposition. The DEP is therefore located at $2614 \text{ keV} - 2 \cdot 511 \text{ keV} = 1592 \text{ keV}$. At 1620 keV, there is another full energy peak from ^{212}Bi which stems also from the thorium chain. These two peaks are often used to test pulse shape discrimination performance since they have similar energy, only that one contains mainly SSE, the other MSE.

The tests of the pulse shape discrimination method unfortunately cannot discriminate very well on the location of the interactions. Tests with collimated low energy gammas can be done, but they only penetrate a few millimeters. Higher gamma energies penetrate deeper, but the positional information is lost. Thus, statements about the quality of the technique can only be made considering all events of a measurement. So SSE events occurring in the corner of the detector contribute almost as much to the total spectrum as events happening close to the electrode, even though their pulse shapes are expected to be different. This would lead to a different discrimination potential across the detector, yet the efficiency given by such a measurement is based on the distribution of single site events inside the detector

depending on the position of the Th-source. This work describes a method to measure the interaction point inside the detector and assign it to the corresponding waveform.

4

The GERDA experiment

“The main thing history can teach us is that human actions have consequences, and that certain choices, once made, cannot be undone.”

Gerda Lerner

4.1 SETUP

The GERDA experiment is located in Hall A of the Gran Sasso National Laboratory (Laboratori Nazionali del Gran Sasso, LNGS) and the experiment is aimed at the detection of the neutrinoless double-beta decay. It uses germanium detectors that are enriched in the isotope Ge-76. This isotope is a possible candidate for the proposed $0\nu\beta\beta$ decay. Since the effect, if it exists, is small, all possible measures to reduce backgrounds have to be taken. The location at the LNGS was chosen because the underground site is shielded by 3500 m w.e. of rock. This reduces backgrounds induced by direct or indirect muon exposure by a factor of $5 \cdot 10^5$ [15]. But cosmic radiation is not the only background to worry about. Natural radioactivity can as well introduce signals that would wrongly be identified as coming from the $0\nu\beta\beta$ decay. The maximum energy of the natural thorium chain of 2614 keV is larger than the energy endpoint of the double-beta decay; all energies below the 2614 keV can possibly be detected by the germanium crystal and obscure the measurement. The GERDA experiment, like many other low background (astro) particle physics¹ experiments, has chosen a multi-layered shielding

¹since the neutrinoless double beta decay is a general particle physics effect with no extraterrestrial particles involved except as background, this prefix might be debatable. But because the physics involved and the techniques applied are similar, the “astro” prefix is often used to refer to the $0\nu\beta\beta$ field, too

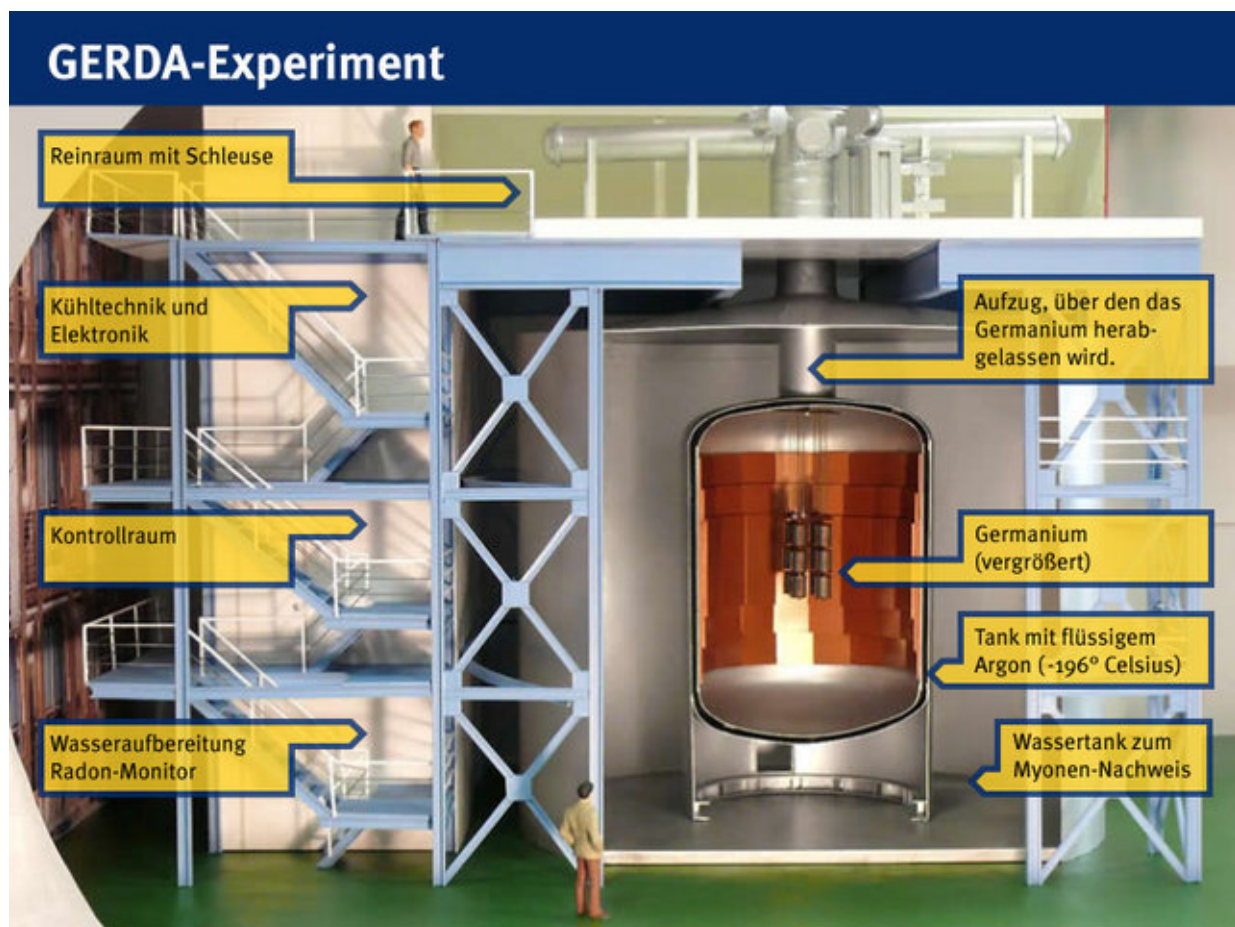


Figure 4.1: The structure of the GERDA experiment at Gran Sasso Laboratory

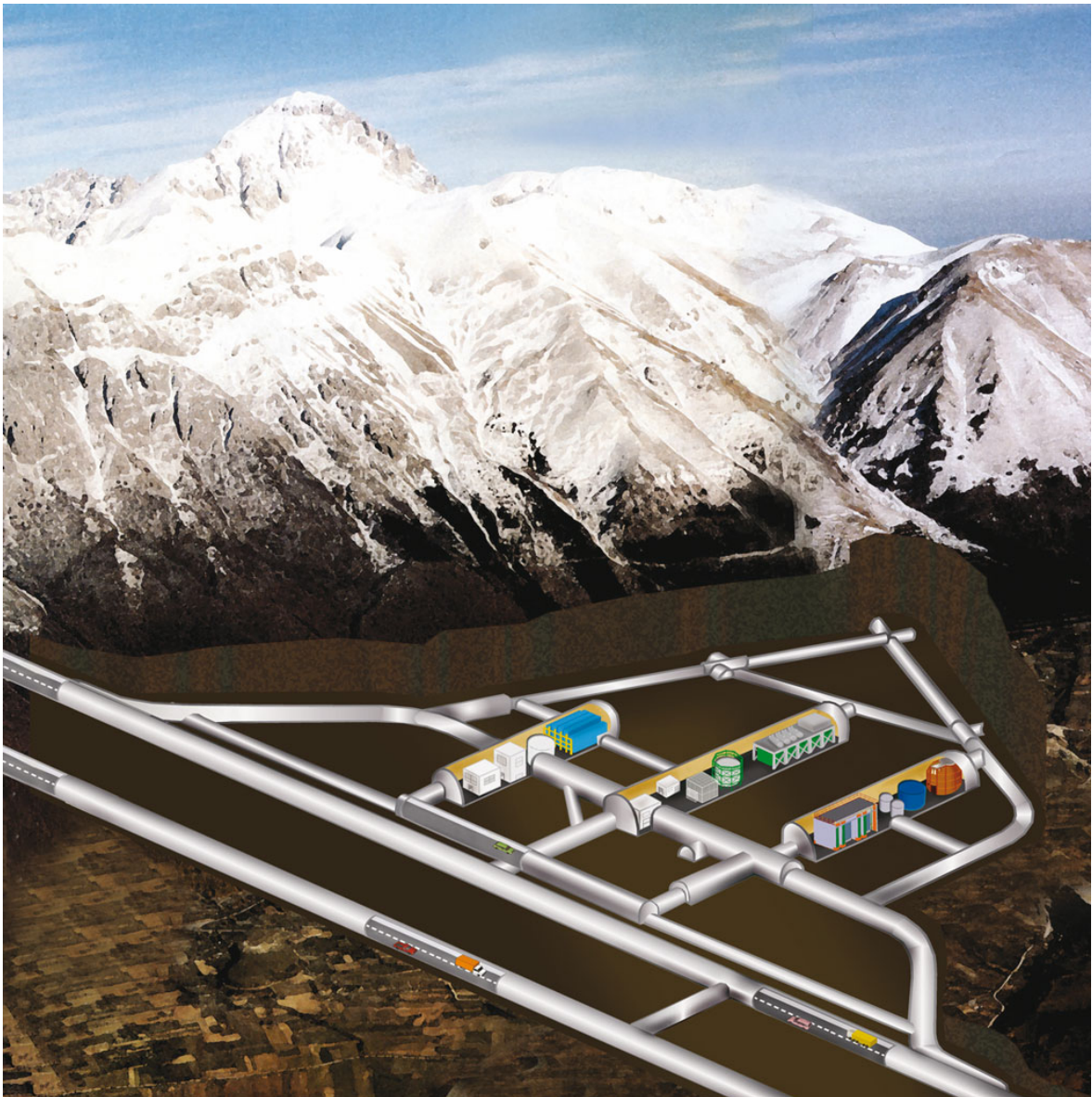


Figure 4.2: The Laboratori Nazionali del Gran Sasso (LNGS) under the Gran Sasso massif.

design. One layer of this shielding design is the above-mentioned location at the underground lab to shield against cosmically produced muons. The first actual, physical layer is a steel tank with a diameter of 10 m and a height of 8.3 m, which is filled with 590 t of purified water, supplied by the BOREXINO experiment [6]. This serves as a shield against neutrons, due to the high number of protons in the water. But also γ rays are shielded, even though the Z is not very high, but the sheer mass and distance help to shield most gammas coming from the outside. The water tank is also instrumented to serve as an active detector by 66 photomultipliers attached to the walls. They detect light emitted by muons passing through the water tank very efficiently down to single photons. The muons travel at speeds almost at the speed of light and do not slow down considerably when passing through water. The Cherenkov effect describes the emittance of a cone of light by particles passing through mat-

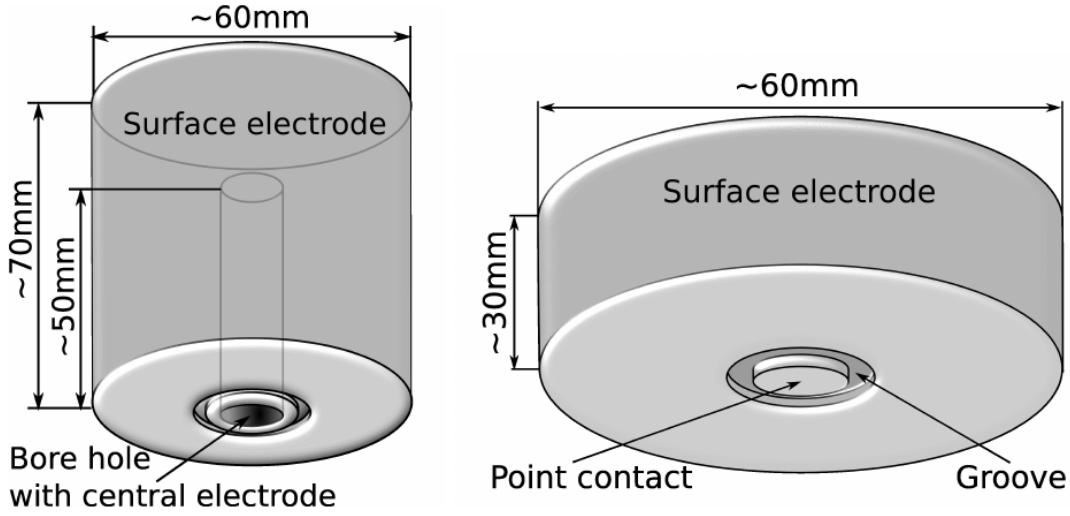


Figure 4.3: Sketch of the two types of germanium detectors used in GERDA. A semi-coaxial detector on the left and a flatter BEGe with enhanced pulse shape capabilities on the right.[53]

ter with speeds higher than the speed of light (in that medium). Muons are detected via their photon emission and this signal is used to veto the germanium detectors, so that no signal can be induced in the germanium that came from a muon. Additionally, plastic scintillator panels are installed on top of the cleanroom to take care of the last insensitive spot of the muon veto. The neck of the cryostat, which is used to get the detectors in and out and to lower calibration sources into the cryostat, is not covered by water and vertical muons could potentially strike a detector without being detected by the water-Cherenkov veto.

The relatively small detectors by comparison to the whole structure of the experiment are submerged in a tank of liquid argon, that is placed at the centre of the water tank. The high- Z argon is a better gamma absorber than the water and is supported in its shielding efforts by copper plates fixed to the inside of the argon cryostat. The liquid argon is kept at a temperature of 87 K, which serves the Ge-detectors well. The low temperature is needed to operate the semiconductor detectors and assure a minimal leakage current.

The experiment makes use of the source-detector principle. Germanium detectors enriched in ^{76}Ge serve as the source of the $0\nu\beta\beta$ decay as well as the detector. The efficiency to detect such a decay is therefore very close to 100%. The downside is that the region of interest, the endpoint of the double-beta spectrum of ^{76}Ge is at $Q_{\beta\beta} = 2039$ keV and hence below many natural decays. To achieve an absolute radio-pure environment, careful selection and screening of the materials used, and very considerate working are required.

The experiment has been proposed in 2004 [5], built in 2009-2011, and official measurements have started in November 2011. A first measuring phase has ended in 2013 and a first result has been published, excluding the $0\nu\beta\beta$ decay with the highest sensitivity, so far. A second measurement phase has been started, in which the number, total mass and design of the detectors used have been increased. The sensitivity of GERDA will be covered in the next

session, while the first published result will be discussed in section (4.3).

4.2 SENSITIVITY AND BACKGROUND

The sensitivity for GERDA, that means the discovery potential to observe the decay as a function of the different experimental parameters, is given by

$$S(T_{1/2}^{0\nu}) \propto \frac{\epsilon \cdot f_{76}}{m_A} \sqrt{\frac{Mt}{BI\Delta E}} \quad (4.1)$$

where the variables denote:

- ϵ efficiencies (incl. detector eff., dead layer, ROI eff.)
- f_{76} enrichment fraction
- m_A atomic mass
- M detector mass
- t live time
- BI background index
- ΔE energy resolution

This equation illustrates very clearly that there are several different leverages in order to improve the sensitivity of the experiment. An increased lower limit of the half life $T_{1/2}^{0\nu\beta\beta}$ of ^{76}Ge is considered an improvement in case of a non-discovery. While, obviously, in the case of a discovery of the $0\nu\beta\beta$ decay, the detection of this decay and the measurement of its half-life are the goal of the experiment. The isotope has been chosen already, hence the atomic mass m_A is fixed. Likewise, the efficiency ϵ is pretty much fixed. Due to the chosen *detector as source* design, with the ^{76}Ge inside the detector, the efficiency is already very close to 100%. Only the thickness of the dead layer covering the outside of the detector plays a role for the efficiency. If a possible $0\nu\beta\beta$ event would (partially) deposit energy in this dead layer, the energy read out by the detector would be smaller and the event, therefore, would not be attributed as a $0\nu\beta\beta$ event, thus lowering the efficiency. The next parameter to tune is the enrichment fraction f_{76} of the ^{76}Ge -fraction of the total mass of the Ge-detectors. Naturally, germanium contains a fraction of 7.75% of ^{76}Ge . This fraction is increased to 86% with time-consuming and costly enrichment procedures. The more obvious parameters to improve the experiment are mass M and live time t . While of course it is aimed to increase the mass, i.e. the number of detectors, and measure as long as possible, these parameters are subject to cost and time considerations. The remaining two parameters are the energy resolution ΔE and the background index BI . Germanium detectors generally are capable of giving a very good energy resolution in the order of $\sim 2\%$ (FWHM). This is an advantage over other photomultiplier-based $0\nu\beta\beta$ experiments that might be dealing with a more favourable energy-endpoint of their isotope, but are subject to a much worse resolution in their energy determination. The energy resolutions possible with a photomultiplier depend

on the scintillator used, but are typically in the 5-10 % range. Adding to the already good resolution of Ge-detectors, the filters that determine the energy value from the recorded waveform have been improved for GERDA to enhance the total energy resolution even further [12]. The background index, i.e. the number of counts attributed to background processes in a defined energy window, is probably the most important parameter in order to improve the efficiency of low-count experiments. The number of background events superimposes the already small number of signal events and might make it impossible to detect a signal, when the BI is too high. The background index can be brought down by two methods. The passive method is to try to eliminate possible background sources like natural radioactivity in the vicinity of the detector, shielding, running the experiment in a location sheltered against muons. The active method is to use additional detectors or analysis techniques to differentiate signal from background events. In the case of the GERDA experiment, an active muon veto in the form of a photomultiplier based water-Cherenkov detector is used to be able to determine possible event candidates that were produced by direct muon hits or their spallation products. Candidates for background events are tagged and it is then possible to remove the tagged events, or a certain class of them, from the data.

Additionally, a technique to distinguish background-like events with multiple hits in the germanium detector from signal-like events with only one confined region of energy deposition is utilised in the experiment. In GERDA, this can be done by analysing the shape of the pulses recorded by the detectors. Different types of events produce slightly different waveforms. The theory of signal formation in semiconductor detectors and the standard method in GERDA to distinguish them are described in sections 3.3 and 3.4, respectively. Signal-like events induced by the neutrinoless double beta decay produce a charge cloud that is limited in size, because the produced electrons are captured within a few millimetres. Events that are induced by background events, typically a gamma from a nearby decay, often have multiple interaction points within the detector. At each interaction point, a small charge cloud is produced, but when these charges drift to the electrode a time offset in the arrival time is realised. The resulting waveform that is read out at the electrode is a composition of two or more single site waveforms with a small time shift relative to each other. The resulting shape of the waveform is used to distinguish these two types of events.

Phase II of GERDA will mostly consist of detectors that are specifically used for their pulse-shaping properties. Phase I only had a few of this type of detectors, and it was tried to compensate the lacking pulse-shape capabilities by advanced neural-network pulse shape discrimination techniques.

More on the first published result and how the published numbers were compiled is presented in the next section.

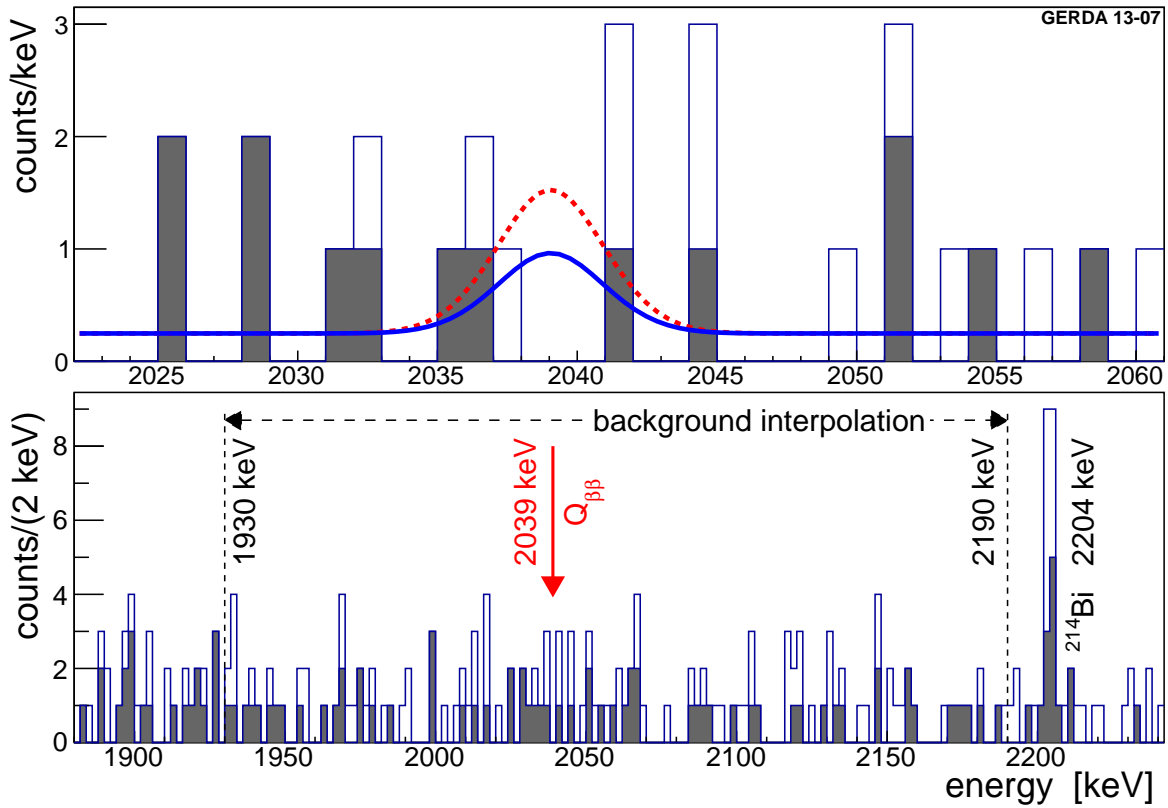


Figure 4.4: First results of the GERDA experiment. A discovery could be ruled out and a previous claim of Klapdor et al[39] could be refuted. The half life of the $0\nu\beta\beta$ decay is $T_{1/2}^{0\nu\beta\beta} > 2.1 \cdot 10^{25}$ yr @ 90 % C.L. [10].

4.3 FIRST RESULTS

The GERDA Phase I ran from November 2011 till May 2013 with a total exposure of 21.6 kg·yr of ^{76}Ge [10]. The experiment started with eight semi-coax detectors that were reused from the HDM and IGEX experiments and a mass of 17.67 kg. In July 2012 five BEGe detectors were added that were originally meant to only enter in Phase II. Several detectors and time ranges had to be excluded over the whole measuring cycle due to failures or instabilities. The energy calibration was done every one or two weeks by inserting ^{228}Th sources mounted on a pole into the liquid argon. The position of the energy peaks was realigned and the resolution was checked. No major deviations were found in between calibration cycles (<0.15% deviation in gain).

A blinded analysis approach was chosen to prevent any possible bias in selecting and implementing cuts, parameters and event selection. This was done by choosing an energy region with a width of 40 keV around $2039 \text{ keV} \pm 20 \text{ keV}$ and excluding events contained in this energy region from the analysis processing. Only after the background model[11](Fig. 4.5) and the energy calibration parameters were fixed, the window was opened and the events were processed. Except for an even smaller window right around the endpoint energy ($\pm 5/4 \text{ keV}$ for coax/BEGes), which was not opened until the parameters for the pulse shape

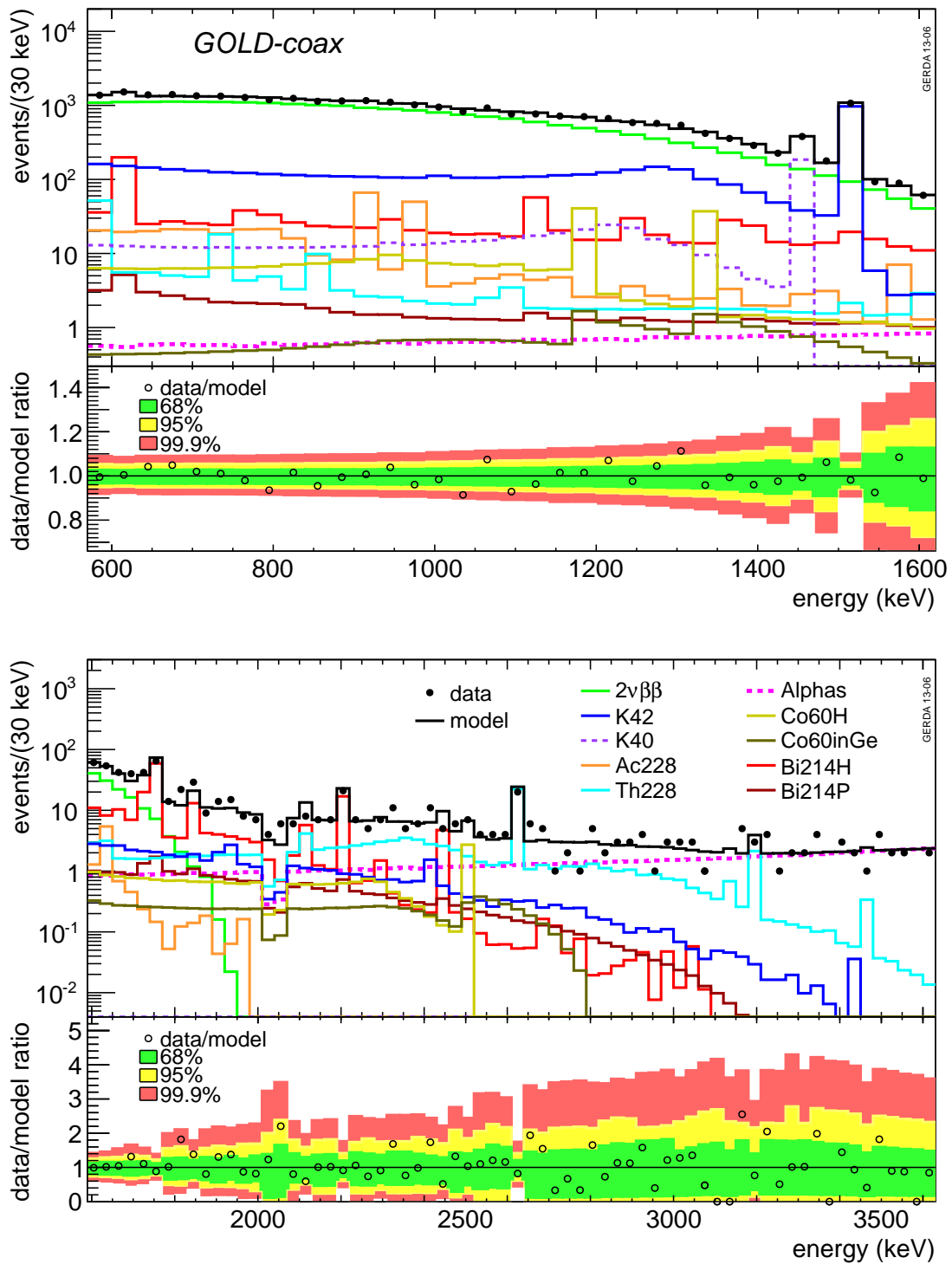


Figure 4.5: The expected background has been heavily studied and simulated. A fit to the measured data is shown for different energy ranges. The top graph of each figure depicts the different components of the background, the bottom graph describes the deviation of the model from the measurement. [11]

analysis had been decided on. For the two different detector types, two different approaches were chosen. For the BEGes with their inhomogeneous electric field and the very different drift times, it was possible to just fix a value of the parameter A/E , as it was described in chapter 3.4. The numeric value of the A/E -cut parameter is determined via survival probabilities of the DEP (double escape peak) of the ^{208}Tl from calibration data. The semi-coaxial detectors have multi-site events that are harder to distinguish from single-site events. The A/E approach would not work and there were three competing methods applied. The artificial neural network (ANN), the likelihood-ratio and the model that took A/E and the pulse asymmetry into account, all came up with very similar results. $\sim 90\%$ of events rejected as background-like were also rejected by the other two methods [10].

The experiment took data for a total exposure of $21.6 \text{ kg} \cdot \text{yr}$, applying these discrimination techniques and using the A/E method for the BEGe detectors a lower limit for the half-life of the $0\nu\beta\beta$ decay was found with 90 % C.L. to be:

$$T_{1/2}^{0\nu\beta\beta} > 2.1 \cdot 10^{25} \text{ yr} \quad (90\% \text{ C.L.}) \quad (4.2)$$

This was the best limit at the time and the experiment was able to rule out a former claim for the $0\nu\beta\beta$ decay of parts of the Heidelberg-Moscow collaboration[39].

In 2017, the results of GERDA Phase II were published. Not only was the collaboration able to further increase the exposure to $34.4 \text{ kg} \cdot \text{yr}$, but the background index was further reduced by roughly an order of magnitude by including another active veto in the liquid argon, so that there were actually no background events detected in the region of interest, making the experiment virtually background free[22]. The lower limit for the half-life of the $0\nu\beta\beta$ decay could be increased to

$$T_{1/2}^{0\nu\beta\beta} > 5.3 \cdot 10^{25} \text{ yr} \quad (90\% \text{ C.L.}) \quad (4.3)$$

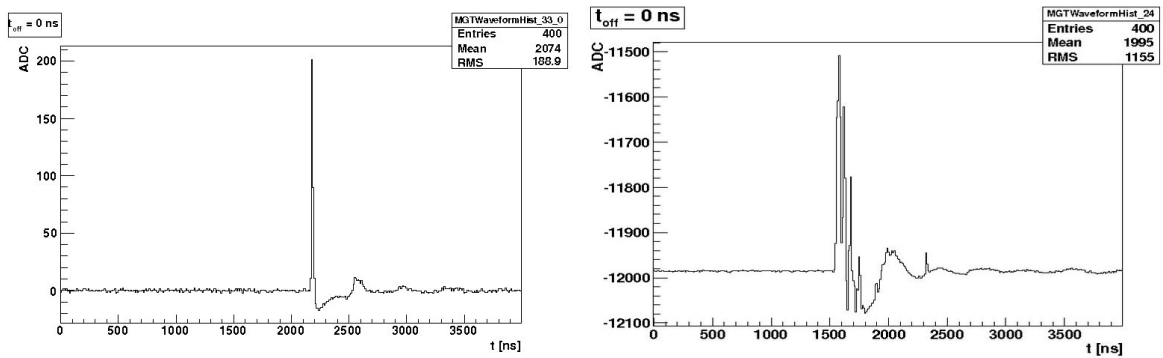
5

Deconvolution of PMT Signals

“And Now for Something Completely Different“

— Monty Python

Minimising background of all sorts is tremendously important when performing low statistics experiments. In the previous chapters various means to keep distracting events to a minimum have already been presented. Among them are the choice of location and passive shielding materials; the detectors are run at the Gran Sasso Underground Lab, and are shielded by multiple layers of water, copper, and liquid argon. An immense effort has been carried out to guarantee the radiopurity of the detectors and the structure holding them as much as possible. In addition to these passive shielding techniques, a few supplementary active techniques are being employed to lower the background index of the experiment. The pulse shape discrimination as described in chapter 3.4 uses different signal shapes due to different drift times to distinguish multi-site gamma events from single-site events that possibly are created by a neutrinoless double beta decay. While the pulse shape discrimination method is applied on events recorded in the germanium detectors, other active techniques can be used to minimize the background index as well. A very basic yet effective technique that is mainly aimed at reducing background from muons is the instrumentation of the surrounding water tank with photomultipliers (PMs). Muons deposit roughly 2 MeV/cm of energy along their track through matter and depending on their path they can deposit any amount of energy in the detector including the sought after 2039 keV. Whenever a muon passes through the water tank, Cherenkov radiation is emitted, which is picked up by the photomultipliers. At this exact time, a veto signal is sent out telling the DAQ to ignore a possible coincident event in the germanium detectors. This chapter describes a deconvolution technique that



(a) A clear single-PE pulse including a characteristic drop in signal after the pulse. (b) A signal containing multiple pulses with pulse heights corresponding to several PEs. The different pulses overlap due to different timing and reflections in the tank.

Figure 5.1: Two pulses representing typical signals for the calibration mode and for the veto mode.

allows to analyse waveforms recorded by PMTs (photomultiplier tubes) in high and low light domains with the same method. Prior to this, two different approaches were used to analyse calibration and physics runs. In addition, waveforms are calibrated in units of photo electrons when using the described approach. While this technique is not directly related to the PET-germanium experiment that the following chapters are dealing with, in the end both topics have the goal to reduce the background index in the GERDA experiment.

The GERDA muon veto was planned, simulated, built, installed and analysed by the Tübingen GERDA group [40][51][28]. It consists of 66 photomultiplier tubes with a diameter of 8". They are arranged in four rings on the walls and three rings on the floor of the water tank, where the innermost ring is comprised of 6 PMTs and is located within the so-called pillbox in a separate volume under the argon tank. The inside of the water tank is covered with highly reflective VM2000 foil¹ to increase the light yield. To calibrate and test the photomultipliers, five diffuser balls connected to a pulsable LED via an optical fibre are installed within the tank. The pulsing frequency as well as the intensity can be externally controlled and the coincident signals in the PMTs can be analysed. This is done to be able to check the amplification factor of the photomultipliers and correct any possible drifts in this factor by adapting the voltage.

In calibration mode, the LED is dimmed to a level that only one photon arrives at a time. The single photon peak created thereby is used to calculate the amplification. Since the photon emission process and the subsequent passage through the water are governed by Poisson statistics, the LED has to be set to a level where on average only ≈ 0.2 photons arrive on each pulse. This means that in less than one in five cases a photon is observed, but it mainly prevents the calibration measurement from being polluted by two or more photons

¹VM2000 foil used to be produced by 3M, but production has since been discontinued.

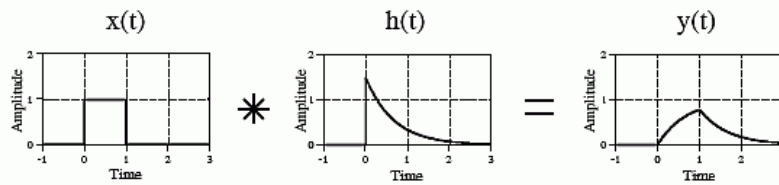


Figure 5.2: The principle of a convolution. In this case, this would be the original point-like signal of the photo electron $x(t)$ and the response function of the detector $h(t)$ resulting in the signal that is actually recorded $y(t)$. For deconvolution the order is reversed.

arriving at the same time².

Yet in the normal veto mode, the photomultipliers can see much higher signals from very energetic muons with photons arriving at different times due to the reflections in the tank. A typical signal for a single photon calibration signal is shown in Figure 5.1a, while a more luminous signal produced by a muon is shown in Figure 5.1b.

So far, no analysis method existed to deal with both scenarios. The calibration was done looking at the pulse height of the signal, while in the normal data acquisition run the integral of the whole signal was taken. While both methods work reasonably well in their domain, it was not possible to compare these methods over the full dynamic range of the veto system.

A method that allows to deal with small as well as large signals that are even overlapping is presented in the following section. This method is based on the deconvolution of a standard pulse. It automatically performs a normalisation of the signal in units of the standard pulse. If the standard pulse was composed of single photon pulses, the deconvolution method returns the number of photo electrons.

5.1 DECONVOLUTION

The signal recorded by the detector's data acquisition system is composed of two components:

1. A delta-like pulse corresponding to the detection of a photo electron at a certain time, described by $p(t)$
2. The electronic response of the detector including the dispersion in time and secondary charges produced, described by $r(t)$.

The convolution of these two functions returns the observed signal function $s(t)$ and is described by

$$s(t) = (p * r)(t) = \int_{-\infty}^{\infty} p(\tau)r(t - \tau)d\tau. \quad (5.1)$$

Lower case letters are used for quantities in the time domain. They can always be Fourier transformed into frequency space where these quantities are represented by capital letters

²With a mean of $\mu = 0.2$ the Poisson probability to observe two photons is 1.6 % and practically vanishes for even higher numbers of photons.

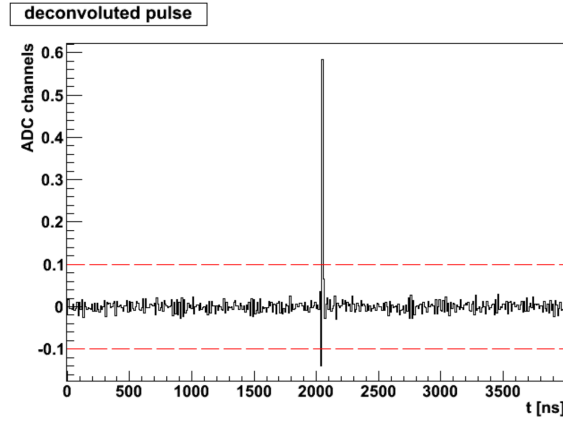


Figure 5.3: Deconvoluted pulse and thresholds above (and below) which the photo electrons are counted.

and depend from the frequency ω :

$$S(\omega) = \mathfrak{F}(s(t)) = \int_{-\infty}^{\infty} s(t)e^{-2\pi i\omega t} dt \quad (5.2)$$

The above convolution equation (5.1) can be written equivalently in frequency space:

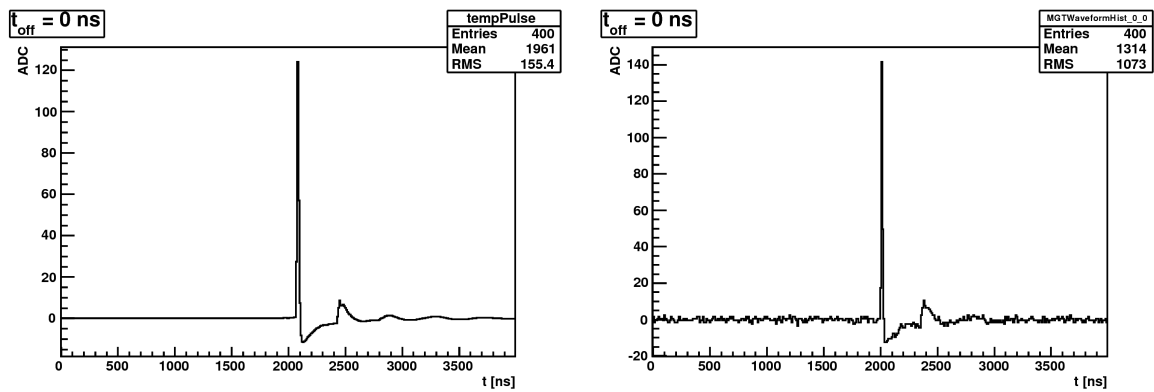
$$S(\omega) = P(\omega) \cdot R(\omega) \quad (5.3)$$

It has some obvious advantages to do the calculation of the convolution and particularly of the deconvolution in frequency space. This convolution of two functions to get one resulting signal function is depicted in Figure 5.2.

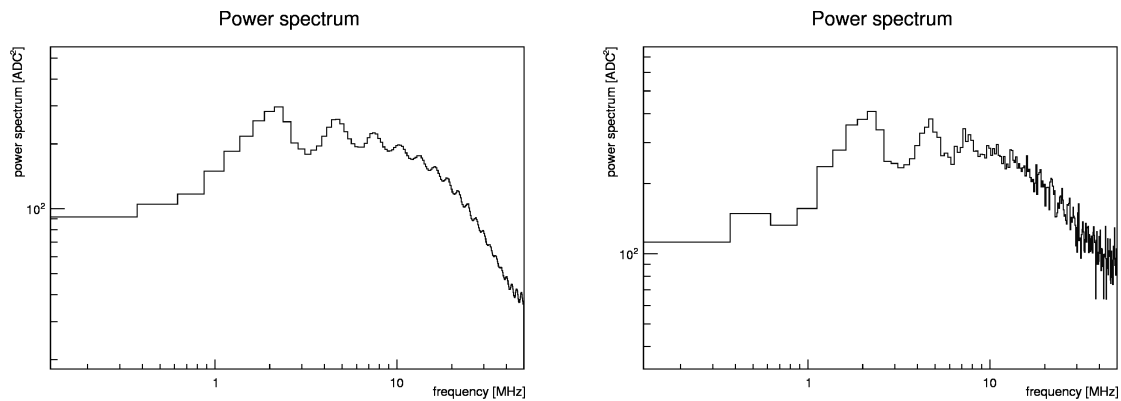
A typical detector response function to one photo electron $r(t)$ is defined by taking the mean of several thousand 1-PE calibration signals. The underlying pulse function $P(\omega)$, whose time domain representation $p(t)$ is basically a time series with delta functions at the times where a 1PE was detected, can be calculated from the measured signal $S(\omega)$ and the detector response function $R(\omega)$:

$$P(\omega) = \frac{S(\omega)}{R(\omega)} \quad (5.4)$$

This has to be converted back in the time domain and then represents the detected photon electrons in units of the standard 1 PE detector response. The original position within the time series is maintained, the height is measured in units of 1PE, which means that a signal with twice the pulse height of the average 1PE peak results in a value of 2 PE after the deconvolution. The pulse heights are still subject to statistical fluctuations which are inherent to the PMT technology. By deconvolving the response function, the signal function has become a lot cleaner and is easier to analyse. The total number of photo electrons contained in the signal can basically be summed up; to be less sensible to noise it is reasonable to define a threshold value for the values to add. In this work a threshold of 0.05



(a) A template pulse (left) and a single PE pulse (right) in time domain.



(b) Fourier power spectrum of a template pulse (left) and a single PE pulse (right) in frequency domain.

Figure 5.4: The Fourier transforms and original signals of a template pulse (first column) and the actual signal (second column). The template pulse is smoother (in time and frequency domain) due to it being the average of thousands of pulses. The oscillation in the Fourier signal is due to the post-pulse oscillation of the 1PE peak.

PE has been used. When also considering negative values, the fact that measured pulses do not perfectly match the template pulse can be considered to achieve even better results.

In Figure 5.4 the Fourier transforms of template and measured pulse are shown along the original signal. After the deconvolution, which is done in Fourier space, the deconvolved signal is much cleaner as can be seen in Figure 5.5.

5.2 COMPARISON TO OLDER METHODS

The deconvolution method is checked against two already existing methods. While the two old methods only work in their respective domain, which is low light intensity in calibration mode for the pulse height method and higher light intensity in physical mode for the integral mode, the deconvolution method (PE_FFT) works in both realms. To measure how well the

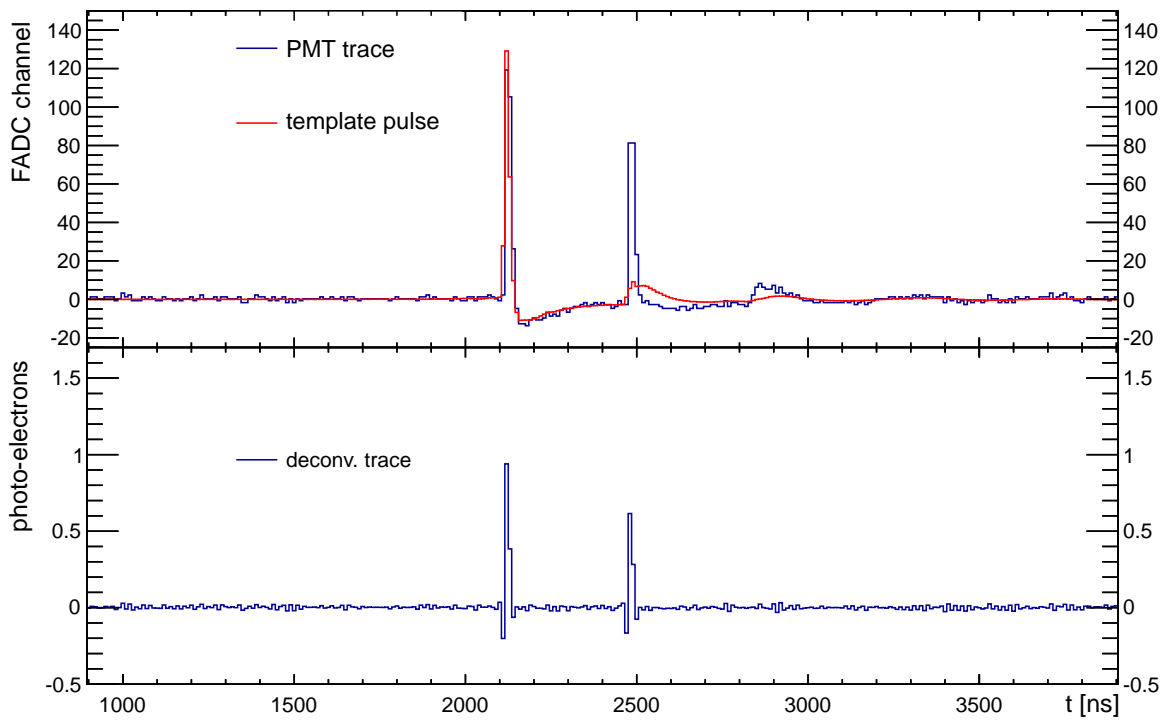
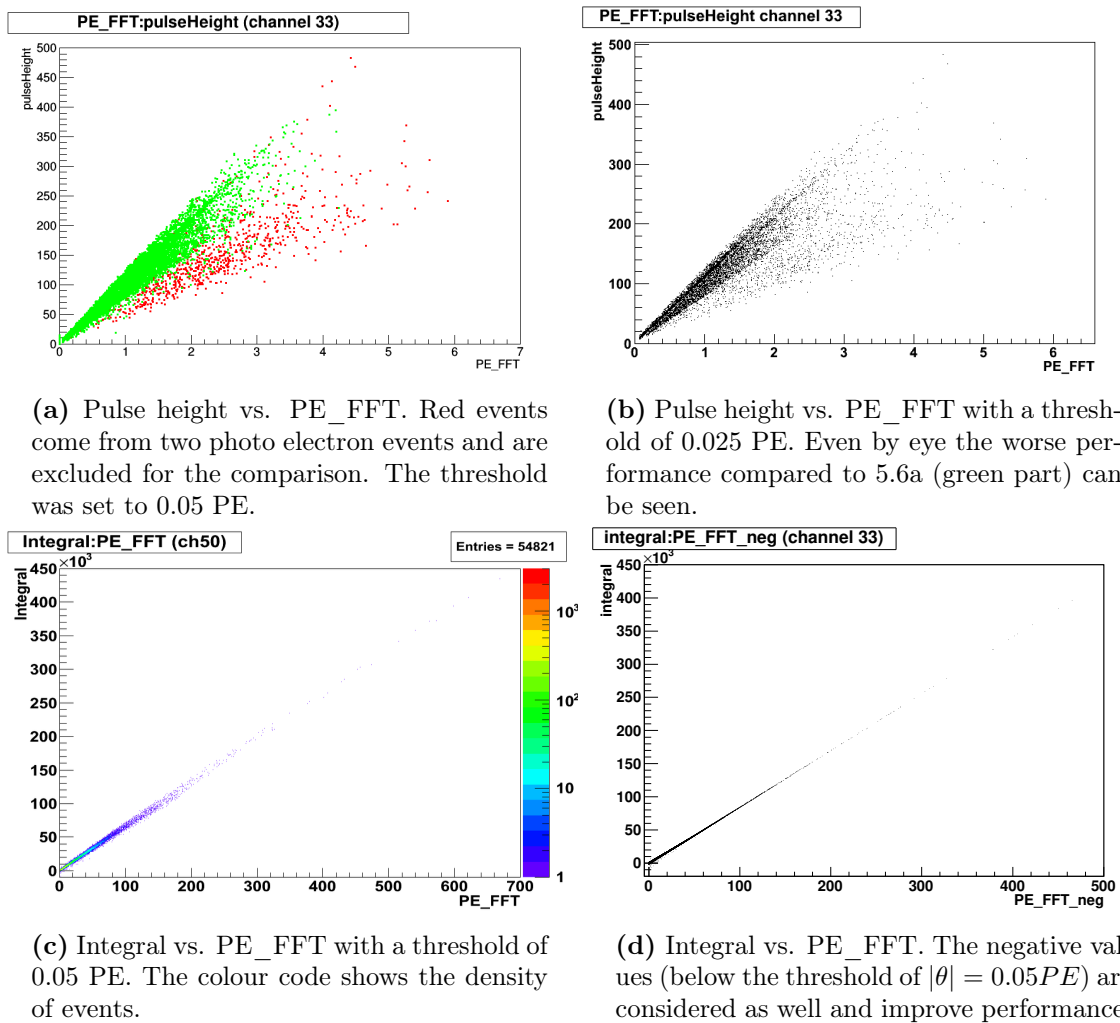


Figure 5.5: Two measured pulses together with the template pulse (in red) in the upper part of the figure and the deconvolved pulses after the transformation in the lower part of the figure. The template pulse is only drawn for the first pulse. The second pulse sitting in the ringing part of the first pulse is no issue for the deconvolution method. The deconvolution method yields the number of photo electrons, as it is normalized in units of 1PE pulses, and the timing of each interaction.



(a) Pulse height vs. PE_FFT. Red events come from two photo electron events and are excluded for the comparison. The threshold was set to 0.05 PE.

(b) Pulse height vs. PE_FFT with a threshold of 0.025 PE. Even by eye the worse performance compared to 5.6a (green part) can be seen.

(c) Integral vs. PE_FFT with a threshold of 0.05 PE. The colour code shows the density of events.

(d) Integral vs. PE_FFT. The negative values (below the threshold of $|\theta| = 0.05PE$) are considered as well and improve performance.

Figure 5.6: Comparing pulse height/integral method with the deconvolved template pulse method (PE_FFT). While pulse height/integral only work in their specific domain, the deconvolution works in all intensity ranges.

pulse height			integral		
threshold [PE]	PE_FFT	PE_FFT_neg	threshold [PE]	PE_FFT	PE_FFT_neg
0.5	0.9724	0.9843	0.5	0.9867	0.9891
0.2	0.9895	0.9990	0.2	0.9919	0.9922
0.1	0.9954	0.9985	0.1	0.9964	0.9958
0.05	0.9991	0.9993	0.05	0.9993	0.9997
0.025	0.9883	0.9904	0.025	0.9952	0.9943

Table 5.1: Correlation coefficient for different threshold values for the two light realms and their corresponding methods compared to the deconvolution method.

PE_FFT method works, the Pearson correlation coefficient

$$r = \frac{\sum_{i=1}^n (x_i - \bar{x})(y_i - \bar{y})}{\sigma_x \sigma_y} = \frac{\sum_{i=1}^n (x_i - \bar{x})(y_i - \bar{y})}{\sqrt{\sum_{i=1}^n (x_i - \bar{x})^2} \sqrt{\sum_{i=1}^n (y_i - \bar{y})^2}} \quad (5.5)$$

is used. For a measurement each event's pulse height (e.g. integral) is correlated with the corresponding value from the deconvolution method. This is done for each channel and the total correlation is taken as the average. The best correlation in both domains is achieved for a threshold of 0.05 PE, the method proves to be suitable in both domains.

A method that can be used in low and high light intensity domains to easily determine the number of measured photo electrons has been developed and checked. The measured waveform is automatically calibrated in units of single photo electrons with this deconvolution method.

6

Simulation and feasibility of the PET experiment

It's not an experiment if you know it's going to work.

Jeff Bezos

6.1 GENERAL IDEA

As mentioned in previous chapters, the pulse shape discrimination technique to reduce the background index is crucial for GERDA and other germanium-based $0\nu\beta\beta$ experiments. The method described in chapter 3.4, the A/E method, works well, and the performance of the pulse shape discrimination method is usually tested by irradiating a detector with a ^{228}Th -source. The ^{228}Th decay chain includes isotopes that produce gammas at 1620 keV (full-energy peak (FEP) of Bi-212) and 1592 keV (double-escape peak (DEP) of ^{208}Tl). The Bi-212 FEP is used as a multi-site-event prototype, while the DEP of ^{208}Tl is used as a typical single-site event. The shapes of the resulting waveforms vary depending on the position of the deposition in the crystal, but also on many other parameters like doping densities, their distribution, and even crystal axis play a role, so that the process itself is not well understood. The ^{228}Th -method cannot give event by event information. Only histograms of energy and shape parameters can be evaluated in dependence of the source type and position of the source. Moreover it is not possible to get spacial information out of this kind of measurement. Potentially, this biases the analysis results because irradiating the detector from the outside leads to a different distribution of DEP events than if they come from $0\nu\beta\beta$ and are uniformly distributed in the detector. Therefore, a method that allows to measure both the waveform and the position of its origin is desirable and is presented in the following

chapters. The combination of a medical PET detector with a germanium detector allows to reconstruct the initial point of interaction of DEP events and its corresponding waveform on an event-by-event basis. This chapter describes the basic concept of the setup and the simulations made to ascertain the feasibility of the experiment. The geometry of the lead collimator needed for the experiment is evaluated, and an estimate for the rate of coincident PET-germanium events is provided. These simulations show the feasibility of this experiment. Chapter 7 then describes the setup and experimental preparations. Results, issues with the realization of the experiment, narrowing-down error sources and possible solutions are described in chapter 8.

The basic idea of this experiment is to combine a germanium detector with the position-sensing capabilities of a PET scanner like it is used for medical applications. To produce an image a PET scanner detects many pairs of gammas, that are emitted back to back in β^+ -decays. The decaying isotope is usually applied intravenously, and depending on the isotope, is enriched in either the thyroid or tumour tissue. The image is reconstructed by evaluating the statistical distribution of hits in the detector cells in the PET tube. Of course, it is not possible to apply a radioactive source, especially not a liquid one, to the germanium detector. Another issue is that the image reconstruction is only a statistical process, while for the evaluation of the pulse shape discrimination efficiency the interaction point of each event should be reconstructed. The position along the line of flight of the two gammas can not be reconstructed. The time of flight for gammas on this length scale is way too short. It has only been tried recently to use the timing information to improve the reconstruction algorithms [55], but the very short flight times pose hard challenges to the electronics used and yield only slight improvements in resolution.

The solution to this dilemma is shining a collimated source from the outside on the germanium detector. The source has to be a high-energetic γ -source, in order to induce pair production in the detector. The probability for pair production increases with energy, as shown in Figure 3.1. The produced positron annihilates quickly with the emission of two 511 keV gammas. The line connecting the detector cells of the PET where the gammas were detected intersects the collimation axis and marks the location of the first gamma interaction where the pair production took place.

The schematic setup can be seen in Figure 6.1 with the radioactive source illuminating from the left through the collimation lead brick and in Figure 6.2, where the setup is turned and the source is located at the top. The “green” gamma passes through the collimator, creating a $e^+ - e^-$ pair, the positron annihilates which creates a 511 keV gamma pair that is detected in the PET tube surrounding the Ge-detector. So by moving the source and collimator relative to the detector and irradiating different areas of the detector, different x-y positions can be probed. For any x-y setup, the PET scanner provides the z-information, so the whole detector can be probed. At the same time, the germanium detector records the

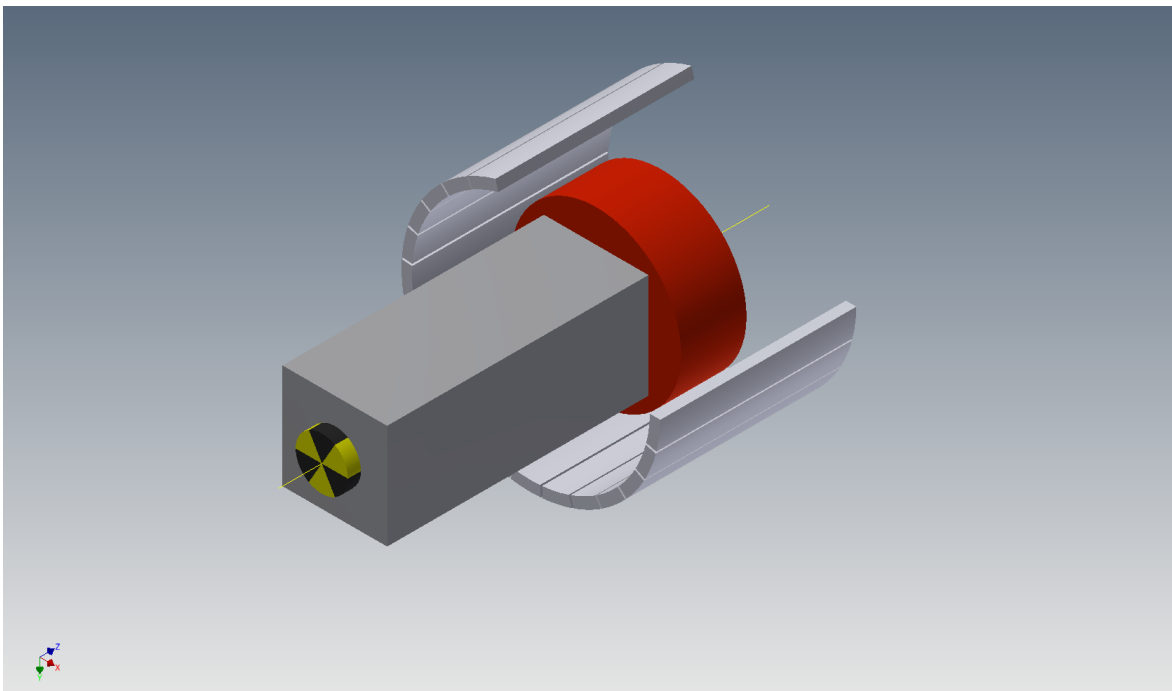


Figure 6.1: Schematic view of the setup of the germanium detector positioned in the PET tube, with lead collimator and radioactive source. The lead collimator contains a small hole to let through focused gamma rays.

waveform produced by the stopped electron-positron pair. The mean free path of electron and positrons is typically < 1 mm and can be considered point-like for the scope of this experiment. The wanted events have to meet two conditions at the same time:

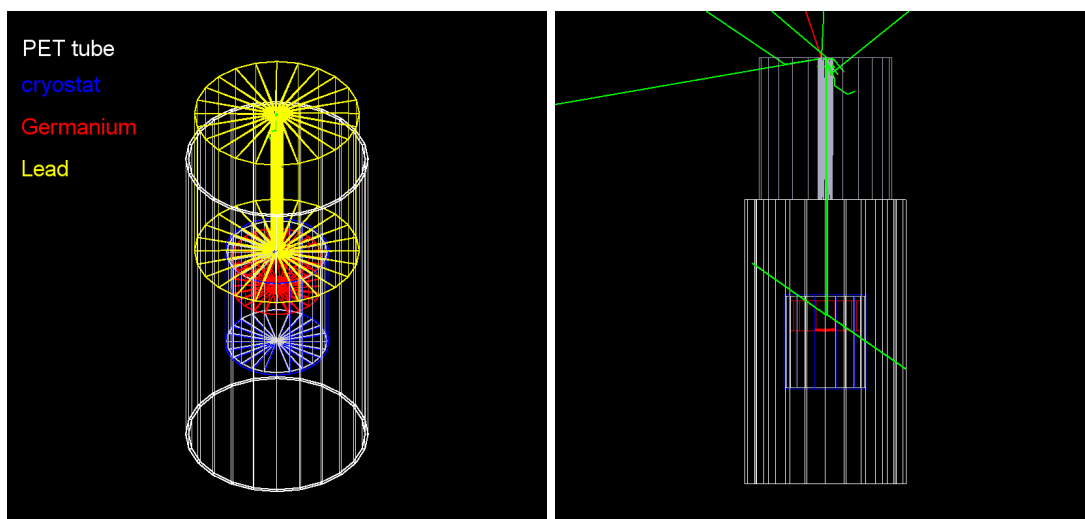
- energy around DEP energy in germanium detector
- two-fold coincidence in PET detector around 511 keV

With this setup, the waveforms of single-site-events can be measured in dependence of the location of their point of creation. A waveform library of typical pulses at a certain position can be created for a detector.

6.2 *Geant4* SIMULATIONS

Simulations in *Geant4* were carried out to estimate the size needed for the lead collimator. Also the expected rates were estimated to determine the necessary strength of the source and check the experiment for its general feasibility. These simulations were carried out partially by Julia Nagel for her Bachelor's thesis [46].

The geometries of the setup were implemented in the simulation. For the calculations MaGe [18] was used, a framework based on *Geant4* [8] that is used by the MAJORANA and GERDA collaborations for the simulation of their germanium detectors. *Geant4* was used in version 4.9.4.2.



(a) Simulation setup including PET tube (white), germanium (red), lead collimator (yellow) and cryostat (blue). Source is positioned on top of the collimator.

(b) Simulation setup including particle traces. A double escape event is shown with two gammas (green) being created within the detector and absorbed in the PET. Some other events that do not even pass the collimator can be seen near the source. Source is again located on top of the collimator.

Figure 6.2: View of the *Geant4* simulation setup.

6.2.1 DIMENSIONS OF COLLIMATOR

The collimation of the high energy gammas is paramount for the success of the experiment. For this reason simulations were done for different parameters, different diameters of the hole, different collimator lengths and positions.

The main parameters to vary are the length of the collimator, the diameter of the collimation hole and the position of collimator, germanium detector, and PET tube relative to each other. The material and the shape of the hole are somehow given for obvious reasons, since lead gives the best shielding and round holes are just easier to manufacture.

The right balance between a sharply irradiated area and an acceptable count rate has to be found. Another boundary is the practicality to have a lead collimator produced with the desired dimensions and to get a radioactive source produced and approved that has the desired strength. The simulations were done by shooting $5 \cdot 10^8$ gamma rays with energies of 2614 keV at the setup. The gamma rays' initial directions were evenly distributed in all directions, with the restriction that only the half space facing the experimental setup was used for the simulation. Table 6.1 summarises the results of this simulation campaign, Figure 6.3 graphically depicts the survival function in the germanium detector, the percentage of hits not contained within a certain radius, in dependence of the radius.

The simulation campaign favours a collimator length of 20 cm. Lead that is less thick is not sufficient to provide a well enough shielding and an illuminated area that is focused

length	diameter	survival function at radius						number of events
		0.25 cm [%]	0.50 cm [%]	0.75 cm [%]	1.00 cm [%]	1.25 cm [%]	1.50 cm [%]	
20 cm	0.75 mm	78.68	31.62	16.18	11.03	7.35	5.88	1,230
20 cm	1.0 mm	82.69	37.54	7.91	4.77	3.35	2.35	15,472
20 cm	1.5 mm	86.75	45.70	12.58	8.61	6.62	5.30	19,787
20 cm	2.0 mm	92.76	70.00	30.00	7.24	1.72	1.03	23,222
10 cm	0.75 mm	87.91	56.21	13.73	5.56	4.25	2.94	44,934
10 cm	1.0 mm	92.88	76.15	51.15	26.92	14.04	10.00	71,597
10 cm	1.5 mm	96.15	80.42	57.69	28.67	11.19	4.55	90,431
10 cm	2.0 mm	95.17	81.56	65.31	42.37	15.92	7.03	110,832
5 cm	0.75 mm	96.24	85.57	69.10	50.11	34.72	25.56	169,483
5 cm	1.0 mm	99.87	99.31	95.58	90.55	83.82	75.00	235,342
5 cm	1.5 mm	98.68	94.75	88.79	81.15	70.22	57.10	269,400
5 cm	2.0 mm	96.56	90.07	80.83	69.71	50.74	29.11	301,521

Table 6.1: Results for different simulation parameters. The survival function gives the percentage of hits not contained within the given radius.

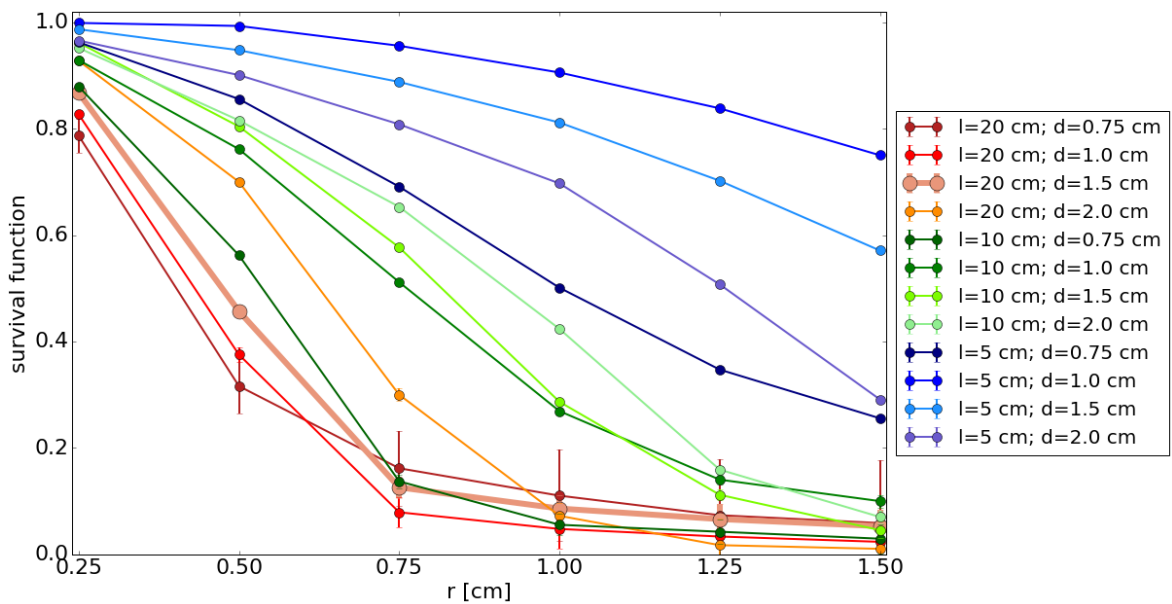
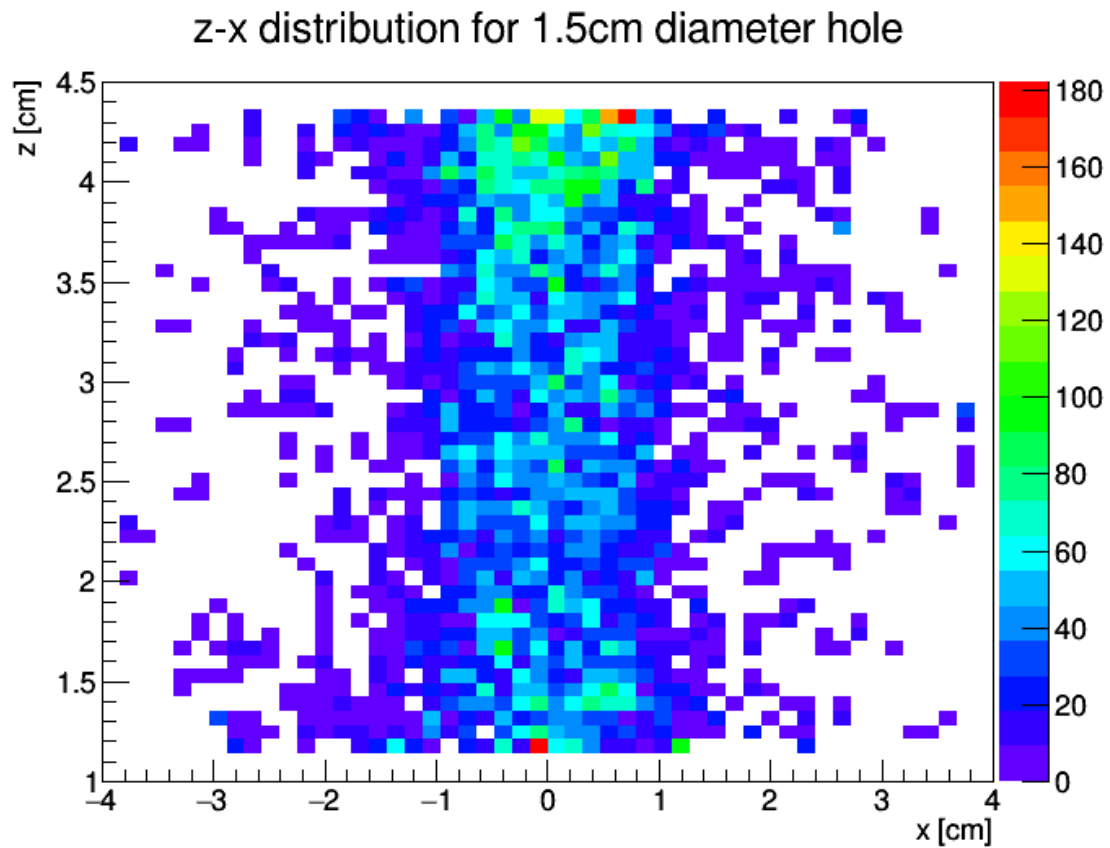
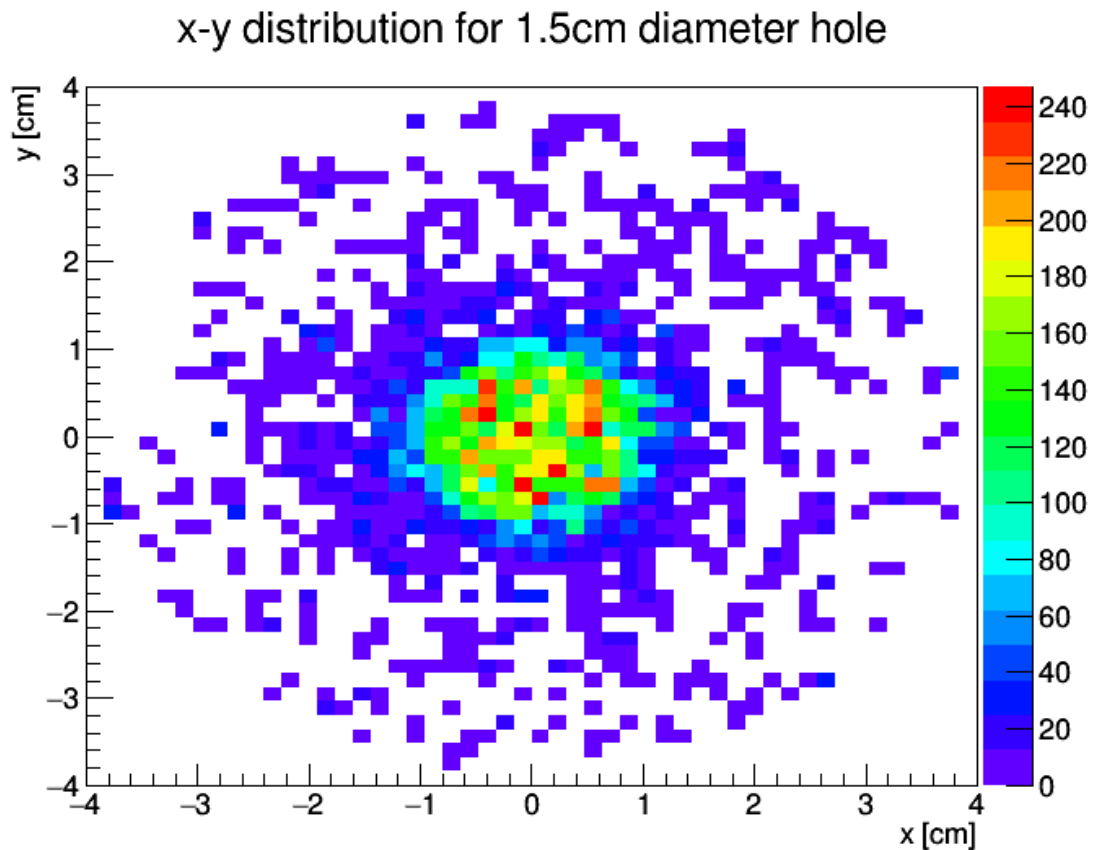


Figure 6.3: Survival functions for DEP events in dependence of the radius for different simulation parameters. Statistical error bars are included for all curves, yet only visible for the lines with the poorest statistics. A steeply falling curve is desired as this limits the illuminated region, while still reasonable numbers of gammas should be let through.



(a) Projection of simulated hits in z-x direction.



(b) Projection of simulated hits in the x-y plane.

Figure 6.4: Distribution of hits in the detector for a collimator with length $l=15$ cm and diameter $d=15$ mm. The source was positioned above the detector.

well enough. The collimation hole should either have a diameter of 10 mm or 15 mm. 7.5 mm giving the sharper focus but not allowing enough particles to reach the detector. This can be seen in Figure 6.3, where the curve for $l=20$ cm and $d=7.5$ mm has the largest error bars due to limited statistics, while the error bars for most other curves are barely visible. Since a 15 mm collimation diameter still gives a good enough focusing and better statistics, it was chosen use this diameter. An additional external constraint for that choice was that the department's workshop could only produce holes with this diameter at the required length. The distance between germanium and lead was varied also, but apart from a larger distance leading to a decrease in counts, does not seem to matter that much concerning the containment of the energy deposited. Therefore it was chosen to bring the collimator as close to the detector as possible. The spatial distribution of DEP events within the germanium detector can be seen in Figure 6.4. The parameters for the lead collimator yielding the best compromise between irradiated volume and high enough statistics were found to be:

parameter	best value
diameter	15 mm
length	20 cm
distance Pb-Ge	touching

Table 6.2: Best parameters for the dimensioning of the collimator as found by simulation.

While it was initially planned to use ^{228}Th as a source, it was later decided to use a ^{56}Co source due to activity and background considerations. A ^{56}Co source with an activity of 5 MBq was accessible, while thorium sources only existed at the institute with an activity of a few hundred kBq. The big advantage of ^{56}Co though is, that it is not naturally occurring and so the gammas at the wanted energies definitely originate from the source. For Th-228 this is not given, since thorium contaminations (to a small extent) are practically everywhere and some gammas would originate in the material surrounding the detector, invalidating the hypothesis that the initial gamma came in along the collimation axis. The previous simulations were done with gammas at the thorium¹ energies. After the switch to cobalt with its slightly higher energy gammas, the simulation was repeated with the best parameters from the thorium simulation to check if more lead for the collimation would be necessary. The survival functions were practically identical within the margin of errors, so the setup could be kept.

¹At the ^{208}Tl energies to be precise. But since thorium is the initial isotope and thallium occurs in its decay chain, thorium will often be used to refer to the source/gamma rays

6.2.2 EXPECTED RATES

As discussed in the section above, the dimensions of the collimator and the source have a large effect on the collimation and the expected rate. The number of gammas simulated in relation to the gammas detected in the detector with the correct energy helps to estimate the needed activity of the source. The activity has to be matched to realistic run times, so that enough events are recorded in a typical measurement cycle of ~ 24 h. The simulation has to be expanded to also take into effect, that the two escaping 511 keV gammas have to both reach the PET ring. When this is done, for the best parameters from above, the following numbers are found:

Some inaccuracies occur due to the fact, that the exact sensitivity of the PET detectors is not

total simulated	$5 \cdot 10^8$
events in detector	564573
events DEP	19787
events in PET	
350 keV < E < 750 keV	573
particleType = gamma	

Table 6.3: Detected events with different criteria from simulation

known and its modelling is beyond the scope of this estimation. Many unknown parameters would have to be included in such a simulation like the response of the photomultipliers that read out the LSO crystals, the exact geometries and the location and size of the metal holders and shields. The simulation that was performed includes the energy deposition in the correct material (LSO), the range chosen represents the not so good energy resolution of the PET detector and is based on the energy thresholds chosen in the experiment later on. Efficiencies of the PET are estimated below. Taking into account that in the simulation the gammas are produced from a point-like source and are distributed in all directions in the half space to save resources, a factor of two has to be introduced.

In order to calculate the number of PET-detectable interactions per second, a 5 MBq ^{56}Co source is assumed.

$$\frac{573}{2 \cdot 5 \cdot 10^8} 5 \text{ MBq} \cdot 0.25 = 0.72 \frac{1}{\text{s}} \quad (6.1)$$

The factor 0.25 is due to the probability of ^{56}Co to produce one of the desired lines (7.93 % for 3253 keV, and for the 2598 keV line it is 17.28 %). Again, this does not take into account the sensitivity of the PET system, but the rate in the order of ~ 1 s sounds interesting enough.

In order to further estimate the sensitivity of the PET, a few considerations are made. The attenuation coefficient for LSO is $\mu = 0.87 \text{ cm}^{-1}$ [52]. With a thickness of the LSO crystals in the INVEON of 10 mm this amounts to 87% efficiency. On the other hand, the probability of total absorption on the first interaction for a 511 keV gamma is 0.34 for LSO [41]. This is a

class of events	lower bound	upper bound
events that produce a e^-e^+ pair and whose annihilation gammas deposit their energy in PET	62208	
events including the estimated PET efficiency	6394	41818
events in 1cm slice furthest away from surface	1598	10454

Table 6.4: Overview of the expected number of events from simulation in a 24 h measurement with a 5 MBq source. The different stages of efficiency considerations are included, as well as the upper and lower bound for the efficiency.

lower bound, since compton-scattered events can still contribute if they deposit all or most of their energy in the crystal. The efficiency from the attenuation coefficient is an upper bound, since this only describes gamma particles that interact at least once and does not necessarily mean that enough energy is deposited in the crystal in order to be detected.

This brings up the next topic: the energy window in the PET detector, which is chosen from 350 to 750 keV. With an energy resolution of typically $\sim 20\%$ the integration over the gaussian yields that 94 % of 511 keV events are contained within the window from 350 to 750 keV.

Combining the above efficiencies, a correction factor for the PET efficiency of

	absorption eff. \times energy window eff.	total eff.
lower bound	$0.34 \cdot 0.94$	0.32
upper bound	$0.87 \cdot 0.94$	0.82

has to be considered.

These efficiencies have to be squared because they apply to both gammas of the coincidence. The rate of interesting events is then reduced to

$$\begin{aligned}
 \text{lower bound:} & \quad (0.32)^2 \cdot 0.72 \frac{1}{\text{s}} = 0.074 \frac{1}{\text{s}} \\
 \text{upper bound:} & \quad (0.82)^2 \cdot 0.72 \frac{1}{\text{s}} = 0.484 \frac{1}{\text{s}}.
 \end{aligned} \tag{6.2}$$

For a measurement period of 24 hours, this amounts to 6394 - 41818 events depending on the actual PET efficiency. It has to be noted that the efficiency of the PMTs that read out the LSO crystals is not considered at all. Another thing to check is if the number of events at the back of the detector is sufficient. The distribution of events in germanium along the collimation axis, the z-axis, is shown in Figure 6.5, with the source irradiating from the left. The first centimeter from the surface contains roughly 50% more events as the middle or last centimeter. This reduces the expected rate in the lower section of the detector by another factor of ~ 4 .

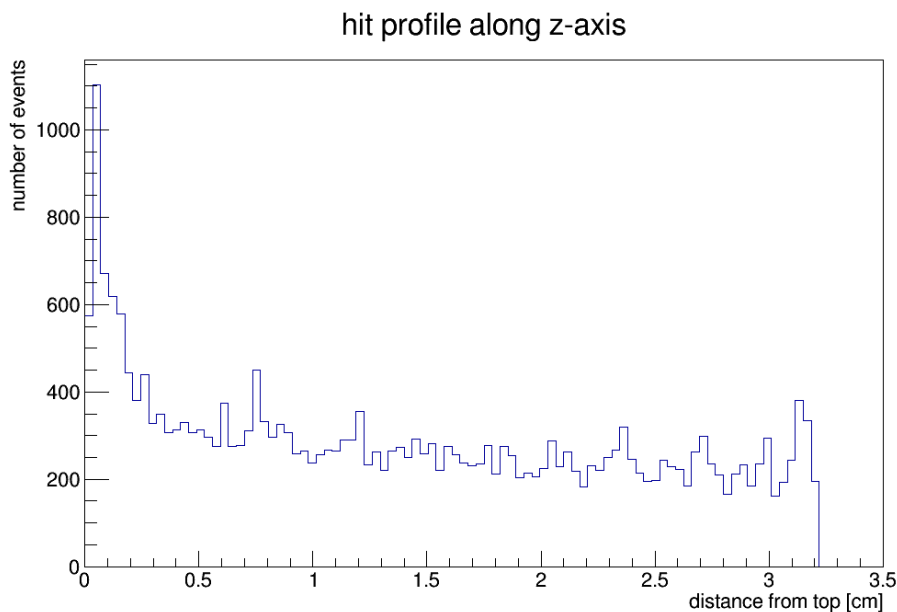


Figure 6.5: The distribution of events along the collimation axis measured in centimeters from the surface.

6.2.3 POSITION RECONSTRUCTION

The reconstruction of the interaction point is the crucial point of the proposed experiment. To achieve a good reconstruction the dimensions of the lead collimator have been optimized as described in the previous section in order to yield a reasonably limited irradiated area and high enough statistics. This section demonstrates how the interaction point is calculated and presents the position sensitivity from experiment and from simulation. A point source has been measured, i.e. simulated and the distribution of the reconstructed positions is displayed.

MATHEMATICAL PROCEDURE

The lead collimator provides an axis along which all candidate DEP events should occur. For each event in which a 511 keV double coincidence condition is met, the PET scanner returns a pairs of $(ringNumber1, detectorNumber1)$ and $(ringNumber2, detectorNumber2)$ tuples. These coordinate pairs can easily be transformed into cylindrical coordinates, or into cartesian, as needed. The line connecting these two points on the cylinder surface of the PET is checked for intersections with the imagined extension of the collimator axis. Typically, the two lines will have no exact intersecting point and are therefore skew. The point of interaction will be defined as the point located exactly in the middle of the line of minimal distance between the two original lines. If this minimal distance is small enough, the lines are considered to be intersecting, from a real world point of view.

The coordinate system is chosen so that the z-axis serves as the symmetry axis of the rotational symmetry of the PET and germanium detectors. The transformation from ring R and

detector number D to cylindrical coordinates is then described by the following formulas:

$$\rho = r_{PET} \quad (6.3)$$

$$z = \frac{R}{R_{MAX}} l_{PET} \quad (6.4)$$

$$\varphi = D \frac{360^\circ}{D_{MAX}} \quad (6.5)$$

For the Inveon PET the total number of rings is $R_{MAX} = 80$ and the total numbers of detectors per ring is $D_{MAX} = 80$.

The two pairs of ring-detector coordinates there give the two points \vec{a} and \vec{b} in cartesian coordinates:

$$\vec{a} = \begin{pmatrix} \rho \cos(\varphi_a) \\ \rho \sin(\varphi_a) \\ z_a \end{pmatrix} \quad \vec{b} = \begin{pmatrix} \rho \cos(\varphi_b) \\ \rho \sin(\varphi_b) \\ z_b \end{pmatrix} \quad (6.6)$$

The line connecting the points is given by

$$l : \vec{x} = \vec{a} + t\vec{d} \quad \text{where} \quad \vec{d} = \vec{b} - \vec{a} \quad (6.7)$$

The other line is given by the collimator axis

$$c : \vec{x} = \vec{c}_0 + s\vec{c}_1 = s \begin{pmatrix} 0 \\ 0 \\ 1 \end{pmatrix} + \begin{pmatrix} x_{offset} \\ y_{offset} \\ 0 \end{pmatrix} \quad (6.8)$$

plus an optional offset in x and y, in case the source is moved relative to the germanium detector to probe it in its outer regions.

The normal vector \vec{n} is perpendicular to both lines, l and c

$$\vec{n} = \frac{\vec{d} \times \vec{c}_1}{|\vec{d} \times \vec{c}_1|} \quad (6.9)$$

and Δx gives the distance between the two skew lines:

$$\Delta x = (\vec{a} - \vec{c}_0) \cdot \vec{n} \quad (6.10)$$

In order to calculate the two base points of the minimal distance line m , it is recalled that this line has to be perpendicular to l as well as to c . Thus m has to be parallel to \vec{n} . The plane E that is spanned by \vec{c}_1 and \vec{n} contains \vec{c}_0 and can therefore be created by shifting of line c along \vec{n} . Line l intersects this plane in point \vec{p}_1 which is also the point closest to line c . To calculate \vec{p}_1 the plane E is transformed to the normal form using the normal vector $\vec{n}_1 = \vec{n} \times \vec{c}_1$

$$E : \vec{n}_1 \cdot [\vec{x} - \vec{c}_0] = 0 \quad (6.11)$$

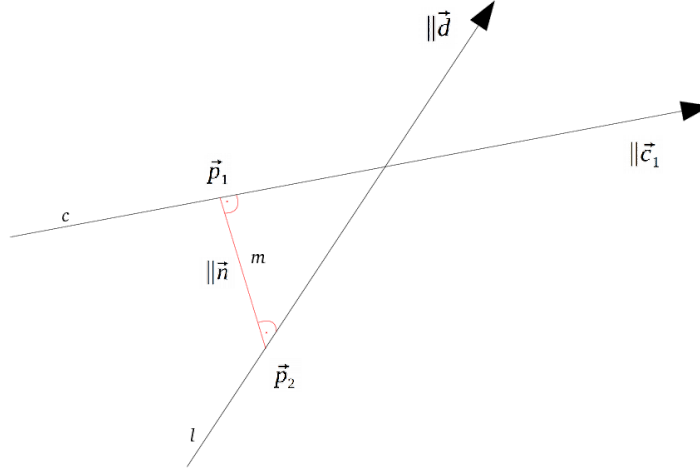


Figure 6.6: Sketch to demonstrate names and positions of lines and points in reconstruction procedure.

and equation 6.7 is inserted for \vec{x} and solved for parameter

$$u = \frac{(\vec{c}_0 - \vec{a}) \cdot \vec{n}_1}{\vec{d} \cdot \vec{n}_1} \quad (6.12)$$

which inserted in the line equation for l yields the intersection point \vec{p}_1 . Analogously, the calculation yields \vec{p}_2 when plane F spanned by \vec{n} and \vec{d} and supported by \vec{a} is intersected with c :

$$\vec{p}_1 = \vec{a} + \frac{(\vec{c}_0 - \vec{a}) \cdot \vec{n}_1}{\vec{d} \cdot \vec{n}_1} \vec{d} \quad (6.13)$$

$$\vec{p}_2 = \vec{c}_0 + \frac{(\vec{a} - \vec{c}_0) \cdot \vec{n}_2}{\vec{c}_1 \cdot \vec{n}_2} \vec{c}_1 \quad (6.14)$$

The interaction point is then assumed to be in the middle of the two base points along m :

$$\vec{S} = \vec{p}_1 + \frac{1}{2}(\vec{p}_2 - \vec{p}_1) \quad (6.15)$$

It has to be mentioned, though, that the reconstruction cannot be more accurate than the width of the projection of the cylinder.

A schematic view of the particles' reconstructed paths can be seen in Figure 6.7, with the original hits in the germanium in red and the hits in the PET represented by black dots.

POSITION SENSITIVITY FROM SIMULATION

The Geant4 simulation has the big advantage that the knowledge about the location of the interactions inside the detector is also known. The reconstruction algorithm i.e. the whole measurement setup can be tested by comparing the reconstructed interaction point to the

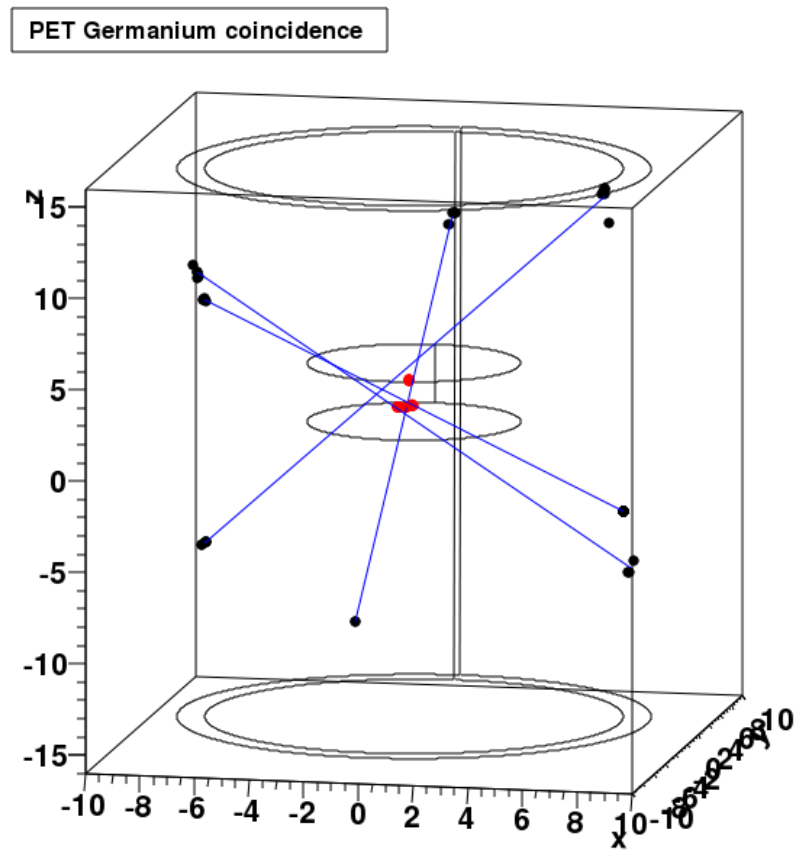
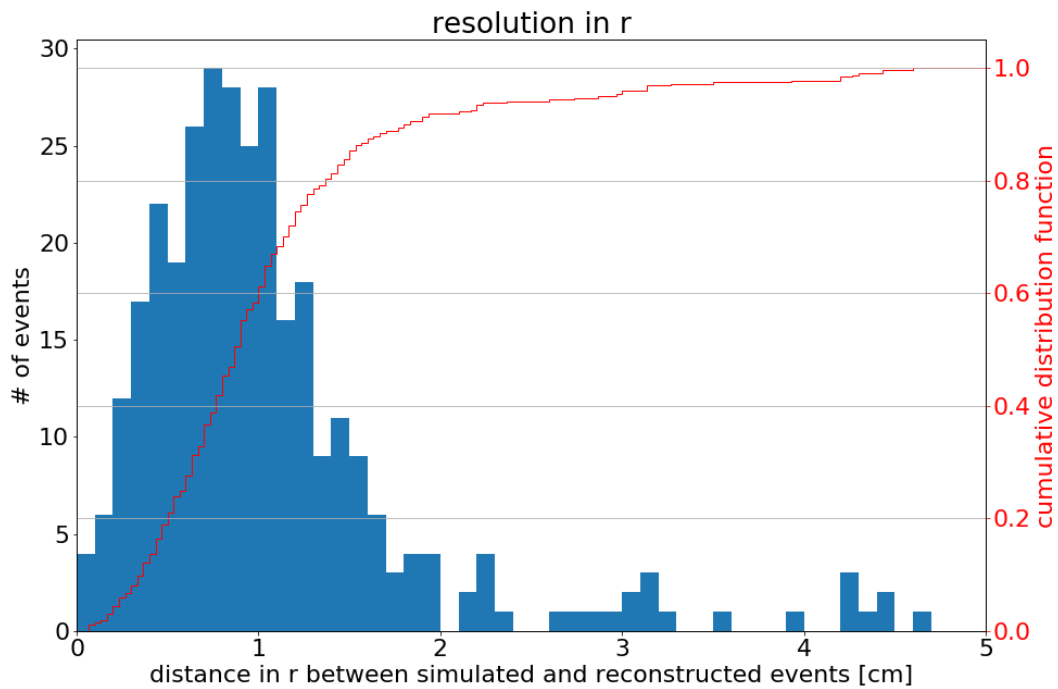
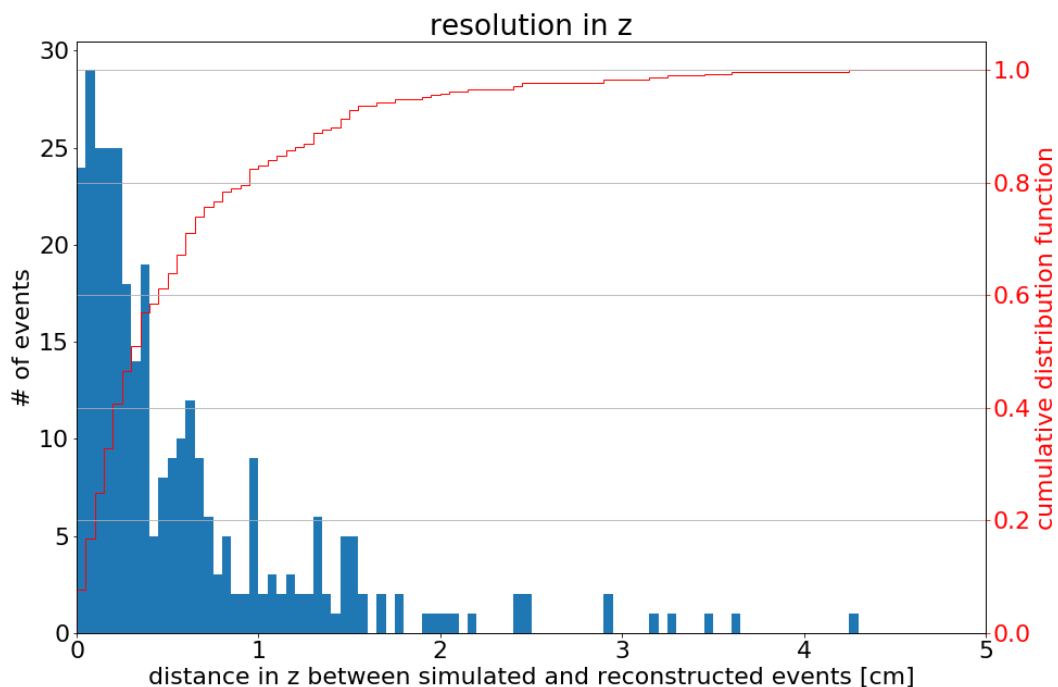


Figure 6.7: Simulated points of interaction in germanium (red) that create two gamma rays which are detected in the PET ring. Blue lines connect points in PET. The original gamma is coming from above. Simulation setup is rotated with respect to the real experimental setup.



(a) Resolution of the reconstructed algorithm in r direction.



(b) Resolution of the reconstructed algorithm in z direction.

Figure 6.8: Distance between the reconstructed interaction point and the simulated one. Resolution is separated for r (a) and z (b). The reconstruction was done by only using the hit pattern of affected detectors in the PET. The spatial information of hits within the PET was discarded, only the index numbers referencing the PET detector cell were used. Only events with a maximum distance between interaction points in germanium of less than 1 mm were used for this analysis.

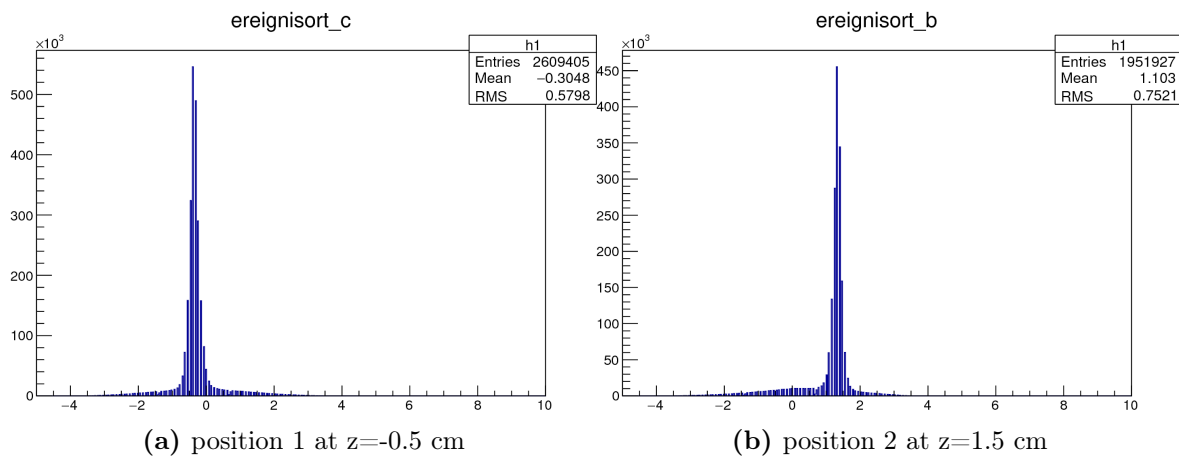


Figure 6.9: Reconstructed positions of the ^{22}Na source in the PET detector.

simulated one. As described above, the reconstruction algorithm has to assume a collimated beam of gammas and cannot be more exact than the diameter of the collimator; even less since collimation is not perfect. The simulation and consecutive analysis was done using the best parameters from above, in particular a borehole with a 1.5 cm diameter. For each event the simulation returns the coordinates of each interaction point, for the PET as well as for the germanium detector. Since the simulation does not group the energy depositions into a detector pattern already, these hits in the PET were first split up into clusters. The clusters were split so that the hits² stemming from one gamma would only return the coordinates of one weighted mean point. A new cluster was started when

$$\vec{d} = \vec{x}_i - \vec{x}_{i-1} > 1 \text{ cm},$$

the stepwidth from one interaction point to the next was greater than 1 cm. Only events with two clusters in the PET detector were considered, a single interaction point per cluster has been calculated based on the average. The locations of the clusters were then projected to the integer ring-detector scheme of the PET detector. Only events that also had an energy deposition in the germanium in the DEP region were considered. An average interaction point was also calculated for the germanium interaction. The reconstructed interaction point was then compared to the one obtained from simulation. The difference between them can be seen in Figure 6.8 and has its mode, the most likely value, at 1 cm. Using a collimator of \varnothing 1.5 cm results in an area of DEP interaction points with a diameter of $\varnothing < 2$ cm (see Figure 6.4a). Figure 6.8 also shows the cumulative distribution function i.e. the percentage of events reconstructed within a certain distance to the actual point of interaction. The result, that 90% of events are reconstructed within less than 1.7 cm, is quite encouraging. The manufacturer quotes a resolution of 1.4 mm FWHM, but this value does only apply for point-like sources and a different reconstruction algorithm and is not meant for event-by-event reconstruction.

²usually an electron that has several interactions before being stopped

POSITION SENSITIVITY FROM EXPERIMENT

A small experiment was set up to test the reconstruction algorithm described above and to measure the spacial resolution. A small glass vessel containing diluted ^{22}Na was introduced in the PET scanner and a few short runs were taken. The inside diameter of the vessel was 0.5 mm. ^{22}Na is a β^+ emitter and releases 2 gammas with 511 keV each and is therefore well suited to check the reconstruction algorithm. The source was positioned on two different positions along the central axis. The analysis was done without the knowledge of the position of the source. The two positions could be reconstructed at $z_1 = -0.5$ cm and $z_2 = 1.5$ cm within the margin of error of positioning the source in the detector by hand. The measured resolution was 29mm FWHM. That is not too great compared to the official resolution quoted by Siemens of 1.4 mm FWHM at the centre of the field of view, but the approaches are very different. One being a highly developed reconstruction algorithm, optimised for image reconstruction, while the other reconstructs location place of the interaction on a event-to-event basis.

6.3 SUMMARY

This chapter has described the basic idea of the experiment. An expected rate of relevant events was estimated; for a 5 MBq source and within a measurement time of 24 hours 1598 - 10454 events are expected in the 1 cm slice of the detector furthest away from the source, depending on the actual sensitivity of the PET. A few thousand events should be recorded and due to the coincidences between the detector systems and the uniqueness of the ^{56}Co gamma energies, these events should be virtually background-less. This proves the general feasibility of the experiment.

7

Setup of the PET experiment

Press DEL to enter SETUP

BIOS

The previous chapter described the general idea of the experiment: to determine the interaction point of a double escape gamma event in a germanium detector. To do this, a gamma source is collimated with a lead block and pointed on the germanium detector. The escaping gammas are detected in the PET tube surrounding the detector. The positional information of the interaction is determined by intersecting the line of collimation with the line connecting the two detector cells where the two 511 keV gammas were detected in the PET. The challenge is, as mentioned before, to temporally correlate the two detection systems. This chapter deals with the description of the experimental setup, the challenges when the two systems were hooked-up together and how it was solved by injecting a pulser pattern into both systems. In order to inject the synchronisation marker in the PET data an input port was used which was originally designed to mark those times when the animal was breathing. In this case this external input port was used for the synchronisation trigger sequence and for trigger signals from the germanium detector to establish the coincidences between the systems. The setup and the event classes will be explained in detail in the following chapters.

7.1 MEASUREMENT SETUP

The setup of the experiment is schematically sketched in Figure 7.3. The PET small animal scanner with its large bedding and processing unit is the biggest structure. The germanium detector with its liquid nitrogen supply is inserted in the PET tube. The lead collimator

along with the radioactive source are both attached from the other side of the tube.

The waveforms of the germanium detector were recorded using a Struck SIS3302 FADC with 100 MHz sampling frequency. The conversion of the signal standards (from TTL to NIM and the other way around) was done using rather old Ortec NIM-modules. The trigger pattern was generated by a Tektronix pulse generator. The PET system is described in more detail in section 7.3.

A synchronisation marker, or more precisely a trigger pattern consisting of three pulses, was sent every second from the pulse generator to the FADC, which passed it on to the PET system. This was necessary as the internal clocks of both DAQ systems were deviating over time. Whenever the germanium detector registered an event above its threshold, a coincidence marker was sent to the PET system, as well.

Both markers were recorded in the data with their respective timestamp. The set-up of the triggers and in which systems they are fed is pictured in Figure 7.1. This means there are three different classes of events:

PET event The conditions in the PET detector for a coincidence are met (two energy depositions with ~ 511 keV within the coincidence window) and the timestamp together with the indices of the involved detector cells are recorded in the PET DAQ system.

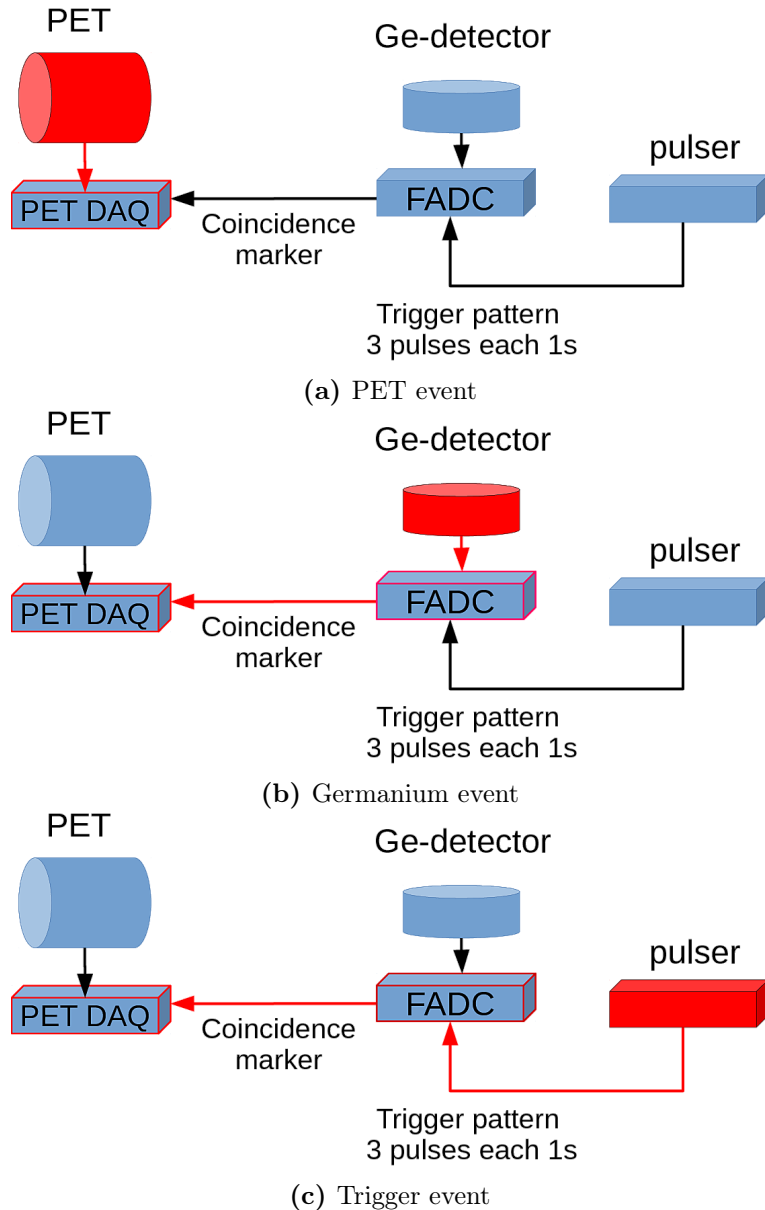


Figure 7.1: Schematic setup of the DAQ and trigger logic. The three different event types are displayed. A PET event is only registered in the PET DAQ (a), a germanium event is recorded in the Ge-DAQ, additionally a logical signal is sent to the PET (b). The pulser sends a synchronisation sequence every second to the germanium system (c), which in turn sends a coincidence marker to the PET, therefore the pulser is registered in both DAQ systems and can be used to synchronise the times.

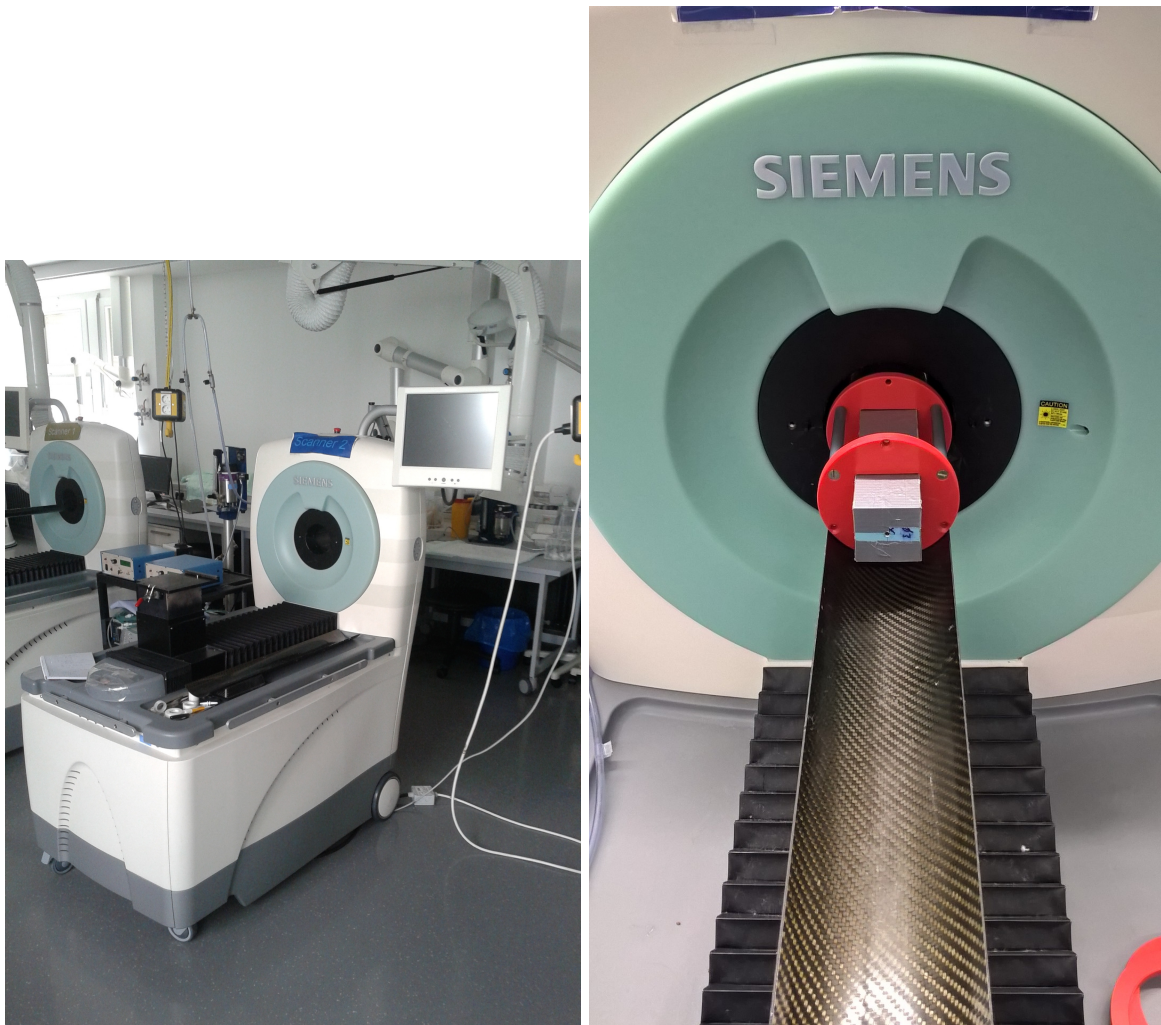


Figure 7.2: Picture of the lab setup.

germanium event If the signal pulse at the electrode of the germanium detector exceeds a threshold value, the waveform is recorded by the FADC and a digital pulse is sent to the PET DAQ where the timestamp of it is recorded as well.

pulser event In order to be able to compare timestamps of the two DAQ system in case of asynchronous internal clocks, a synchronisation pulse was sent from the pulse generator to the FADC, which in turn sent a digital signal to the PET DAQ. To make this pulse signal stand out against the other events recorded via the trigger port, a pulser pattern of three pulses was created. These trigger events are used to correct the timestamps and make it possible to match events across DAQ systems. The trigger system is explained in section 7.2 and the pulser pattern can be seen in Fig. 7.4.

An impression of the experimental setup as well of the lab where the experiment was built up can be seen in Figure 7.2. The fact that the lab is being used for animal experiments leads to the necessity of wearing full body protective equipment to protect the animals against germs and other extra diseases.

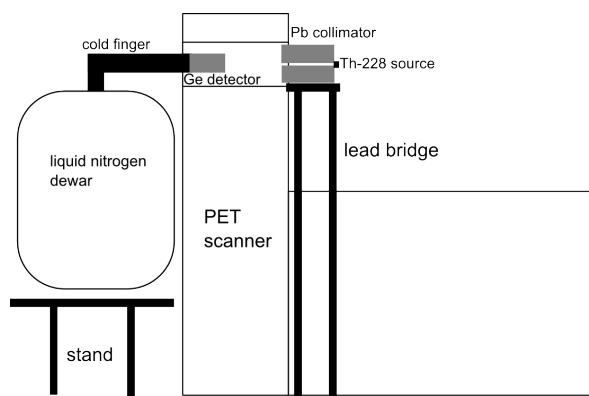


Figure 7.3: A sketch of the setup of the experiment. The arrangement of the germanium detector in the small animal PET, the lead collimator, and the radioactive source.

7.2 TRIGGERS AND TIMING PATTERN

Unfortunately the PET system, due to it being a commercial system, offers no possibility to get any triggers out of the system. The only possible interface to connect the two machines is an input port, supposed to be used as a veto trigger for the heart beat or breathing rhythm of the animal. Movements of the animal decrease the image quality, with this marker that is created by a breathing monitor¹ it is possible to add a veto marker and exclude those events following the marker from the data. With these events excluded, the picture is only reconstructed from events where the animal was at total rest and therefore the image gets sharper. However, for this experiment this input port is used for the coincidence signal coming from the germanium detector. No events are removed for this experiment and the marker is used to correlate events from PET and Ge-detector as well as monitor the time shift of the internal clocks.

It had to be checked how suitable this input port is in taking signals with higher frequency than it was originally designed for. So some small test runs were set up with a pulse generator hooked up to the input veto port. It was then looked at the number of veto events found in the output data file. Since there existed no extensive technical documentation, also the length, amplitude, and polarity of the pulse had to be determined. The results for pulse frequency and pulse duration are shown in Table 7.1, amplitude and polarity could be determined quickly enough. The results show that at a pulsing frequency of 10 kHz and a pulse duration of 50 μs all pulses are still recorded. Only for shorter and quicker pulses does the recording efficiency decrease. Assuming that the 10 μs after one pulse were absolute dead time, while in fact the efficiency is still a lot better than that, the ratio of pulses within this time interval at a random count rate of $\lambda \sim 100 \frac{1}{\text{s}}$ is

$$\frac{\int_0^{10\mu\text{s}} e^{-\lambda t} dt}{\int_0^{\infty} e^{-\lambda t} dt} \approx 9 \cdot 10^{-4} \quad (7.1)$$

¹or heart rate monitor, the same principle applies for the heart beats of the animal as for the breathing.

run number	frequency	pulse duration	events expected	events received
1	500 Hz	1 ms	15.000	14.987
2	1 kHz	50 μ s	30.000	30.008
3	5 kHz	5 μ s	150.000	150.017
4	10 kHz	50 μ s	300.000	299.997
5	10 kHz	25 μ s	300.000	299.538
6	50 kHz	10 μ s	1.500.000	984.802

Table 7.1: Results for input port checks. Several pulsing frequencies and pulse durations have been tried out. Only for very high and short pulses does the PET system lose events.

This means that, as an upper bound, no more than 1 in one-thousand pulses will be lost, in reality even less. The event rate of $100 \frac{1}{s}$ is defined by the FADC reading out the germanium detector, roughly 150 events per second is the maximum that can still be read out without introducing dead time for signal processing. For a trigger system that is only supposed to track the breathing or heart rate of a mouse, this maximum pulser frequency it can still handle seems rather good.

These tests proved that even for a strong source, the expected rate of events with energies in the DEP range that would create a trigger marker that is sent to the PET, would still be manageable by the PET system. To be able to check possible deviations in the running of the clocks of the two systems it was decided to additionally inject a synchronisation marker in the Ge and PET DAQ systems. The FADC provides two individual channels, one for the detector signals and one for the synchronisation signal from the pulse generator. So the different event types can be easily distinguished by looking at the right channel². But the PET systems only has one channel and the shape of the waveform is lost, making timing and germanium events undistinguishable. To deal with this, a distinct pattern of trigger pulses was injected into both systems every second. The timestamps of this pattern in both systems can be used to correct the clocks, make the timestamps compareable, and find coincidences via these timestamps. In theory, an event-by-event correspondence between the germanium and PET coincidence events could be produced directly without using the extra triggers, but in practice there are events missing in both data every once in a while, which makes it harder to establish a direct correlation. In order to reliably detect the trigger pattern, a pattern of three consecutive pulses was chosen with a pulse duration of 25 μ s and a period of 50 μ s per pulse, hence the whole pattern takes 150 μ s and it is shown in Figure 7.4. The granularity of the timing in the PET output data is 200 μ s. This means that the three triggers can have the same timestamp, or one of the triggers is ahead or behind one timing slot. This pattern can be easily found in the data. The PET reaches almost 100 % trigger recording efficiency; the germanium detector, or the FADC recording it, have a slightly lower efficiency, so that patterns missing one or more triggers occur every once in a while. Even totally missing patterns occur in the germanium data while they are still recorded in the PET data. This

²Also the pulse shape is very distinctive.



Figure 7.4: The pulser pattern, that is induced in the PET and the germanium DAQ. The pattern is used to find out and later correct a time shift in the two DAQ systems.

is due to the fact that the FADC does recognise the incoming trigger and also passes it on to the PET system in almost 100% of the time, but the recording system of the FADC can possibly be busy writing to disk, writing and clearing the buffer, so that no new events can be recorded. Using the trigger pattern a safer event-to-event correlation can be achieved.

7.3 THE INVEON PET SCANNER

The Inveon PET scanner is a medical/scientific instrument for small-animal imaging produced by Siemens Healthcare GmbH. It is used to research clinical imaging using mice and rats and investigating biological processes and diseases in these animals, i.e. cancer. Its detector array consists of 64 detector blocks (4 along the z-axis and 16 to cover the circumference of the PET tube) arranged in a cylindrical shape. Each detector module consists of a 20×20 array of LSO³ crystals of size $1.6 \times 1.6 \times 10$ mm. Each LSO block is optically coupled to an array consisting of four photomultiplier tubes (Hamamatsu R8900 C12 PSPMT) via a light guide. The crystals of the detector block are separated by saw kerfs from each other but remain connected, physically and optically. From the light distribution that hits the four PMTs, it is possible to reconstruct the position of the gamma interaction⁴. LSO has a scintillation decay time of roughly 40 ns, which is very fast for a solid scintillator, and therefore many independent events can be distinguished, which means that the PET scanner can be run with stronger radioactive source to improve image contrast and resolution. This leads to better statistics and hence better resolution of the reconstructed image. For the experiment described in this thesis, neither high count rates nor fast decay times are necessary.

The PET's capability to reconstruct an image from the detected energy, position and timing comes from a coincidence arrangement of two gamma events in the crystals within a very short time window (typically in the range of hundreds of ps). The positions of coincident events, within the time window, and which also fall in the expected energy window of the 511 keV

³lutetium oxyorthosilicate is used for its high absorption coefficient and fast scintillation decay time.

⁴From this follows that the sensitivity of such a block is slightly decreased towards the corners.

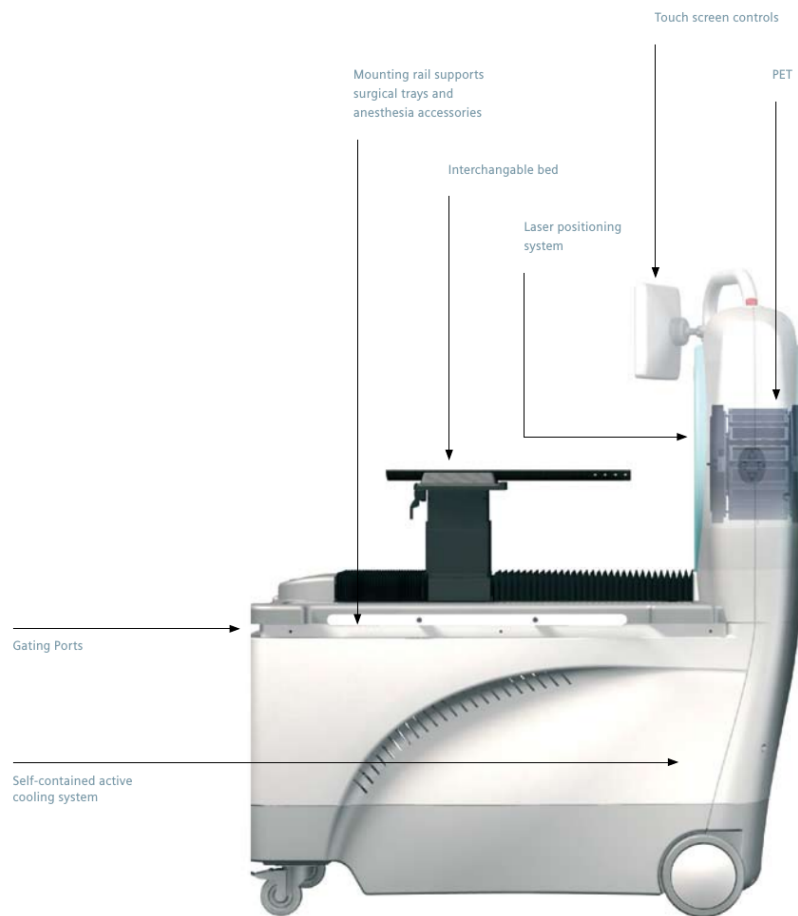


Figure 7.5: Schematic drawing of the Inveon PET scanner[54].

gamma, are used to reconstruct the image via the filtered back projection algorithm or Radon transform⁵, in the easiest case, more elaborate algorithms are subject of research [42] or have already reached production stage. The PET imaging technique requires the introduction of a radioactive tracer in the body. Depending on the element used the positions of the tracer usually indicate regions of high metabolic activity and can hint to a cancerous tumour. Figure 7.6 shows a reconstructed picture of a mouse's head together with MRI images. These techniques have different advantages in detection capabilities versus image resolution, but they work particularly well when they can be combined. A possible tumour can be located very well by the PET, while the MRI delivers a very good picture of the surrounding tissue and the position of the tumour relative to other body parts. The PET image capabilities stem from how the tracer is metabolised by the tumour, providing for many β^+ decays at the location of the tumour, which is then reconstructed into a picture.

In general, it is true that the PET image only develops by considering all recorded

⁵introduced in 1917 by Johann Radon

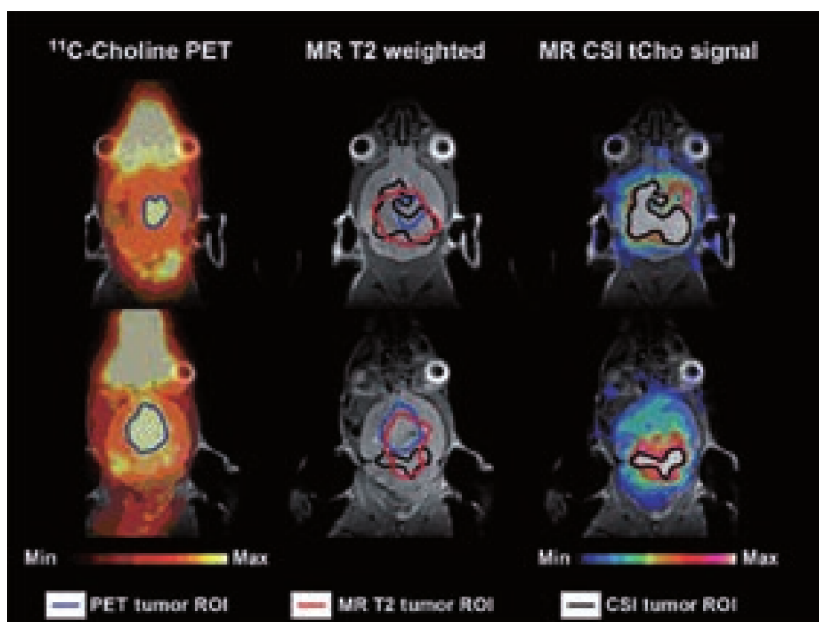


Figure 7.6: PET and MRI images of a mouse's head. ^{11}C was used as a tracer. [21]

events and their statistical distribution along the detector tube's surface. A single pair of hit coordinates is of little use for image reconstruction. On the other hand, for the spatial reconstruction as proposed in this thesis, the imaging capabilities of the PET do not matter, but it is necessary to achieve a reasonable timing along with the coordinates on an event-to-event basis. In addition to the temporal coincidence between two hits in the PET, a coincidence in the germanium is required as well. While the Inveon PET detector is specifically designed to catch very fast coincidences, and also the germanium detector's signal is sampled with 100 MHz, meaning a 10 ns timing resolution, it is still a challenge to bring those two systems together and run them in a time synchronised mode. Especially since neither is originally designed to communicate well with the other system.

7.4 RADIOACTIVE SOURCE

The selection of the source is crucial for the experiment. The source has to produce gammas at high energies to increase the probability of pair production. This is determined by the choice of isotope. The rate should also be in the right range, high enough to provide enough statistics and yield an acceptable measuring time, and low enough in order to not produce too much pile-up. After all, the waveform at different locations is the sought-after metric and should be kept as pure as possible.

For the first preliminary tests of this experiment, a ^{228}Th -source was used with a full energy peak at 2614 keV, yielding a double-escape peak at 1592 keV. For the actual experiment, a ^{56}Co -source was used. The source was produced at the synchrotron of the *Forschungszentrum*

Rosendorf by the group of Stephan Preusche with a starting activity of 4.6 MBq⁶ (measured 27.10.2015, see Appendix A). ⁵⁶Co has several high-energy lines, the most interesting ones are at 3253.5 keV and 2598 keV with their respective DEPs at 2231 keV and 1576 keV, and with their branching ratios of 7.93 % and 17.28 %. The big advantage of cobalt is that this isotope does not occur naturally and events at these energies that have coincident PET events must necessarily originate in the external source. Th-228, and its successors in the decay chain, on the other hand are unfortunately relatively abundant in most materials and can therefore induce background events. The reconstruction algorithm assumes a direction along the collimation axis, which for background events is not given and hence delivers a falsely reconstructed interaction point.

⁶This rate was limited by legal restrictions on the maximum amount of a radioactive isotope a facility is allowed to produce per year.

8

Results of the PET experiment

It is a good morning exercise for a research scientist to discard a pet hypothesis every day before breakfast. It keeps him young.

Konrad Lorenz

This chapter will present the analysis of the measured data; from describing the analysis stages to presenting the results, discussing the problems, and presenting possible approaches to overcome them. The different consecutive stages of the analysis setup are described and the results will be presented for each stage. It begins with explaining how the germanium pulses are transformed to energy values and how they are calibrated. Thus making it possible to only select events with energies in the range around the DEP energies. The process of correcting and then merging the PET and germanium data to produce coincident events is not an easy task, but crucial for the experiment. As described in the previous chapter, a pulser pattern is introduced in both systems each second. These patterns are extracted from each source and consecutively aligned against each other, correlated, and used to correct the timestamps. For this task two different methods are presented: the *time difference method* and the *fitting method*. They will be explained in detail in chapter 8.3. From the aligned timestamps of both data sets, it was tried to find coincidences between PET events and DEP events in the germanium. The results and issues with this analysis step and the investigation to get to the bottom of this problem will be presented in chapters 8.4 and 8.5, respectively. An outlook on how these problems could be overcome is given at the end of this chapter.

8.1 ANALYSIS AND RESULTS

ANALYSIS SETUP

The analysis is done in ROOT, the analysis toolkit of the high energy community, developed by CERN. It is mainly developed in C++ and offers good analysis capabilities for file sizes that do not fit into memory. ROOT was used in version 5.32. Various analysis stages were implemented for each detector system and, after merging them into a combined data set, for the merged data. Each step transforms the data, merges the data of the two detector systems together or otherwise treats the data. For each step a separate script is implemented and a separate file with its own data structure is created and saved. This was done in order to be able to work independently on the different analysis stages without having to reprocess all data every time. The analysis process is sketched in Figure 8.1 and will be covered in more detail in the following.

The main stages that transform the data from the raw recorded pulses of the germanium detector to a selection of waveforms at a certain interaction point in the detector is quickly sketched:

1. At the first stage the raw germanium pulses that are stored in a binary format are converted to ROOT format.
2. The waveforms are digitally processed using several moving window average and differentiation filters. The result is a single energy-like value per event, measured in arbitrary units.
3. The gamma lines of the ^{56}Co source are used to calibrate the energy spectrum. A second-order-polynomial is used to fit the observed peaks to the known energies of the ^{56}Co -lines.
4. The timestamps of the events in both DAQ systems are extracted, labeled according to their origin and the time change is corrected for. The germanium and the PET system each record two different types of events. The FADC connected to the germanium detector records:
 - events triggered by an energy deposition in the germanium
 - events triggered by the external pulser

each in its own channel, so that different event types are easily distinguishable.

The PET scanner records two different sets of events as well:

- events triggered by a coincidence of two scintillator cells at an energy of around 511 keV

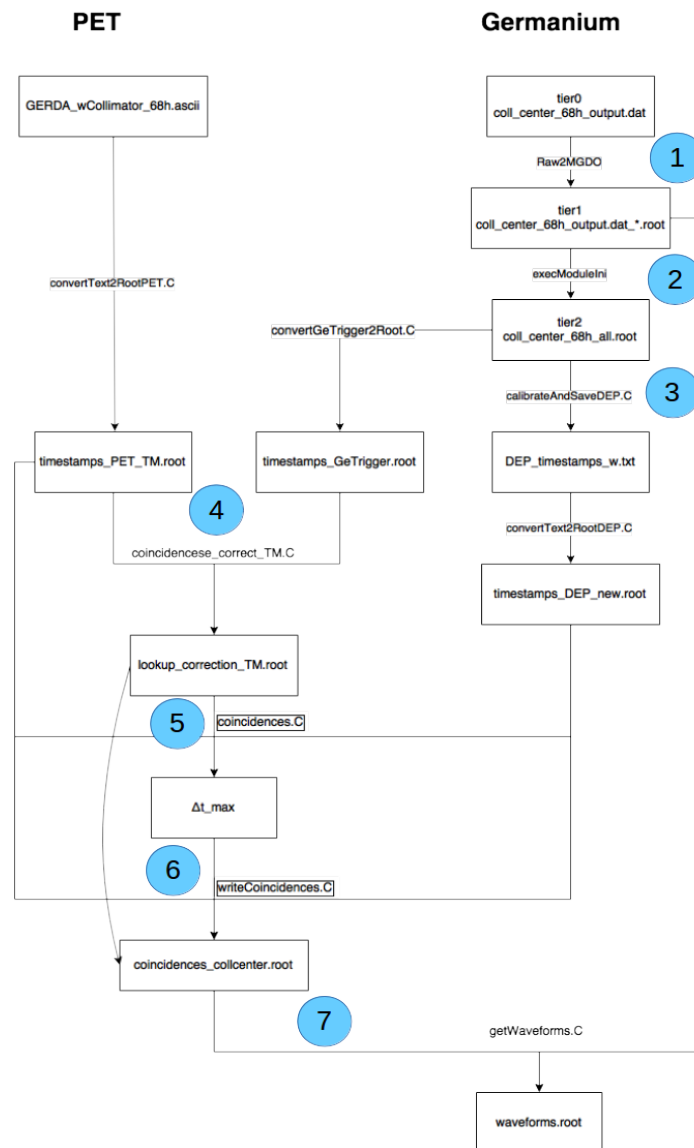


Figure 8.1: The figure depicts the analysis flow for the two detector systems. The different stages: conversion into ROOT format, calculating the energy from the waveform, calibration, merging of the two different paths, finding coincidences are described in more detail in the text.

- events triggered through the external trigger port. These are all events triggered by the germanium system, either due to an event in the germanium or through the external pulser.

The different types cannot be easily distinguished in the PET system, they appear in the same data channel and there is no energy information. But when looking at their timing structure, it is possible to extract the time marker pulses. This is why the threefold pattern was introduced.

5. The external trigger timestamps of the germanium and the PET data are fused together and the time shift between the two DAQ systems is determined.
6. The time shift is used to correct and align the timestamps. Now coincidences between PET and DEP germanium events within a time window Δt are created.
7. The spatial reconstruction is performed for the events selected in the manner described above. Waveforms originating in the same detector region are averaged to produce one typical waveform per detector segment.

The individual steps of the analysis procedure are described in more detail in the next sections. In addition to the ROOT analysis, another analysis was done in Python and there using mainly the Pandas (Python Data Analysis Library)[45]. This was done in an approach to check some new analysis ideas and find the root cause of the problem that not enough coincidences were seen in order to be distinguishable from background. This package allows a higher flexibility and development speed. It was also used to double-check the analysis done with the ROOT package. Most of the plots in this work have been produced with python's `matplotlib`, which allows easier graphics setup and customising of the plots.

8.2 ENERGY SPECTRUM

A relatively easy part, because it is fairly standard, is the determination of the energy spectrum of the ^{56}Co source in the germanium detector. Starting from the digitally sampled waveforms measured in the germanium detector an energy has to be determined. The waveform measured is created by charges drifting through the detector and the height of the waveform is roughly proportional to the energy deposited in the interaction, but slight variations in the arrival times, and thus pulse shape, may lead to differences in pulse height, even at the same energies. The determination of this height, and the shaping and filtering is done with the Gaussian algorithm, which does not only consider the maximum pulse height, but includes the shape of the waveform around the rising edge of the pulse as well. For the Gaussian algorithm, a number of moving window average transformations with window width τ are applied. This shapes the signal into a quasi-Gaussian pulse. The moving window average acts as a low-pass filter, eliminating higher frequencies, that are typically attributed to noise. The maximum amplitude is then taken as the energy value. For the experiment five moving

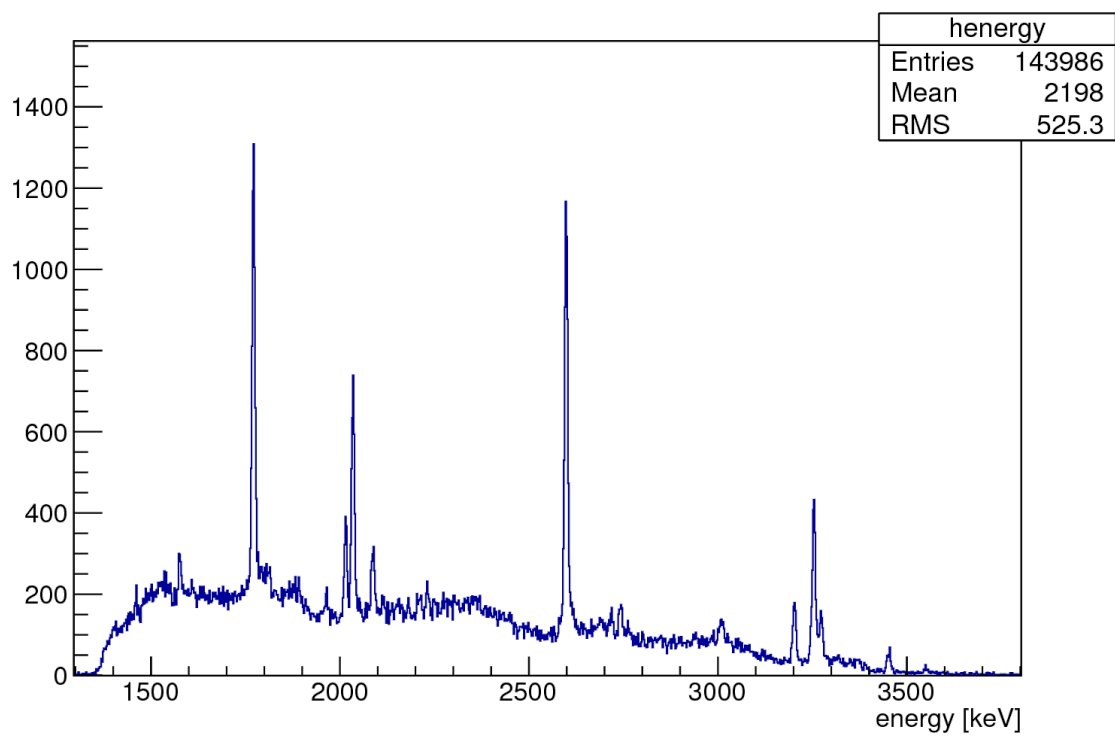


Figure 8.2: Energy spectrum measured by the germanium detector. Main full energy (FEP) lines are located at 1771 keV, 2598 keV, 3201 keV, and 3253 keV. The single escape lines (SEP) can be seen at 2087 keV and 2742 keV, even though barely. The double escape peak (DEP) can be found at 1576 keV and 2231 keV. Again the DEP, as well as the SEP, of the 3253 keV line are much harder to spot.

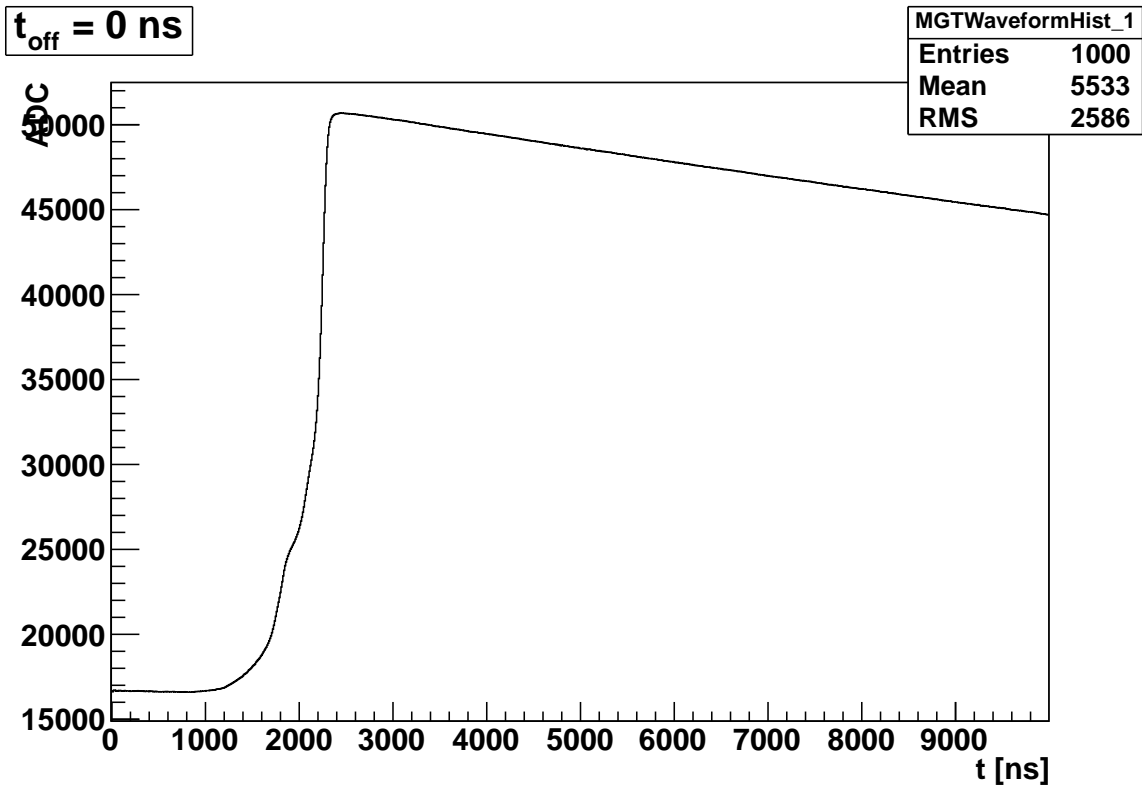


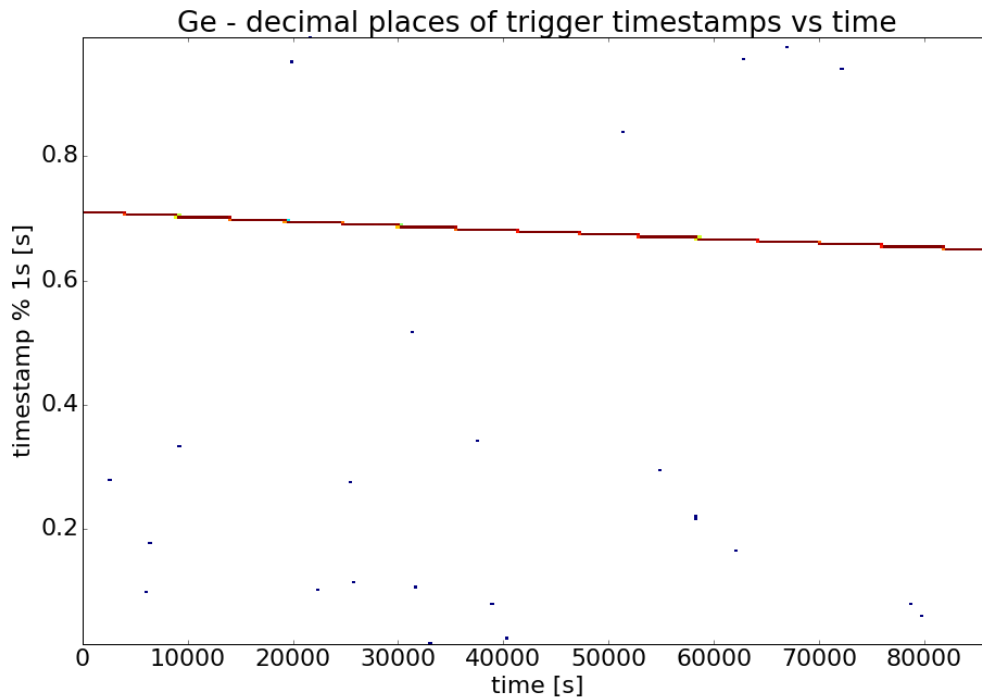
Figure 8.3: A waveform recorded by the germanium detector. One sample corresponds to 10ns. The amplitude is measured in ADC units.

window averages with $\tau = 3 \mu\text{s}$ were applied. This is not the optimum and a better energy resolution would be possible in general, but the width of the recording window would have to be changed. The energy resolution is not limiting the performance of the experiment, therefore it was decided to rather optimise the maximum trigger rate and keep the window size small.

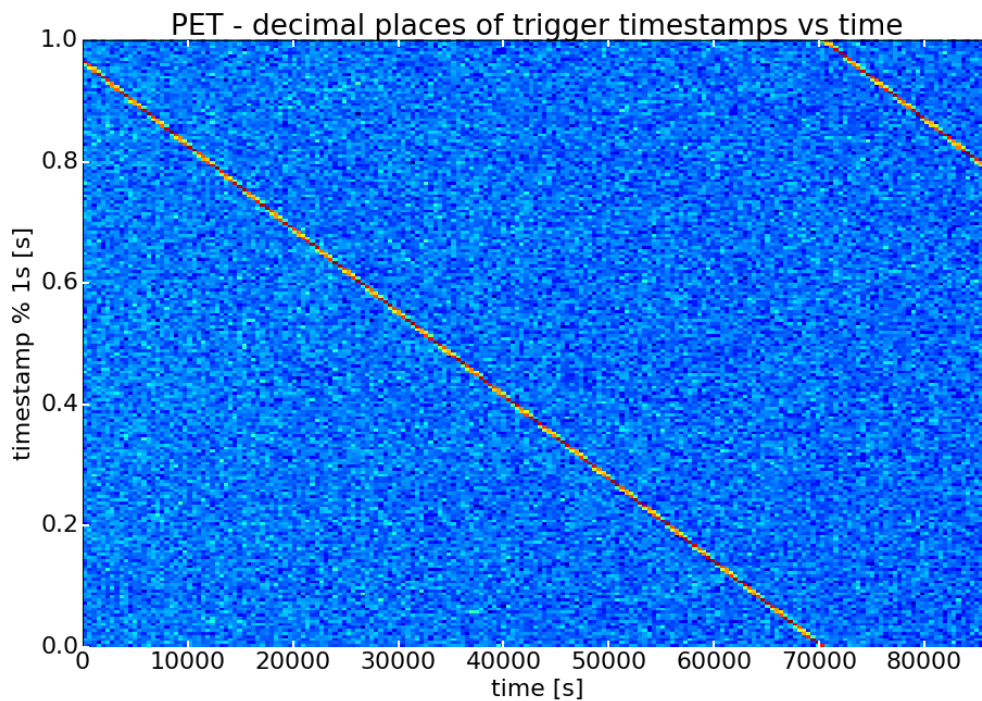
The measured energy spectrum can be seen in Figure 8.2. The full energy peaks (FEP), single-escape peaks (SEP), and double escape peaks (DEP) of several ^{56}Co lines can be seen. The energy lines of interest for the experiment are the DEP lines. The energy resolution was measured to be 10.1 keV FWHM at 3201 keV (3.2‰)

8.3 TIME SHIFT CORRECTION

The two internal clocks of the two independent systems, one being the FADC with the read-out computer attached to the germanium detector and the other the PET scanner with its data acquisition system, might not be stable on the \sim hundreds of μs level compared to each other. Especially their relative time shift, the time shift of the clocks running in different directions, or at least with different speeds, is of concern for this experiment. Therefore the timing marker was introduced every second in both systems to allow to correct for possible deviating clocks. There are two types of events in both DAQ systems, physical events and



(a) The time shift of the trigger pattern for the germanium detector and recording system.



(b) The time shift of the trigger pattern for the PET Inveon system.

Figure 8.4: The time shift of the trigger pattern can be seen in the shift of the decimal places of the triggers for the germanium (8.4a) and the PET system individually (8.4b). The floating point modulo one second is taken of the timestamps. The different slopes and the different amount of “noise” events can be clearly seen, due to the PET system not being able to distinguish between events from external trigger and germanium system.

timing markers. The latter are used to correct the absolute timestamps and make them comparable across both systems. The physical events with their corrected timestamps can then be used directly to look for coincidences in PET and germanium detector.

There are two possible approaches in relating the events in the PET data with those in the germanium data and eventually create coincidences:

1. Use only the PET data to find coincidences between events from PET (`isTrigger==0`)¹ and events coming from germanium tagged with the coincidence marker (`isTrigger==1`). This approach uses only the data recorded in the PET. Events that triggered the germanium DAQ enter the PET system via the external trigger port and are tagged as such. To relate the energy and waveform, which is information not available in the PET, to these events, they have to be matched against the germanium data via the time differences between the events. The timestamp is not reliable for both systems over long periods of times, but the short time differences can be compared to each other and thereby an event by event assignment can be achieved. Since events can be missing in either DAQ system, a fault tolerant assignment system has to be implemented. The method will be called the *time difference method*.
2. Use the trigger pattern present in both systems to match the time pulser events that are induced every second. Over time these trigger packets are drifting slowly apart. Correct for the time shift by fitting a correction function. Then use corrected timestamps to find coincidences. This method will be referred to as the *fitting method*.

In the end the difference in the methods comes down to first identifying coincidences and then after that relate the energies from germanium to the coincidences found (*time difference method*) or first making the timestamps comparable across both systems and then looking for coincidences (*fitting method*).

8.3.1 THE TIME DIFFERENCE METHOD

In order to identify coincidences, only the data that is taken by the PET system is used. Events from physical PET events (`isTrigger==0`) are related to those events from the germanium (`isTrigger==1`). Apart from a possible offset that could potentially take place in either the intrinsic PET system or the system for external trigger markers, the timestamps can be directly compared to find coincidences. Only when more information about the event is wanted that is stored in the germanium data (e.g. energy or the waveform), is it necessary to relate the germanium timestamps to the events from the PET detector. It is then possible to correlate these events to each other by going step-by-step through both data sets.

The fact that the time frames of the data acquisition systems and the pulser are shifting relative to each other can be seen in Figure 8.4; for the germanium in Fig. 8.4a and for

¹`isTrigger` is the name of the variable used to distinguish the origin of an event. `isTrigger==1` are events triggered through the input port, so either time marker or germanium events.

the PET system in Fig. 8.4b. A 2-dimensional histogram of the timestamps modulo 1s, i.e. the decimals of the timestamps versus the timestamp is shown. It shows a uniform random distribution of events plus a line stemming from the trigger that pulses every second. In case of the germanium DAQ, shown in Figure 8.4a, the events from trigger and from detector can be distinguished and so the picture is cleaner with fewer background events as in the case of the PET, as can be seen in fig. 8.4b. The few events are due to rare faulty events from either the pulser or the FADC. The FADC is known to occasionally have problems with the buffer, reading out both channels when only one channel was triggering. The decimal places of the timestamps from the trigger should stay the same, or at least change with the same velocity for both systems. This is obviously not the case, the three systems, the DAQ of PET and germanium and the trigger, are not running synchronously. This should be corrected for.

With this method it is assumed that the relative change of the internal clocks inbetween two pulses can be neglected. Each one-second interval of one system is assigned to another one-second interval in the other detector system, times are corrected by subtracting the timestamp of the starting trigger of the interval. While the FADC connected to the germanium detector yields very accurate timing information, the PET system is limited to timing bins of $200 \mu\text{s}$ width. This means that the synchronisation pattern of three pulses with a $50 \mu\text{s}$ spacing, is either recorded with the same timestamp, or eventually has one pulse assigned to the leading or trailing time bin. Then events can be correlated to each other, either to check for coincidences or to assign the germanium energy to the corresponding PET event. The fact that it is not known which trigger event in one system corresponds to which trigger event in the other system can be overcome by shifting the starting points relative to each other by adding an offset and check where more coincidences occur. In case of a trigger event mismatch the number of coincidences should only correspond to the number expected from accidental coincidences, and be maximal when the correct time offset between both systems is found.

8.3.2 THE FITTING METHOD

Another approach is to fit a function to the two-dimensional histogram of the timestamps versus the modulo 1s of the timestamps and use this function to correct the timestamps. This is done for both DAQ systems. The two systems differ in resolution and their characteristics in the sense that the germanium and trigger signals are each recorded in their own channel by the FADC and can therefore be separated easily. The challenge with the PET system is, that signals coming from the germanium detector as well as those from the pulse generator are recorded on the same input port and cannot be distinguished. While the timestamp pattern of the physical germanium events should be purely random, the decimal places of the pulser events when plotted over time should form a line. This line may have a slope, which reflects the non-stationary nature of either the pulser or the clock of the PET-DAQ. This line in the

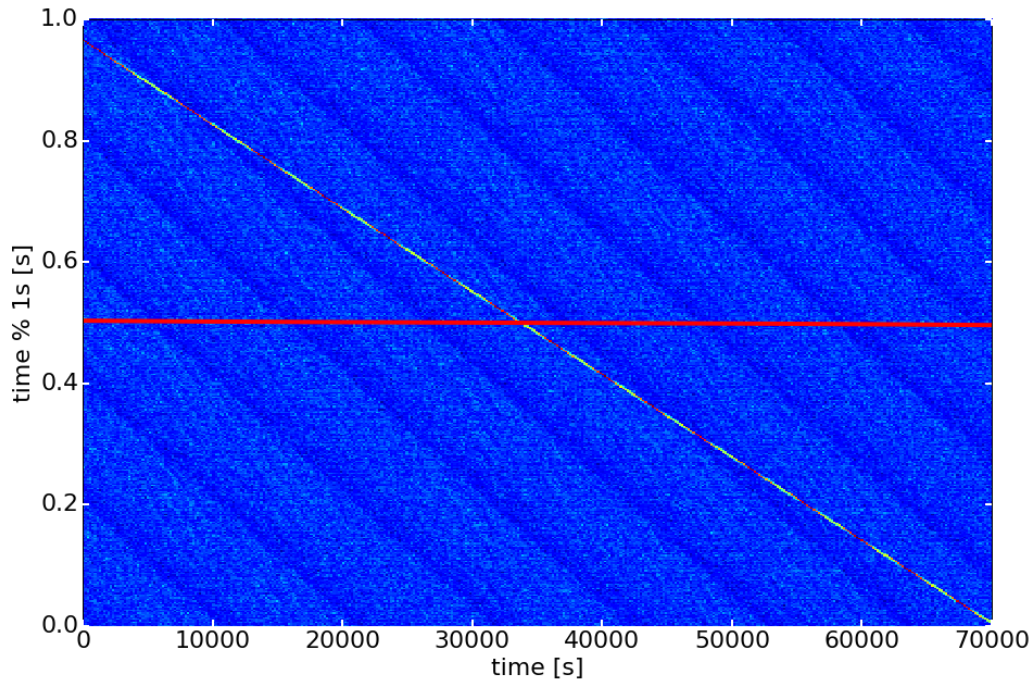


Figure 8.5: A fit to the timing distribution of the events goes wrong when events from the germanium detector are not cleaned up. The jump in decimal places as seen in Figure 8.4b is avoided by only considering the first 70.000 s.

timestamp modulo 1 s plot can be seen in Figure 8.4b for the PET and in Figure 8.4a for the germanium. Looking at both graphs, it is obvious that the time variance differs in the two systems. The idea now is to correct for this discrepancy between the systems by correcting the time shift and matching the pulsers to each other. Then coincidences between the PET and the germanium systems can be searched for, based on these corrected timestamps.

First thing, the events coming from the pulser have to be separated from the events from the Ge-detector. If this is not done, the fit to this clearly visible line in the plots of the decimal places versus time (Figures 8.4b and 8.5), goes wrong. A jump in the decimal places of the timestamps occurs around 70.000 s when the remainder of the timestamps reaches the full second. To be able to consider the whole range of recorded data, the floating remainder is shifted by one second for timestamps < 70.000 s. This allows a continuous fit to the pulser events. The effect of this shift is demonstrated in Figure 8.6.

For a later stage of the experiment, when the coincidences didn't show up and it was assumed that the trigger signals fell in some kind of dead time of the PET, a time delay unit was added to postpone trigger signals. This way trigger signals should be recorded and the constant time shift could be subtracted. Due to the special characteristics of the time delay electronics the 3-fold pattern created by the pulse generator is only passed on as a single, yet delayed, pulse. Hence the distinguishable 3-fold pattern is lost which makes it a lot harder to separate the two event types. Some kind of statistical method must be used in order to distinguish the

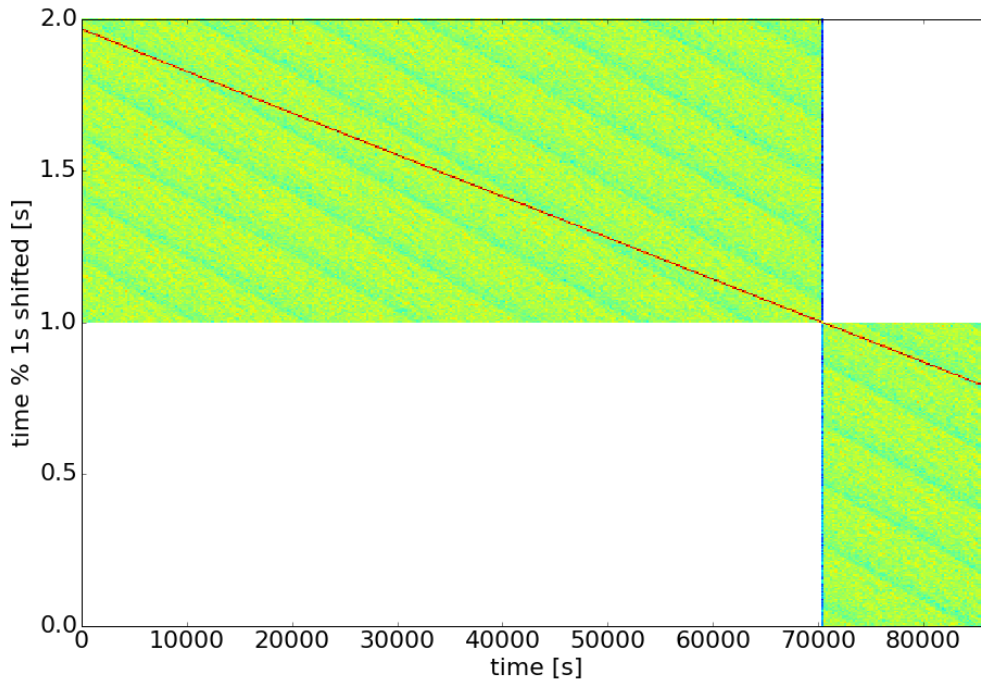


Figure 8.6: The remainder of the floating point division of 1s is shifted up by one second for timestamps smaller than 70300.624 s. This creates a continuous slope in the line of pulser events.

pulser events from the physics events. The pulser pattern is sent out every second and the deviation of the clock should be small, so the decimal places of the timestamps should be the same for a reasonable amount of time. To isolate pulser events a method that could be called "moving window histogram" is used. A moving window of size 1000 events is moved through the data. The length of this window corresponds to roughly 10 s. Within this window the decimal places of all timestamps

$$t_{mod} = t \mod 1s$$

are taken and put in a histogram. The bin size of this histogram is chosen to 1 ms, which corresponds to 1000 bins in the possible range of the decimal places 0..1. The maximum of this histogram is returned and corresponds to the decimal places of the pulser within this window. This assumes that the rate of change of the pulser decimal places is smaller than 1 ms per 10 s. This assumption holds true as can be seen from Figure 8.4b where the decimal places change less than one second within 70 000 s

$$slope < \frac{1s}{70\,000s} = 14\frac{\mu s}{s};$$

within the 10 s window the rate of change with $\sim 14\mu s$ is hence a lot smaller than the chosen bin size of 1 ms. Therefore the decimal value of the pulser can be considered constant for the

time interval considered. The resolution of 1 ms is larger than the theoretically achievable resolution given by the PET data acquisition system, which is 200 μ s. The 1 ms resolution is used to roughly locate the pulser within the other obfuscating events. The total resolution is pushed down to a level of $< 200 \mu$ s by fitting a correction function to the changing decimal places of the pulser events. This is described in the next section.

THE CORRECTION FUNCTION

The idea behind the correction function is to correct the timestamps of the pulsers to a constant decimal places value, for germanium as well as for PET data, allowing to directly compare the timestamps. Since the behaviour of the pulser is known (three pulses @ 50 μ s per second, i.e. one pulse per second in the case of the PET with the delay electronics), the pulser events can be used to align the timestamps. The assumption being, that if the pulser events are aligned, so are the physical ones, that unfortunately do not bear such a characteristic timing pattern.

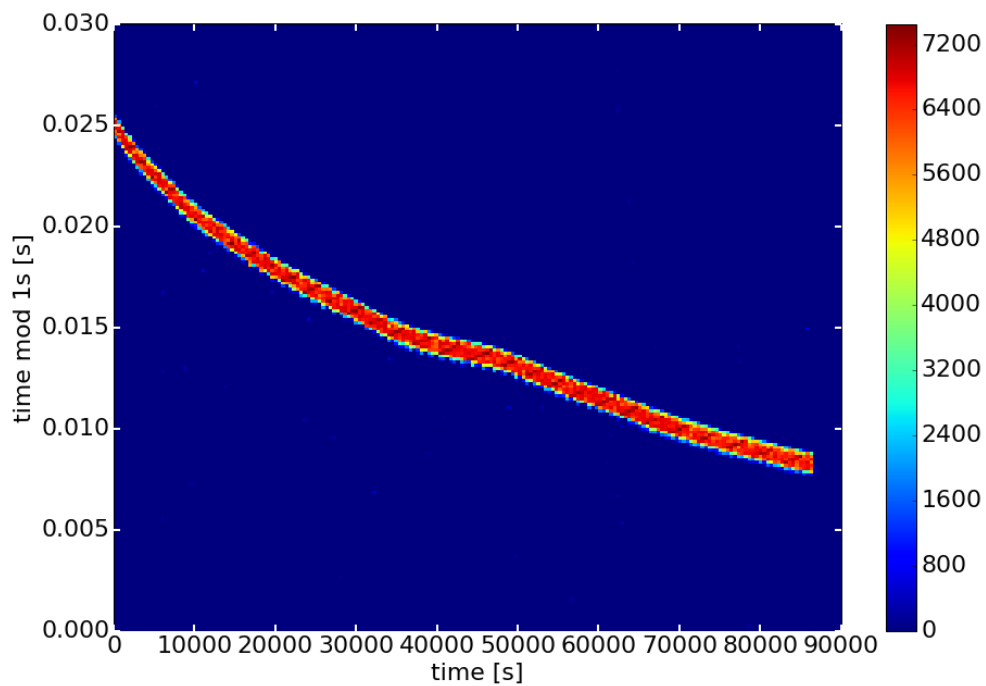
The correction process has to be done for PET and germanium events separately, yet the idea to consider, fit, and later correct the modulo(1s), i.e. the decimal places of the timestamps is the same for both data sets.

Although in both cases the behaviour is roughly linear, at least on the large scale, it turns out that it is beneficial to use a 7th degree polynomial as a fitting function. Polynomials of lesser degree do not succeed in correcting the pulser events to values below the required threshold over the whole measuring cycle, while higher order polynomials do this, but at the cost of more wiggles in the corrected data. The threshold was chosen to be 500 μ s, this is slightly more than two time bins and encloses almost all events after correction. Coincidentally the 7th order polynomials work best for both sets of data. The result, the timestamps corrected by the fitted function, is displayed in Figure 8.7 and Figure 8.8. In the case of the PET data, where the pulser events cannot be clearly separated from the physical germanium events the histogram of the modulo(1s) vs. timestamps is much more cluttered and therefore the fit does not converge as well as in the case of the germanium data. Two additional tasks need to be added in case of the PET timestamps:

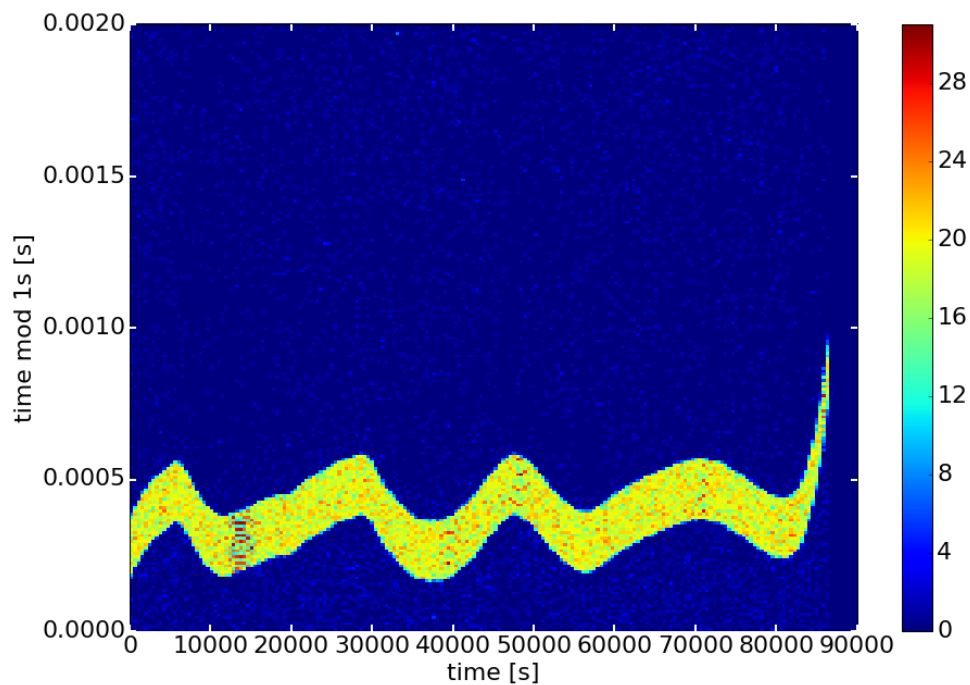
- fit to histogram, suppress small values
- repeat polynomial fit

While the fit to the germanium data is done using a least square fit to all data points, the correction function to PET data is fitted to a 2D-histogram of the data points. To reduce the deteriorating effects of outliers, bins of the histogram below the threshold value of θ_{thr} ($\theta_{thr} = 1000$ for a 2000 x 2000 bins histogram) are set to zero. Then the fit is run a second time, to bring the deviations between the fit and the pulser events below the threshold².

²In principle it should be possible to get one polynomial function that corrects the timestamps instead of two functions that are applied consecutively. But it appears that the fitting routine runs in a local minimum



(a) Decimal places of the timestamps after one correction with a polynomial of degree 7.



(b) Correction applied for a second time. Again with a 7th degree polynomial.

Figure 8.7: Decimal places of timestamps of pulser. After applying a fitted correction function one 8.7a and two 8.7b times.

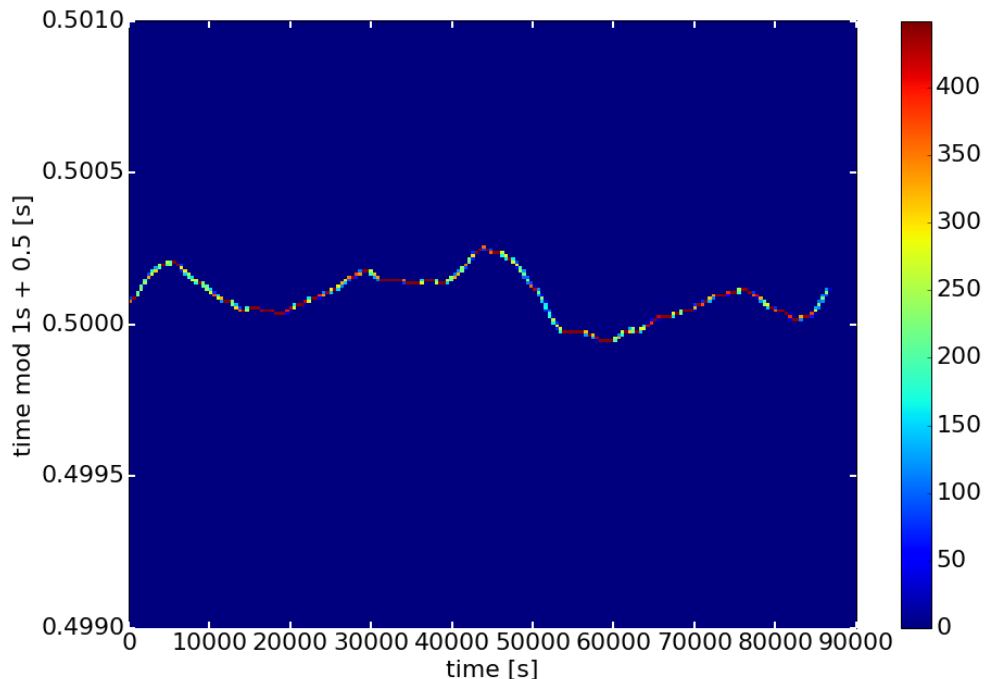


Figure 8.8: Corrected decimal places for germanium events. Again a 7th degree polynomial is chosen. The decimal places are shifted by 0.5 s in order to accommodate them better in one graph.

After the delay electronics were introduced that reduced the timing pattern to only one pulse per second, the method was switched to the moving window histogram method described above and the fit was applied to the maximum values of those histograms.

The correction functions that best represent the data for both data sets are then subtracted from the data. Constant pulser events as seen in Figures 8.7 and 8.8 are then obtained. The correction functions are also applied to non-pulser events. Subsequently, events can be compared directly between DAQ systems, disregarding a possible constant offset of integer seconds. But this unknown offset of not knowing which pulser event corresponds to which can easily be tested since only a handful of possible values are in possible range, i.e. the time it took to start the PET system after having started the germanium system ($\sim 3 - 4$ s).

8.4 COINCIDENCES

The crucial part of the experiment is to find coincidences between events in the germanium detector with an energy deposition of the DEP energies and events in the PET that already satisfy a coincidence condition of themselves, namely two 511 keV gammas need to be detected in two distinct PET cells. The necessary correction methods have been described above and now the results for the two methods will be presented. The *fitting method* corrects and therefore does not return the function which minimises the deviations on a global scale.

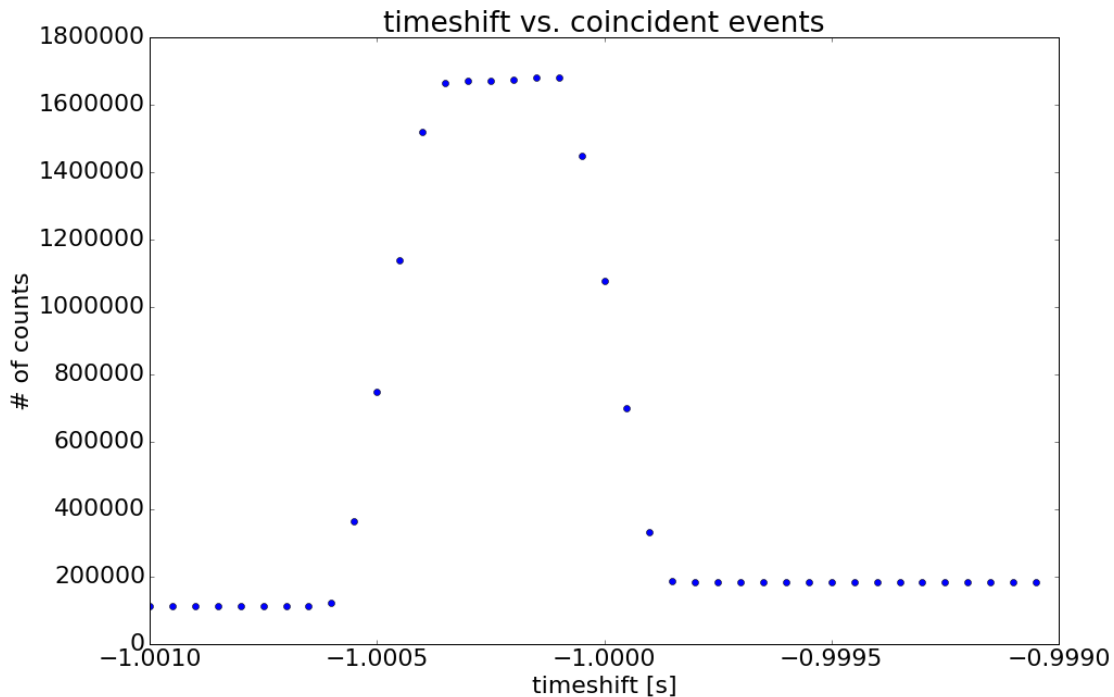


Figure 8.9: The absolute time shift between the two systems is not known, by shifting the corrected timestamps relative to each other the actual time shift is found at the time shift value with the highest number of coincidences.

timestamps of both systems and allows to directly compare them, the results are shown in chapter 8.4.1. The *time difference method* initially uses only data available in the PET, the coincidence information of the germanium being passed along via the external trigger port, and is presented in section 8.4.2. Both of these methods show no selection of coincident events that would show as a surplus of events at DEP energies. Therefore in an attempt to avoid possible problems with the setup an alteration of the experiment was tried out by including a delay electronic module. But unfortunately, the analysis of the extended experiment did not yield improved results. They are described in section 8.4.3.

8.4.1 COINCIDENCES FROM PET AND GERMANIUM DATA

How the correction function is found is described in the section about the *fitting method* above. After correcting the timestamps with the correction function, the germanium timestamps should be easily comparable with the PET timestamps, apart from a small possible technical offset due to unknown delays in either system and the different starting points when initiating the measurement. The correct relative position between the two DAQ systems can be determined by shifting the timestamps relative to each other and counting the coincident events within $|\Delta t| < 200 \mu\text{s}$. As a function of the time shift, a curve with a peak at the correct time shift is obtained (Figure 8.9). The best time shift parameter is found to be

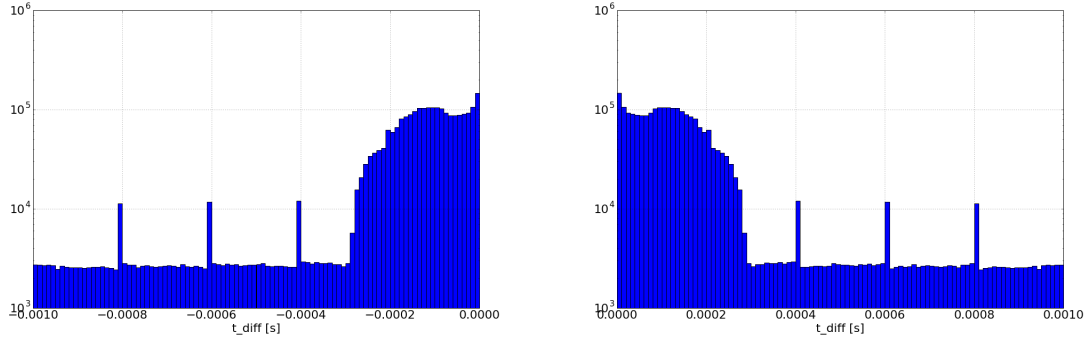


Figure 8.10: Distribution of time differences between events, including triggers, PET and germanium events. Most events are contained within $\pm 300 \mu\text{s}$.

$\Delta t_{best} = -1.00015\text{s}$. At this value, the number of coincidences between PET and germanium detector are maximal, for other time shift values only random coincidences are counted, which are less frequent.

So when the timestamps are corrected with their respective correction function, and then aligned by the right time shift, the timestamps can be directly compared.

This yields a distribution of time differences between events as shown in Fig. 8.10. A majority of events is contained within $\pm 300 \mu\text{s}$. This includes all three types of events. Now the coincidence cut can be applied to get only events that deposit energy in the germanium and at the same time produce a double coincidence in the PET detector. When the events with a time difference between a PET and a germanium event smaller than $|\Delta t| < 400 \mu\text{s}$ are selected, they would be expected to have an excess at DEP energies of the ^{56}Co -lines. The most important ones are 2598 keV (DEP at 1576 keV) and to a lesser extent 3253 keV, with the DEP at 2231 keV. But there is no excess detected as can be seen when comparing Figure 8.11 (b) to 8.11 (d). The events selected via the coincidence in both systems produce an energy spectrum that apart from fewer statistics has the same shape as the energy spectrum with no cuts applied.

When analysing the peak at 1576 keV in more detail, the number of events in the peak is $18.6\% \pm 0.5\%$ above the expected background for the histogram with no cut. After the coincidence cut is applied, the peak is $43.7\% \pm 16.1\%$ above background. This isn't visible by eye, and the statistical significance is very low with the percentage with cut being 1.56σ away from the percentage without cut. Therefore we cannot assume that there is an effect hidden in these spectra and that there are no, or too few to detect, coincidences in the data. When taking accidental coincidences into consideration, it turns out that the observed number of events at all energies after applying the coincidence cut, is around the expected number of events from coincidences. Using one measurement from 16 March 2016, exemplarily, that contained 7018498 events from trigger port (Ge and pulser) and 1729776 events from PET, with the coincidence window of $400 \mu\text{s}$, 56205 accidentally coincident events are expected. After the cut, 66138 are observed. This would agree very well with the number of expected

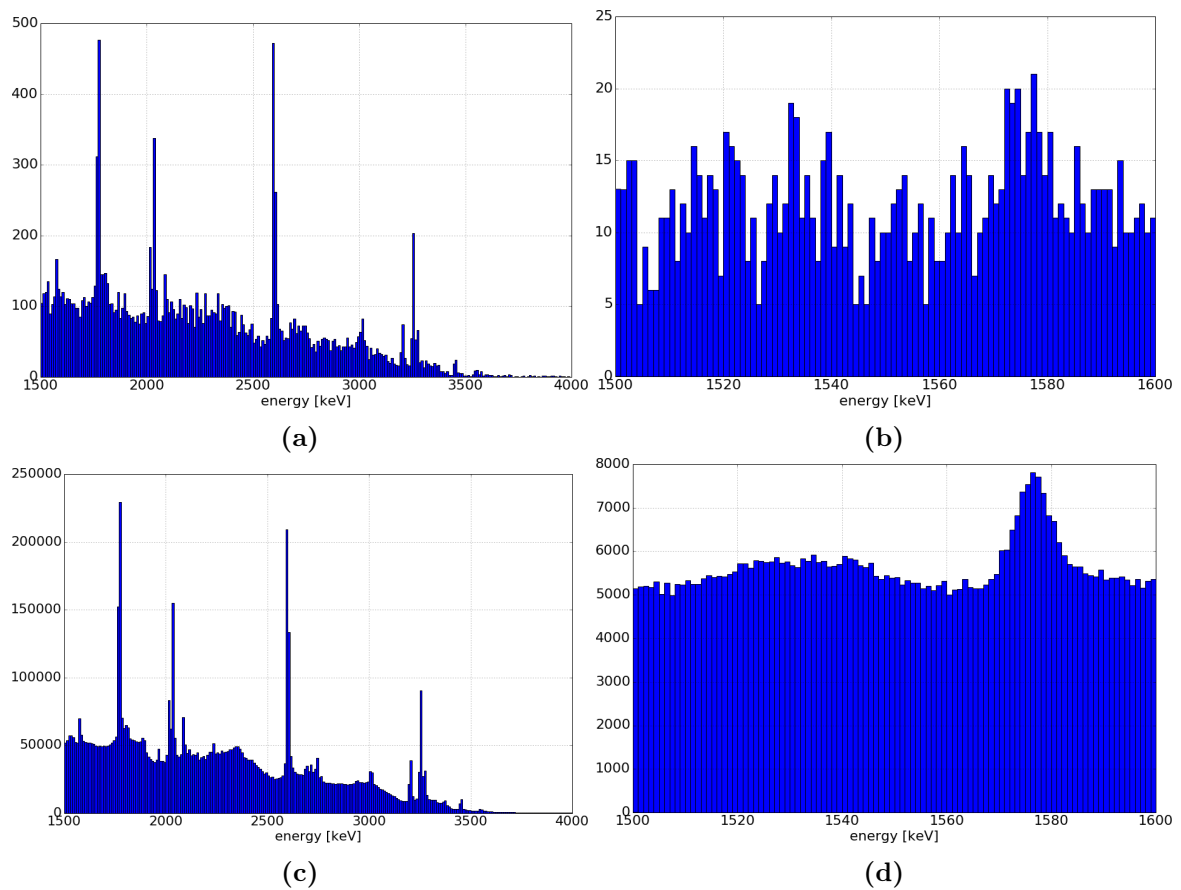


Figure 8.11: Histograms obtained when applying the $|\Delta t| < 200 \mu\text{s}$ coincidence cut between PET and germanium events, (a) and (b). No difference in the spectrum or excess in DEP energy events at 1576 keV is observed when compared to all energies, (c) and (d). While the statistics of the histograms in the top row are much lower, the general shape of the full spectrum is clearly visible. A prominent peak at the DEP energy of 1576 keV and high mostly suppressed energy spectrum would have been expected.

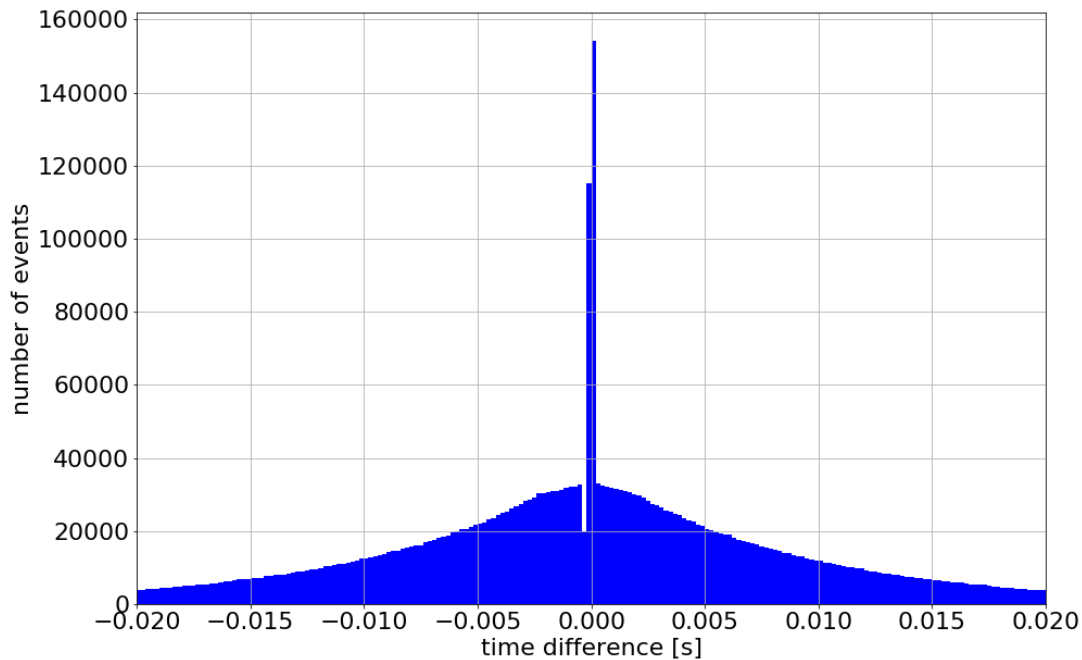


Figure 8.12: Distribution of time differences between a trigger event from germanium followed by a coincidence event. Only data from PET DAQ was used for this plot. The time differences follow an exponential distribution, a clear peak at 0s which is preceded by a deficit at $-200 \mu\text{s}$.

events from the simulation, which was between 6394 and 41818 events, only that they are expected to show up at DEP energies, which they clearly do not.

With the selected events showing no clear preference for the expected energies, further analysis like location reconstruction or building a pulse shape library in dependence of the location cannot be carried out. The next few sections are trying to find out why these coincident events are missing; where possible mistakes were made or other problems exist.

8.4.2 COINCIDENCES WITHIN PET DATA

The *fitting method* apparently has some problems, so it was tried to use the *time difference method*. For this method, only data that is recorded in the PET is used to find coincidences. Only when information about the energy of the event or the pulse shape is needed, does it become necessary to find the corresponding events in the germanium data. The motivation for this method being that there could be some issues with the correcting and assigning of the timestamps with the *fitting method*, that this method does not have.

The data for this method is fully contained in the PET data itself, at least the data needed for the coincidences. Besides the PET events it also contains information coming from the trigger input port, which contains data from the germanium and the pulser channel. There

is only information about the timing of the germanium events, the energy and pulse shape information is in the data from the germanium DAQ and has to be aligned with PET data. But even this information is very valuable and shall be used for a quick check whether relevant coincidences can be seen in this PET data only.

When the time differences between PET events and the closest germanium events are put in a histogram, there should be a preferred time difference that is realised more often than any other time difference and should stick out. It does not necessarily have to be at time difference zero, there might be a technical offset in either system which should be constant though. The only peak that sticks out, as can be seen in Figure 8.12, is a peak around 0 s time difference, which fits well to expectation.

Now those events which have a simultaneous event in PET and germanium are selected and the correct germanium energy is assigned by going through the time differences as described above for the *time difference method*. This leads to a similar plot as in Figure 8.11. Again the data show no clear preference of DEP energies, but a histogram that has the same shape as if all events with no coincidence cut were selected. So there are no coincidences at DEP energy just in the PET data either.

On further investigation of Figure 8.12, apart from the expected exponential decay of the time differences and the peak at 0 s a deficit in the $200\ \mu\text{s}$ bin right before the PET event can be seen. If this deficit occurs within $200\ \mu\text{s}$ before the PET event, this means that it occurs within $200\ \mu\text{s}$ after the external trigger event (pulser or germanium). It seems like the trigger might suppress PET events for a certain time, yet not all of the time. This is in principle what the external trigger is meant for originally, to remove certain events after the trigger to make the image sharper. But this functionality of excluding events was turned off and only the timing information of this trigger port was used. This deficit motivated the idea to delay the trigger pulse in order to move it out of that seemingly less sensitive region. The PET system should record the PET event and after a delay time should the external trigger pulse arrive and be recorded. The alignment would be no problem, since the alignment analysis was already in place and can handle constant time shifts.

8.4.3 DELAYED TRIGGER

Possibly, from the observations described above, the external trigger suppresses coincident events coming from the PET. For this reason the experimental setup was expanded to include an additional time delay to the trigger logic in order to shift the pulse out of the time range that seems to be suppressed.

All digital pulses coming out of the germanium DAQ system, that is pulser and germanium events, are delayed by 1.5 ms. The corrections of the timestamps to both systems are applied in the same way as before. To check this setup, a quick test of 10 minutes was run, without collimation in order to create triggers at a very high rate. Still applying the same analysis tool chain, when shifting the timestamps of the two data sets against each other, the offset

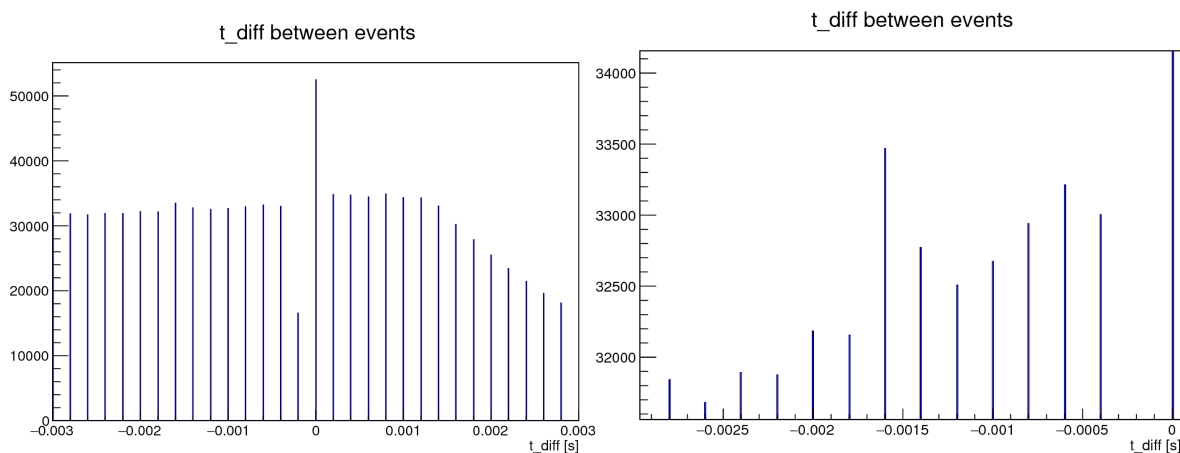


Figure 8.13: Distribution of Δt between trigger and PET events as recorded by the PET with the delay module installed in the setup. The peak at -1.6 ms (and to a lesser extend -1.4 ms) clearly stands out. The delay module was set to a time delay of 1.5 ms.

has an additional offset of the 1.5 ms (Fig. 8.13). Yet this peak at around 1.5 μ s is very small compared to the peak at 0 s that is still clearly visible. This gives rise to the conclusion that there are other timing effects going on, that somehow favour the seemingly “coincident” nature of a PET event occurring simultaneously with an event received via the trigger port. This structure in the timing patterns is further analysed in the following chapter.

8.5 ROOT CAUSE ANALYSIS

8.5.1 STRUCTURE IN THE TEMPORAL PATTERN

In this section, the efforts made in order to further investigate the reasons why the two systems cannot be aligned in time will be presented. The structure of time differences found in the data recorded by the two different DAQ systems will be further analysed.

GERMANIUM SYSTEM

The events registered by the germanium detector are events from radioactive decay which are statistically not correlated, and follow a Poisson process. The distribution of time differences between events should follow an exponential function. Figure 8.14 shows that this is true and the distribution does indeed mimic an exponential function and displays a perfectly straight line in the logarithmic plot. The FADC has a timing resolution of 10 ns since it samples the pulses at 100 MHz³ which gives the distribution a very fine granularity. Only when looking very closely with a high zoom does it become recognisable that the FADC has a dead time of slightly less than 10 μ s where no events are accepted. The peak is due to buffered events that

³At least this is the smallest resolvable time unit. The trigger time assigned to one event depends on how the DAQ system is configured and the shapes of the pulses, especially how stable or similar they are over time. But on the time scale considered, anything in that order is still very small.

are not lost, but not attributed to the correct timestamps. In principle the SIS 3302 FADC has an event buffer with two separate memory banks that should enable it to record continuously. This feature apparently has not been implemented in the DAQ software used. On the time scale needed for this experiment it does not matter, though. Thus the distribution of the time differences of the germanium system behaves completely as expected.

PET SYSTEM

While the case for the germanium events is pretty clear and the exponential shape of the time differences can be easily established, the case of the PET is a little more complicated and the temporal structures show a few peculiarities. For events coming through the external trigger port, the Poisson process seems to be valid. On a large scale the exponential (linear on log-scale) behaviour of the time differences between trigger events is there, as Figure 8.15 shows without fail. On the smaller scale, the only irregularity seems to be the dead time of the trigger port of 2 ms. But this affects only events from the germanium arriving too close after each other, and should not interfere with the coincidences across detector systems. When looking at the time differences between pure PET events (`isTrigger==0`) in Figure 8.16, a few bumps can be noticed. They appear at 0 ms and multiples of 33 ms. Also the general distribution seems to include some wave-structure and is not perfectly straight in the log-representation. When the distribution of the floating remainder of the timestamps (`t mod 1s`) is plotted over the running time of the experiment (Fig. 8.17), five slanted bars can be seen running across the elapsed time. They have a spacing of 200 ms and a slope of ~ 0.45 s/day which is a lot flatter than the timeshift of the internal clocks, as can be seen in Fig. 8.4b. Additional structures can be observed inbetween these bars, possibly stemming from the 33 ms structures from the time differences. Therefore, the timestamps of the PET do not seem reliable on an absolute scale, and it appears comprehensible that coincidences with the germanium detector could not be found.

With such an unpredictable and not-well-understood system with timing effects on the 200 ms scale, it is clear that it is impossible to detect coincidences on the ~ 200 μ s level. The main problem is that the *Inveon* PET detector is a proprietary system produced by SIEMENS for research purposes, indeed, but not allowing access to the internals of the data taking. For biological or medical research and even research on the improvement of image reconstruction[42] this apparatus might be well suited, but when an accurate timing information is needed, as with this experiment, a system which allows more direct access to the DAQ system and does not shield raw data from the user would be more apt. Also since only a service contract existed with the medical department, SIEMENS was not particularly interested in helping to find out issues, that were not even impairing the system's functionality. For the future, a setup of this experiment should include a version of a PET scanner, that allows for direct access to the raw data, and where the process how timestamps are created is known and can be controlled. Moreover, a logical interface would be desirable to either receive or send out

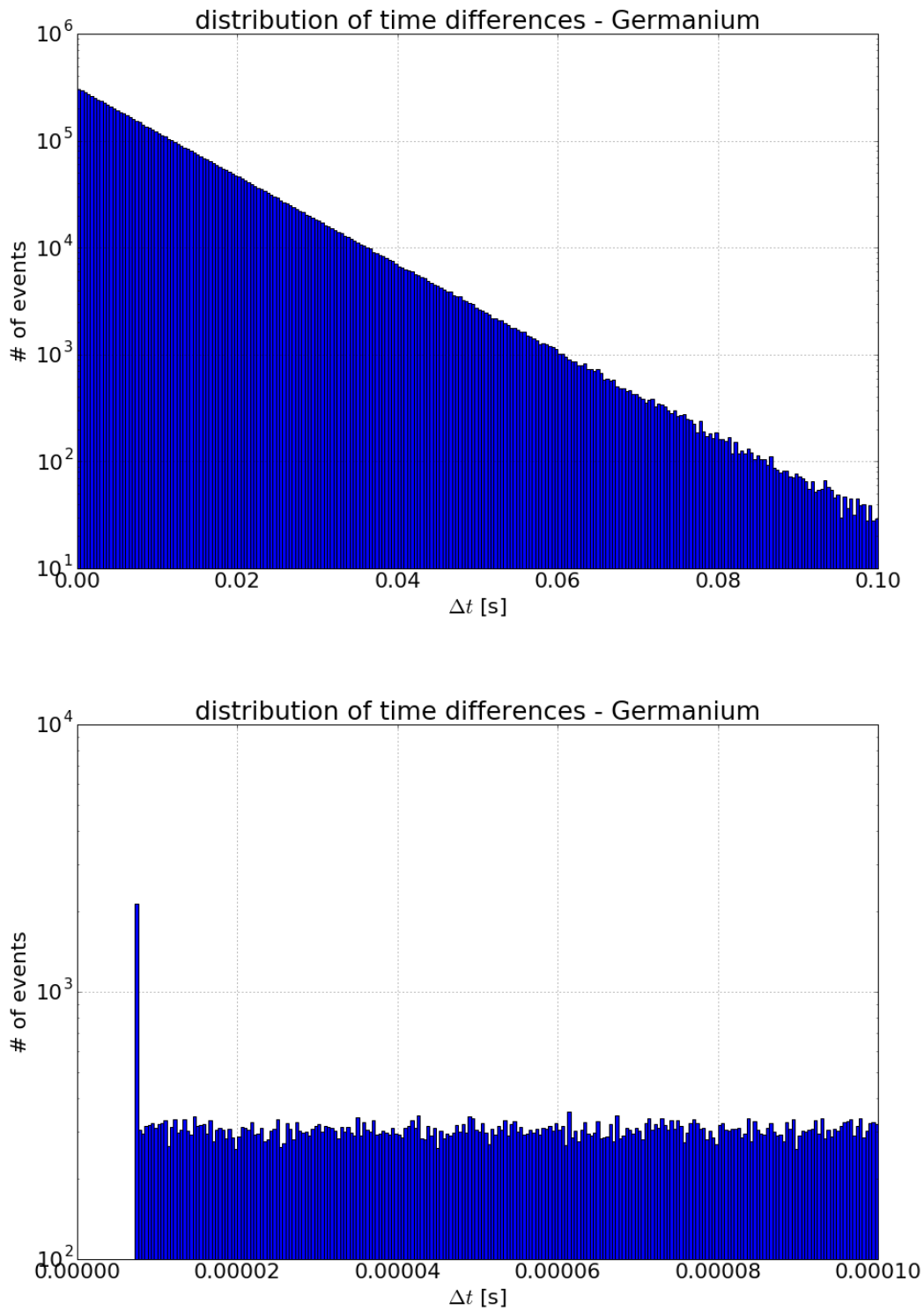


Figure 8.14: Distribution of the time differences between events in the germanium system. They follow a perfect exponential distribution. The peak for very small time differences is due to a dead time effect of the FADC. The event is recorded, but the timestamp is wrongly attributed to the readout time through the DAQ.

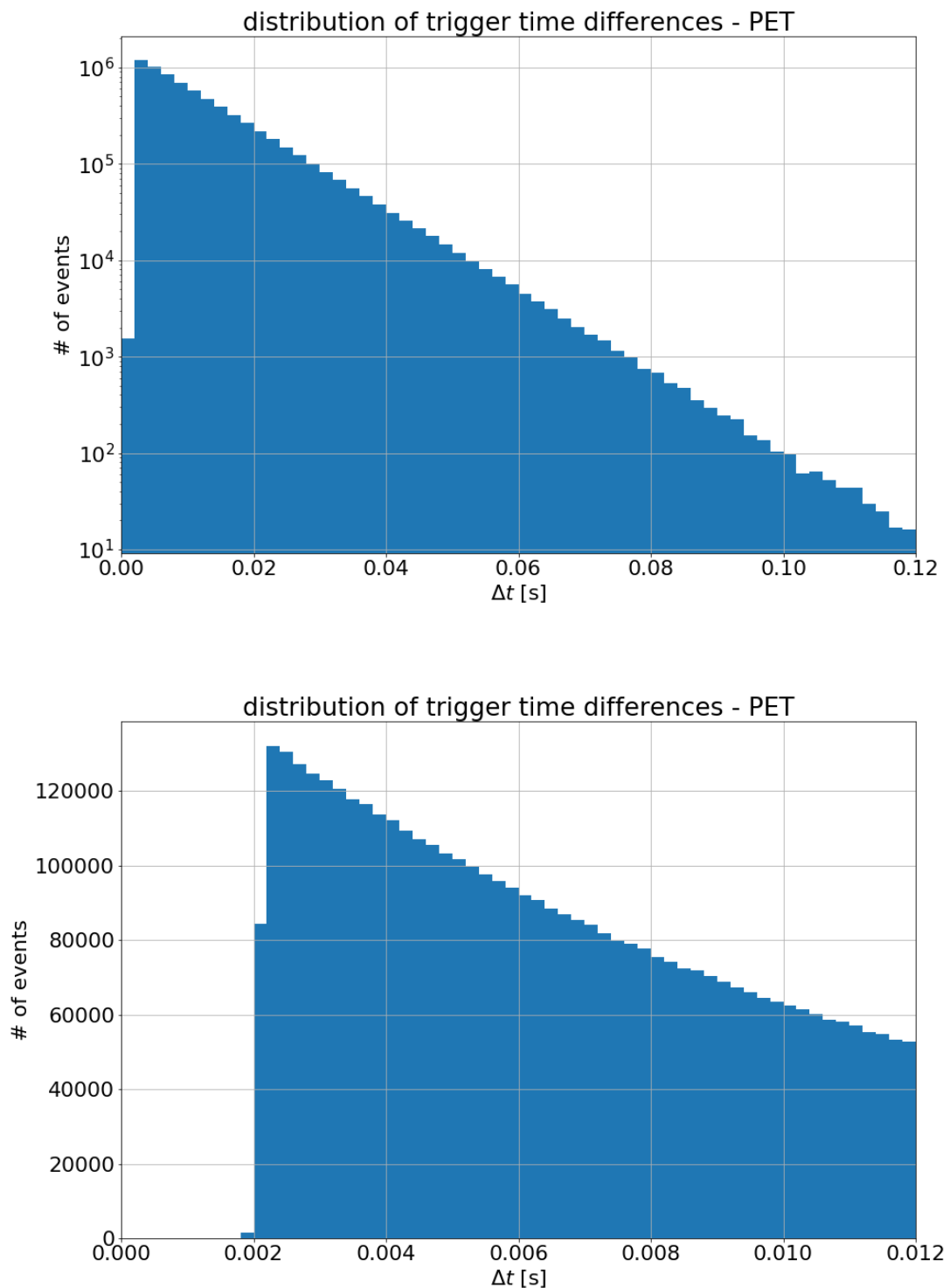


Figure 8.15: Distribution of the time differences between **trigger** events in the PET system. Binning adapted to represent $200 \mu\text{s}$ per bin in the lower part of the figure. This is basically the distribution already seen in the germanium DAQ (Fig. 8.14), only carried over to the PET DAQ via the trigger port. Distribution is exponential, below 2 ms dead time of the trigger port is reached.

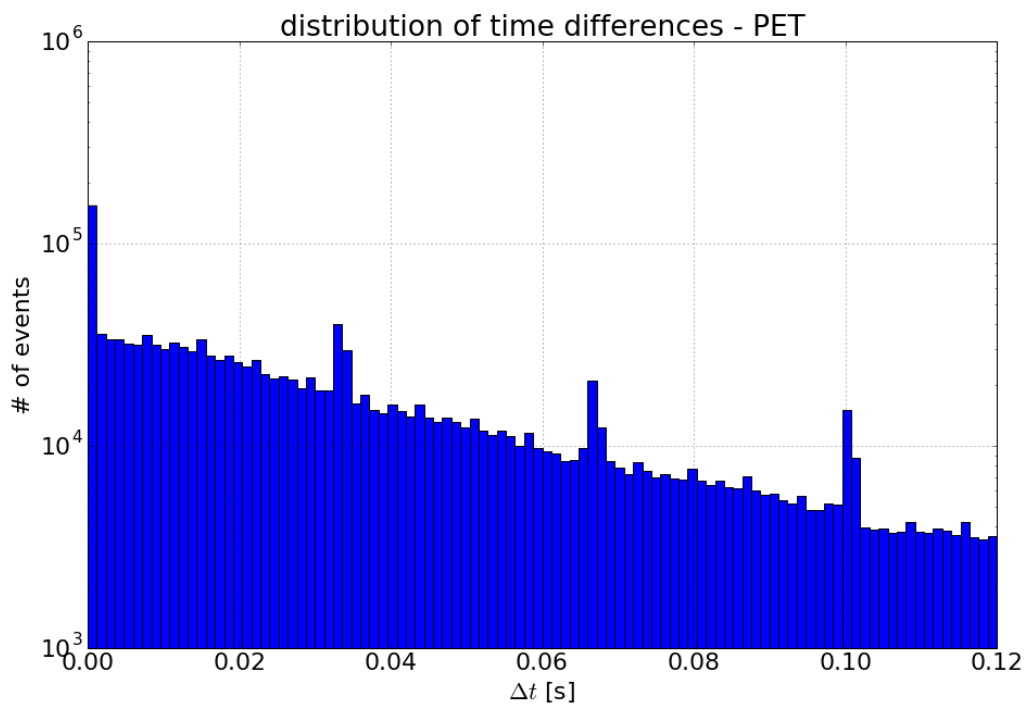


Figure 8.16: Distribution of the time differences between PET events, triggered by coincidences in the PET tube(`isTrigger==0`). Peaks at multiples of 33 ms appear. Also a wave pattern is recognisable above the flat exponential distribution. This indicates some not understood timing effects.

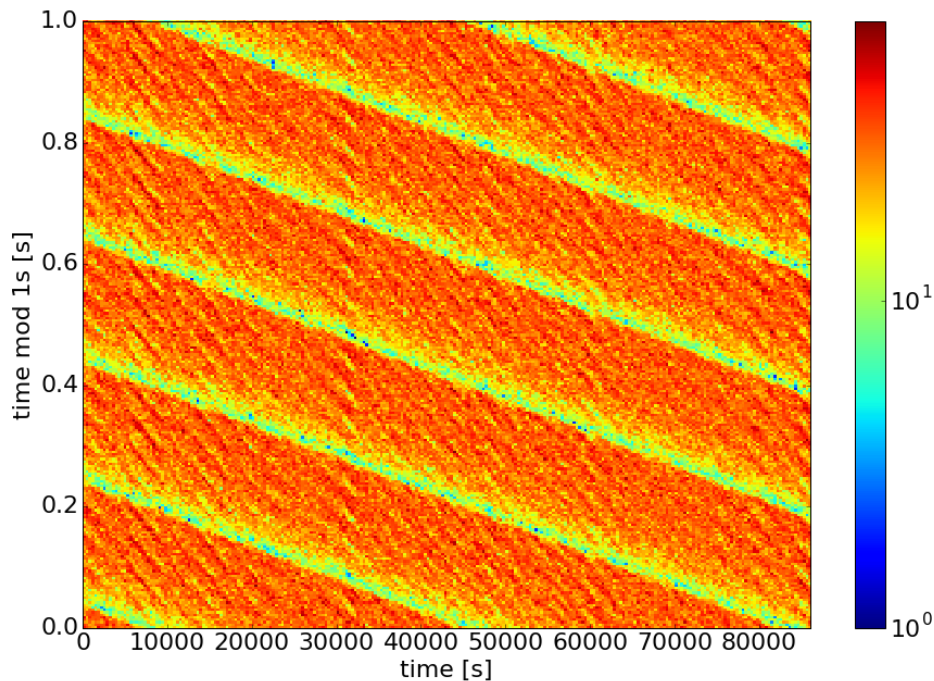


Figure 8.17: Two-dimensional histogram of time modulo 1s over time. A very strange pattern can be seen: wider bands of around 0.2s, whose absolute position changes over the measurement time, and smaller more irregular patterns in between the bands.

digital pulses in order to synchronise the two detector systems. If a timing system could be used which allowed a timing resolution better than the $200\ \mu\text{s}$ of the Inveon the coincidence window would be lowered which could minimize accidental background events. And finally, if the location of that PET system were not inside a germ-controlled environment and not in heavy production use, access to the machine and time scheduling would be a lot easier or not even necessary. This would greatly reduce the development cycle.

9

Summary

*Grad school is the snooze button on the
clock-radio of life.*

— John Rogers, comedian

This work has described a novel idea to determine the location of an interaction within a germanium detector by using a PET detector. The motivation for developing this idea was explained, which was to better understand detector behaviour in order to reduce background for the GERDA collaboration's search for the neutrinoless double beta decay. The goal of this thesis is being able to determine the point of interaction of a pair production process, which makes it possible to create a library of typical pulse shapes of single site events depending on their location in the germanium detector. It was briefly explained how germanium detectors work and especially the principles of pulse formation were briefly explained. The idea to use a PET scanner in conjunction with a germanium detector and to shine a high energy gamma source through a lead collimator to be able to infer the interaction location was introduced. Simulations and calculations to estimate the feasibility of the project were presented. The thickness and dimensionality of the lead collimator needed for the experiment were simulated. It was decided to use a $20\text{ cm} \times 5\text{ cm} \times 5\text{ cm}$ lead cuboid with a circular collimation hole with a diameter of 15 mm. With a $5\text{ MBq } ^{56}\text{Co}$ source, which is the preferred isotope, and the given dimensions of collimator, germanium, and PET detector a PET-detectable rate of $0.72\frac{1}{5}$ coincidences between PET and germanium detector is expected. The exact properties and efficiencies of the PET are unknown, but including efficiencies for absorption, the energy window efficiency, and the distribution along the z-axis of the germanium detector, in a 24 h measurement the lowest segment of the germanium detector should still experience between

1599 - 10455 events, depending on the actual efficiency. These rates and event numbers coming from the *Geant4* simulation prove the general feasibility of the experiment.


The measurement setup was further described and the analysis including two distinct methods, the *fitting method* and the *time difference method* were introduced.

While the simulations showed that there are no objections against general practicality, the real world proved to be a slightly more relentless. The PET system being a machine used in clinical trials did not provide the interfaces needed for an easy setup of a scientific experiment. While many obstacles could be overcome by using an external trigger port for the input of the germanium detector triggers and inducing a time synchronisation pattern in both systems, in the end it turned out that the internal clock of the PET is not reliable to the extent needed for the experiment. When investigating the time structure of random events certain time differences were found to occur more frequent than expected instead of the statistically anticipated exponential or flat distributions.

The success of the experiment is dependent on the simultaneous detection of events in the PET and germanium systems. Unfortunately, this could not be achieved with this experiment. Nevertheless, a new method that allows to assign typical pulse shapes to certain sectors of a germanium detector has been presented and its general feasibility has been shown through simulations. For the future, it would be desirable to work with a system that does not encapsulate all of its internal technicalities, rendering them unavailable from the user. Understanding, control, and access to the internal timing system and an input/output of digital triggers are indispensable requirements for a future experiment that wants to overcome the problem of synchronising the two systems. With the ability to produce coincidences between germanium and PET detectors, the way is clear for reconstructing the location of the interaction and using the measured pulse shapes for a pulse shape library. This library could then be used to check and improve background-reducing cuts to $0\nu\beta\beta$ data.

A

Measurement report ^{56}Co source

	Strahlenschutz-Umgebungsüberwachung am Forschungsstandort Rossendorf Ergebnisprotokoll der Aktivitätsanalyse			Auftragsnummer KSS 219/15			
Auftraggeber:	Herr Preusche, FWPH						
Probenmaterial:	Target						
Probenzahl:	2						
Ort der Probenahme:	Gebäude 707						
Probenahme:	27.10.2015						
Probenübergabe:	28.10.2015						
Bemerkungen:							
Art der Analyse / Analysedatum	Probe / Bezugsdatum, -zeit	Nuklid	Messwert	Einheit	Messun- sicherheit [%]		
ISITU- Spektrometrie 30.10.2015	Probe 5 27.10.2015; 09:19 Uhr	Co-56	4,6E+06	Bq/Probe	17		
		Co-57	3,5E+04	Bq/Probe	10		
		Co-58	3,1E+04	Bq/Probe	17		
		Mn-52	7,5E+03	Bq/Probe	38		
	Probe 6 27.10.2015; 10:29 Uhr	Co-56	3,1E+06	Bq/Probe	17		
		Co-57	2,4E+04	Bq/Probe	10		
		Co-58	2,4E+04	Bq/Probe	18		
		Mn-52	6,0E+03	Bq/Probe	34		
		Kommentar: - Bezugsdatum für die Aktivitätsangaben ist das Analysedatum, sofern nicht anders angegeben - Nuklide in Klammern gesetzt stellen Bezugsnuklide dar - Messwerte mit dem Zeichen „<“ bedeuten Erkennungsgrenzen, d.h. kein Nachweis - außer den hier angeführten Analysen wurden keine weiteren getätigt					
		Datum:	02.11.2015				
Unterschrift:	gez. Bauer KSS/U						

List of Figures

2.1	The Standard Model of particle physics	5
2.2	Probability for an initial electron neutrino to be detected as a different flavour	8
2.3	Mass hierarchy for the normal and inverted hierarchy	10
2.4	Difference in production rates of electron neutrinos induced by muon neutrinos for normal and inverted hierarchy	11
2.5	Effective neutrino mass as a function of the lightest neutrino mass	12
2.6	Parabola of isobares showing allowed and forbidden single and double beta decays	13
2.7	Feynman graphs of the two types of neutrinoless double beta decay	14
3.1	Mass attenuation coefficient for germanium	18
3.2	Schematic energy spectrum for Compton scattering. Full energy peak, DEP, and SEP are depicted	20
3.3	Sketch of the valence and conduction bands in semiconductors. Additional levels are added by doping the crystal with donor or acceptor atoms	21
3.4	pn-junction with reverse bias voltage	23
3.5	Weighting potential for semi-coaxial and BEGe germanium detectors.	25
3.6	Different locations of interaction points in the detector lead to different trajectories of the charge cloud	26
3.7	Pulses originating from different physical processes produce different waveforms	27
3.8	The parameter A/E over the energy for a Th-228 measurement	27
4.1	The structure of the GERDA experiment at Gran Sasso Laboratory	32
4.2	The Laboratori Nazionali del Gran Sasso (LNGS) under the Gran Sasso massif.	33
4.3	Sketch of two types of germanium detectors: Semi-coaxial and BEGe	34
4.4	First results of the GERDA experiment	37
4.5	Expected background and fit to data from GERDA	38
5.1	Two pulses representing typical signals for the calibration mode and for the veto mode.	42
5.2	The principle of convolution	43
5.3	Deconvoluted pulse and thresholds above (and below) which the photo electrons are counted.	44

5.4	The Fourier transforms and original signals of a template pulse and the actual signal	45
5.5	Two measured pulses together with the template pulse (in red) and the deconvolved pulses after the transformation	46
5.6	Comparing pulse height/integral method with the deconvolved template pulse method	47
6.1	Schematic view of the setup of the germanium detector inside PET tube	51
6.2	View of the <i>Geant4</i> simulation setup	52
6.3	Survival functions for DEP events in dependence of the radius for different simulation parameters. Statistical error bars are included for all curves, yet only visible for the lines with the poorest statistics. A steeply falling curve is desired as this limits the illuminated region, while still reasonable numbers of gammas should be let through.	53
6.4	Distribution of hits in the detector for a collimator with length $l=15$ cm and diameter $d=15$ mm	54
6.5	The distribution of events along the collimation axis measured in centimeters from the surface.	58
6.6	Sketch to demonstrate names and positions of lines and points in reconstruction procedure.	60
6.7	Simulated points of interaction in germanium (red) that create two gamma rays which are detected in the PET ring	61
6.8	Distance between reconstructed and simulated interaction points	62
6.9	Reconstructed positions of the ^{22}Na source in the PET detector	63
7.1	Schematic setup of the DAQ and trigger logic. The three different event types are displayed. A PET event is only registered in the PET DAQ (a), a germanium event is recorded in the Ge-DAQ, additionally a logical signal is sent to the PET (b). The pulser sends a synchronisation sequence every second to the germanium system (c), which in turn sends a coincidence marker to the PET, therefore the pulser is registered in both DAQ systems and can be used to synchronise the times.	66
7.2	Picture of the lab setup.	67
7.3	A sketch of the setup of the experiment. The arrangement of the germanium detector in the small animal PET, the lead collimator, and the radioactive source.	68
7.4	The pulser pattern, that is induced in the PET and the germanium DAQ	70
7.5	Schematic drawing of the Inveon PET scanner	71
7.6	PET and MRI images of a mouse's head. ^{11}C was used as a tracer. [21]	72
8.1	Analysis flow for the two detector systems	77

8.2	Energy spectrum measured by the germanium detector	79
8.3	A waveform recorded by the germanium detector. One sample corresponds to 10ns. The amplitude is measured in ADC units.	80
8.4	The time shift of the trigger pattern can be seen in the shift of the decimal places of the triggers for the germanium (8.4a) and the PET system individually (8.4b)	81
8.5	A fit to the timing distribution of the events goes wrong when events from the germanium detector are not cleaned up	84
8.6	The remainder of the floating point division of 1s is shifted up by one second for timestamps smaller than 70300.624 s. This creates a continuous slope in the line of pulser events.	85
8.7	Decimal places of timestamps of pulser	87
8.8	Corrected decimal places for germanium events	88
8.9	The actual time shift is found at the value of the time shift with the highest number of coincidences	89
8.10	Distribution of time differences between events, including triggers, PET and germanium events. Most events are contained within $\pm 300 \mu\text{s}$	90
8.11	Histograms obtained when applying the $ \Delta t < 200 \mu\text{s}$ coincidence cut between PET and germanium events	91
8.12	Time difference between a trigger event followed by a coincidence event . . .	92
8.13	Distribution of Δt between trigger and PET events as recorded by the PET .	94
8.14	Distribution of the time differences between events in the germanium system. They follow a perfect exponential distribution. The peak for very small time differences is due to a dead time effect of the FADC. The event is recorded, but the timestamp is wrongly attributed to the readout time through the DAQ.	96
8.15	Distribution of the time differences between trigger events in the PET system	97
8.16	Distribution of the time differences between PET events, triggered by coincidences in the PET tube(<code>isTrigger==0</code>). Peaks at multiples of 33 ms appear. Also a wave pattern is recognisable above the flat exponential distribution. This indicates some not understood timing effects.	98
8.17	Two-dimensional histogram of time modulo 1s over time	99

List of Tables

2.1	The three forces of the Standard Model and their exchange particles.	5
2.2	Neutrino mixing angles	9
2.3	Property of the neutrino/anti-neutrino if they behave like a Majorana/Dirac particle	14
2.4	Overview of the different $0\nu\beta\beta$ isotopes and experiments searching for it . . .	15
5.1	Correlation coefficient for different threshold values for the two light realms and their corresponding methods compared to the deconvolution method . . .	48
6.1	Results for different simulation parameters. The survival function gives the percentage of hits not contained within the given radius.	53
6.2	Best parameters for the dimensioning of the collimator as found by simulation.	55
6.3	Detected events with different criteria from simulation	56
6.4	Overview of the expected number of events from simulation in a 24 h measurement with a 5 MBq source	57
7.1	Results for input port checks.	69

Bibliography

- [1] J. N. Abdurashitov et al. Measurement of the Solar Neutrino Capture Rate by SAGE and Implications for Neutrino Oscillations in Vacuum. *Phys. Rev. Lett.*, **83**:4686–4689, Dec 1999.
- [2] K. Abe et al. Indication of Electron Neutrino Appearance from an Accelerator-Produced Off-Axis Muon Neutrino Beam. *Phys. Rev. Lett.*, **107**:041801, Jul 2011.
- [3] K. Abe et al. Letter of Intent: The Hyper-Kamiokande Experiment — Detector Design and Physics Potential —. *ArXiv e-prints*, **1109.3262**, September 2011.
- [4] Y. Abe et al. Indication of Reactor $\bar{\nu}_e$ Disappearance in the Double Chooz Experiment. *Phys. Rev. Lett.*, **108**:131801, Mar 2012.
- [5] I. Abt et al. A New ^{76}Ge Double Beta Decay Experiment at LNGS. *ArXiv e-prints*, **hep-ex/0404039**, 2004.
- [6] K.-H. Ackermann et al. The Gerda experiment for the search of $0\nu\beta\beta$ decay in ^{76}Ge . *Eur. Phys. J. C*, **73**(3):1–29, 2013.
- [7] P. Adamson et al. Improved Search for Muon-Neutrino to Electron-Neutrino Oscillations in MINOS. *Phys. Rev. Lett.*, **107**:181802, Oct 2011.
- [8] S. Agostinelli et al. Geant4—a simulation toolkit. *Nucl. Instr. Methods A*, **506**(3):250–303, 2003.
- [9] M. Agostini et al. Pulse shape discrimination for Gerda Phase I data. *Eur. Phys. J. C*, **73**(10):1–17, 2013.
- [10] M. Agostini et al. Results on Neutrinoless Double- β Decay of ^{76}Ge from Phase I of the GERDA Experiment. *Phys. Rev. Lett.*, **111**:122503, Sep 2013.
- [11] M. Agostini et al. The background in the $0\nu\beta\beta$ experiment Gerda. *Eur. Phys. J. C*, **74**(4):2764, 2014.
- [12] M. Agostini et al. Improvement of the energy resolution via an optimized digital signal processing in GERDA Phase I. *The European Physical Journal C*, **75**(6):1–11, 2015.

- [13] J. K. Ahn et al. Observation of Reactor Electron Antineutrinos Disappearance in the RENO Experiment. *Phys. Rev. Lett.*, **108**:191802, May 2012.
- [14] C. H. Albright. Normal vs. inverted hierarchy in type I seesaw models. *Physics Letters B*, **599**(3-4):285 – 293, 2004.
- [15] M. Ambrosio et al. Search for the sidereal and solar diurnal modulations in the total MACRO muon data set. *Physical Review D*, **67**:042002, Feb 2003.
- [16] F. P. An et al. Observation of Electron-Antineutrino Disappearance at Daya Bay. *Phys. Rev. Lett.*, **108**:171803, Apr 2012.
- [17] A. S. Barabash. Average and recommended half-life values for two neutrino double beta decay: Upgrade-2013. *AIP Conference Proceedings*, **1572**(1):11–15, 2013.
- [18] M. Bauer et al. MaGe: a Monte Carlo framework for the Gerda and Majorana double beta decay experiments. *J. Phys.: Conf. Ser.*, **39**(1):362, 2006.
- [19] G. Bellini et al. Final results of Borexino Phase-I on low-energy solar neutrino spectroscopy. *Phys. Rev. D*, **89**:112007, Jun 2014.
- [20] M. Berger et al. XCOM: Photon cross sections database. 2010. National Institute of Standards and Technology, Gaithersburg, MD.
URL <http://www.nist.gov/pml/data/xcom>
- [21] W. S. I. Center. Preclinical Imaging & Radiopharmacy. image brochure.
- [22] G. Collaboration et al. Background-free search for neutrinoless double- β decay of ^{76}Ge with GERDA. *Nature*, **544**(7648):47–52, 2017.
- [23] C. L. Cowan, F. Reines, F. B. Harrison, H. W. Kruse and A. D. McGuire. Detection of the Free Neutrino: a Confirmation. *Science*, **124**(3212):103–104, 1956.
- [24] R. Davis, D. S. Harmer and K. C. Hoffman. Search for Neutrinos from the Sun. *Phys. Rev. Lett.*, **20**:1205–1209, May 1968.
- [25] A. de Gouvea. "On Determining the Neutrino Mass Hierarchy". Theory seminar at FNAL, 2006.
- [26] DONUT Collaboration et al. Observation of tau neutrino interactions. *Physics Letters B*, **504**:218–224, April 2001.
- [27] F. Feruglio, A. Strumia and F. Vissani. Addendum to:"Neutrino oscillations and signals in β and $0\nu 2\beta$ experiments"[Nucl. Phys. B 637 (2002) 345]: First KamLAND results. *Nuclear Physics B*, **659**(1):359–362, 2003.
- [28] K. L. Freund. *Muonic background in the GERDA neutrinoless double-beta experiment*. Ph.D. thesis, Universität Tübingen, 2014.

- [29] Y. Fukuda et al. Evidence for Oscillation of Atmospheric Neutrinos. *Phys. Rev. Lett.*, **81**:1562–1567, Aug 1998.
- [30] C. Giunti and M. Laveder. Neutrino Mixing. *ArXiv High Energy Physics - Phenomenology e-prints*, **hep-ph/0310238**, October 2003.
- [31] M. Goeppert-Mayer. M. Goeppert-Mayer, *Phys. Rev.* 48, 512 (1935). *Phys. Rev.*, **48**:512, 1935.
- [32] D. Greiner. *Design und Aufbau des Double Chooz Myon-Vetos*. Ph.D. thesis, Universität Tübingen, 2013.
- [33] W. Hampel et al. GALLEX solar neutrino observations: results for GALLEX IV. *Phys. Lett. B*, **447**(1-2):127–133, 1999.
- [34] J. Hartnell. Neutrinoless Double Beta Decay with SNO+. *J. Phys.: Conf. Ser.*, **375**(4):042015, 2012.
- [35] K. Heyde. *Basic Ideas and Concepts in Nuclear Physics: An Introductory Approach, Second Edition*. Taylor & Francis, 1998.
- [36] K. S. Hirata et al. Results from one thousand days of real-time, directional solar-neutrino data. *Phys. Rev. Lett.*, **65**:1297–1300, Sep 1990.
- [37] C. C. Hu. *Modern semiconductor devices for integrated circuits*. Pearson, 2010.
- [38] KATRIN collaboration. KATRIN: A next generation tritium beta decay experiment with sub-eV sensitivity for the electron neutrino mass. *ArXiv High Energy Physics - Experiment e-prints*, **hep-ex/0109033**, September 2001.
- [39] H. Klapdor-Kleingrothaus, I. Krivosheina, A. Dietz and O. Chkvorets. Search for neutrinoless double beta decay with enriched ^{76}Ge in Gran Sasso 1990-2003. *Phys. Rev. B*, **586**(3-4):198 – 212, 2004.
- [40] M. A. Knapp. *Design, Simulation und Aufbau des GERDA-Myonvetos*. Ph.D. thesis, Universität Tübingen, 2009.
- [41] T. K. Lewellen. Recent developments in PET detector technology. *Physics in medicine and biology*, **53**(17):R287, 2008.
- [42] C.-C. Liu. *Development of a dedicated image reconstruction and performance evaluation of a small animal MR-compatible PET-insert*. Ph.D. thesis, Universität Tübingen, 2016.
- [43] E. Majorana. Teoria simmetrica dell’ elettrone e del positrone. *Il Nuovo Cimento*, **14**:171–184, April 1937.
- [44] D. Marble. Gamma spectra.
URL <http://faculty.tarleton.edu/marble/AdvLab/Emass/GammaSpectra.htm>

- [45] W. McKinney. Data Structures for Statistical Computing in Python. In S. van der Walt and J. Millman, editors, *Proceedings of the 9th Python in Science Conference*, pages 51 – 56. 2010.
- [46] J. Nagel. *Ortsrekonstruktion von Single Site Events in einem Germaniumdetektor mit Hilfe eines Positionen-Emissions-Tomographen*. Bachelorarbeit, Universität Tübingen, 2015.
- [47] K. A. Olive et al. Review of Particle Physics. *Chin. Phys.*, **C38**:090001, 2014.
- [48] W. Pauli. Offener Brief an die Gruppe der Radioaktiven bei der Gauvereinstagung zu Tübingen, 1930.
URL http://cds.cern.ch/record/83282/files/meitner_0393.pdf
- [49] Planck Collaboration et al. Planck 2015 results. XIII. Cosmological parameters. *ArXiv e-prints*, **1502.01589**, February 2015.
- [50] B. Pontecorvo. Inverse beta processes and nonconservation of lepton charge. *J. Exptl. Theoret. Phys.*, **34**:247–249, 1958.
- [51] F. Ritter. *Analysis of the GERDA muon veto - first light*. Ph.D. thesis, Universität Tübingen, 2012.
- [52] G. B. Saha. Basics of PET imaging: Physics. *Chemistry, and Regulations*, Springer, 2010.
- [53] M. Salathe. *Study on modified point contact germanium detectors for low background applications*. Ph.D. thesis, Ruperto-Carola-University of Heidelberg, 2015.
- [54] Siemens Medical Solutions USA, Inc. *Inveon - No Limits on Discovery*. 810 Innovation Drive Knoxville, TN 37932-2751, 2008. Technical brochure.
- [55] S. Vandenberghe, E. Mikhaylova, E. D’Hoe, P. Mollet and J. S. Karp. Recent developments in time-of-flight PET. *EJNMMI Physics*, **3**(1):3, 2016.
- [56] Wikipedia. Neutrino oscillation — Wikipedia, The Free Encyclopedia, 2017. [Online; accessed 8-August-2017].
URL https://en.wikipedia.org/wiki/Neutrino_oscillation
- [57] Wikipedia. Standard Model — Wikipedia, The Free Encyclopedia, 2017. [Online; accessed 17-March-2017].
URL https://en.wikipedia.org/wiki/Standard_Model

Acknowledgements/Danksagung

Nun bleibt mir am Ende dieser Arbeit, die sich doch länger hinzog als ursprünglich geacht nichts weiter zu tun, als mich bei denjenigen zu bedanken, die zur Entstehung derselbigen beigetragen haben.

Das sind zuvorderst meinen beiden betreuenden Professoren Peter Grabmayr und Josef Jochum, die für den fachlichen, finanziellen und organisatorischen Rahmen gesorgt haben. Die GERDA Kollaboration, von der ich ein Teil werden und wissenschaftliche Luft schnuppern durfte. Die Arbeitseinsätze und Kollaborationstreffen in halb Europa waren arbeitsreich, aber immer hoch interessant und von einer sehr freundlichen, menschlichen Atmosphäre geprägt. Und lernen konnte man von jedem Einzelnen der Kollaborationsmitglieder etwas.

Aber ich will mich vor allem auch bei meinen Kollegen in der Arbeitsgruppe bedanken, die jede Kaffee- und Mittagspause mit sachlichen und unsachlichen Diskussionen gefüllt haben; und wenn die Pausen nicht ausgereicht haben, die Diskussion in den Boulanger verlegt haben. Den Kollegen, die sich im Laufe der Promotion auch zu Freunden entwickelt haben, gilt ein besonders großes Dankeschön.

Herrn Preusche vom Forschungszentrum Rossendorf bin ich zu großem Dank verpflichtet, da er die im Experiment verwendete ^{56}Co -Quelle unkompliziert hergestellt und verschickt hat. Chih-Chieh "James" Liu war der Ansprechpartner für den Betrieb des PETs. Viele, viele Stunden an sams- und sonntäglichen Morgen- und Abendstunden hat er dafür geopfert. Fachlich wie menschlich war die Zusammenarbeit mit ihm hervorragend. Ihm ist nur zu wünschen, dass er sich in der kalifornischer Sonne seine akademischen Lorbeeren verdienen kann. Alex Hegai sei gedankt fürs Bereitstellen von experimentellem Germaniumwissen und logistischer Hilfe beim Durchführen des Experiments.

Ganz besonderer Dank gilt aber den Leuten, die nie müde wurden mir hinterher zu sein und durch ständiges Nachfragen womöglich signifikant zum Abschluss dieser Arbeit beigetragen haben und trotzdem ein offenes Ohr hatten für die Unwägbarkeiten der Promotion. Das waren vor allem meine Freundin Michaela Mann und meine Eltern.